Implementation and Performance Analysis of 3D Cone and Frustum Filters

by

Hussam Shubayli
B.Sc., Jubail Industrial College, Saudi Arabia, 2011

A Thesis Submitted in Partial Fulfillment of the
Requirements for the Degree of

MASTER OF APPLIED SCIENCE

in the Department of Electrical and Computer Engineering

Implementation and Performance Analysis of 3D Cone and Frustum Filters

by

Hussam Shubayli
B.Sc., Jubail Industrial College, Saudi Arabia, 2011

Supervisory Committee

Dr. Panajotis Agathoklis, Co-Supervisor
(Department of Electrical and Computer Engineering)

Dr. Hari Reddy, Co-Supervisor
(Department of Electrical and Computer Engineering)

Supervisory Committee

Dr. Panajotis Agathoklis, Co-Supervisor
(Department of Electrical and Computer Engineering)

Dr. Hari Reddy, Co-Supervisor
(Department of Electrical and Computer Engineering)

ABSTRACT

In this thesis, new effective and efficient implementation structures of three-dimensional (3D) spatio-temporal (ST) Finite Impulse Response (FIR) uniform and non-uniform cone and frustum filters using well-known filter banks are investigated. The performance of the proposed implementation structures for 3D ST FIR uniform and non-uniform cone and frustum filters are investigated for 3D broadband beamforming in radio astronomy applications.

First, implementations of two 3D ST uniform FIR cone filters are investigated. The 3D cone filters are designed by cascading either the well-known uniform quadrature mirror cosine-modulated (QM-CM) filter bank or directly designed filter banks (DDFBs), with 2D low-pass circularly-symmetric spatial filters. In addition, two 3D ST uniform FIR frustum filters are derived from the cone filters by implementing partial bands of the filter banks with corresponding 2D spatial filters. The performance of the proposed implementation structures for 3D ST uniform QM-CM and DDFBs cone and frustum filters are evaluated using broadband beamforming signals in radio astronomy applications. The performance of the QM-CM and DDFBs cone and frustum filters shows improvement in terms of Signal-to-Interference-plus-Noise ratio (SINRs) over existing 3D ST cone and frustum filters. In addition to their effective performance, these cone and frustum filters can be efficiently implemented with equivalent or less computational complexity compared to existing methods.

Second, implementations of two 3D ST non-uniform cone and frustum filters are explored. These cone and frustum filters are obtained by cascading either QM-CM or DDFBs non-uniform filter banks, with 2D low-pass circularly-symmetric spatial filters. The motivation for the 3D ST *non-uniform* cone and frustum filters is to achieve better approximation at low temporal frequencies than using the *uniform* ones. The performance of the 3D ST *non-uniform* cone and frustum filters is evaluated and compared with the performance of the *uniform* 3D ST cone and frustum filters. Results indicate that the performance of the proposed 3D ST *non-uniform* QM-CM and DDFBs cone filters shows some improvement in selective filtering compared to the performance of 3D ST *uniform* cone filters.

Contents

List of Tables

List of Figures

ACKNOWLEDGEMENTS

I would like to express my deep gratitude to Dr. Pan Agathoklis, my co-supervisor, for his kind supervision, patient guidance, enthusiastic encouragement and useful critiques of this research work. I would also like to thank Dr. Hari Reddy, my co-supervisor, for his advice, help, useful suggestions and recommendations in this research work.

My grateful thanks are also extended to academic stuffs in Department of Electrical and Computer Engineering at University of Victoria for their outstanding teaching.

Next, I would like to thank the Department of Electrical and Computer Engineering stuffs for their support, assistance and help in offering me the resources.

I would like to thank all my friends for the moment, minutes and hours they spent to assist and encourage me. I would like to thank my friend and officemate Chamira Edussooriya for his help and encouragement during my research work.

I would also like to extend my thanks to my mother, sisters, brothers, other family members for their encouragement and support throughout my study.

Last but not least, I would to thank the Ministry of Education in Saudi Arabia and the Saudi Cultural Bureau in Canada for their support and assistance during my study and research.

DEDICATION

To the loving memory of my father.
To my mother for her patience and support.
To my brothers and sisters for their advice and encouragement.
To my friends for their time, advice, and inspiration.

List of Abbreviations

1D	One-Dimensional
2D	Two-Dimensional
3D	Three-Dimensional
4D	Four-Dimensional
5D	Five-Dimensional
BB	Broadband
CD	Continuous-Domain
CDFT	Continuous-Domain Fourier Transform
DAAs	Dense Aperture Arrays
DDFT	Discrete-Domain Fourier Transform
DDFBs	Directly Designed Filter Banks
DFT	Discrete Fourier transfer
FB	Filter Bank
FIR	Finite Impulse Response
FoV	Field of View
FPAs	Focal Plane Arrays
IIR	Infinite Impulse Response
MD	Multidimensional
MDFT	Modified Discrete Fourier Transform
NPR	Near Perfect Reconstruction
NU	Non-uniform
NUFBs	Non-uniform Filter Banks
QM-CM	Quadrature Mirror Cosine Modulated
RFI	Radio Frequency Interference
ROS	Region of Support
PR	Perfect Reconstruction
PW	Plane Waves
SKA	Square Kilemetre Arrays
SINR	Signal-to-Interference-plus-Noise Ratio
SOI	Signal of Interest
ST	Spatio-Temporal
UFBs	Uniform Filter Banks

Chapter 1

Introduction

Multidimensional (MD) signal processing techniques have been implemented in various fields such as video signal processing, light field processing, wireless communication, radar signal processing, seismic signal processing, cognitive radio, and image processing [1][2][3][4][5][6][7][8][9]. Five-dimensional (5D) depth-velocity filtering techniques, for instance, are employed in light field video applications for enhancing moving objects with a constant velocity and specific depth [1]. Moreover, four-dimensional (4D) depth filtering techniques are used for enhancing or attenuating video objects based on their depth [2][3]. The three-dimensional (3D) spatio-temporal (ST) filtering techniques have been utilized in video signal processing, wireless communications, and other applications [4]-[9]. In these fields, for instance, two spatial dimensions and one temporal dimension may represent a 3D signal. In video applications, for example, 3D ST dimensions can represent an object with a constant 2D spatial velocity moving on a linear trajectory motion over time [10][11]. In wireless communication, 3D ST signal representation can be used to express a 2D array that received a broadband (BB) signal over time [11]. 3D ST filtering techniques have been successfully implemented in these applications for their capability to enhance 3D ST plane waves based on direction of arrival, and attenuate undesirable signal based on direction of arrival[12][13][14][15].

In addition to 3D ST filtering applications in various fields such as video signal processing and wireless communications [4]-[9], 3D ST filtering techniques that employ 3D cone and frustum filters have a potential implementation in emerging radio telescopes; more specifically, in the Square Kilometre Array (SKA) to resolve some unprecedented challenges [16][17][18][19][20][21]. The SKA is an aperture synthesis radio telescope with high sensitivity, survey speed, and large field of view that will be constructed to study most significant phenomena of the universe that have never been studied [16][20]. The SKA is a massive radio telescope that will occupy an area of one kilometer-square [20] Figure 1.1. The scientific objectives of the SKA project are to study cosmology, and the evolution of stars and galaxies; to test gravity; to understand the origin and evolution of cosmic magnetism and the cradle of life; to investigate the dark ages; and to explore the unknown phenomena of the universe [20]. In the SKA, the survey speed and large field of view are two keys design specifications for the observation of frequency below 1.5 GHz. Therefore, the emerging dense aperture arrays (DAAs) and focal plane arrays (FPAs) that are mounted on paraboloidal refactors are considered to achieve largest field of view [20][22][23]. The design and construction of the SKA is encountering several technical and economic challenges; therefore, many research teams have been investigating several technical aspects, and developing reasonable technical solutions [22][23][24][25].

From the perspective of enhancing signal processing, 3D ST cone and frustum filters have been proposed to be employed with emerging DAAs and FPAs to achieve high survey speed and sensitivity. The 3D ST cone and frustum filters are appropriate for selective filtering for the so-called SKA midband signal (0.5-1.5 GHz) BB signal, such as signals coming from pulsars, by enhancing the signal of interest (SOI) and attenuating terrestrial radio frequency interference (RFI) and other undesired signals [16]-[19],[26][27][28]. Although various narrowband techniques had been previously proposed to temporally process narrowband and broadband signals, these techniques are less effective to process BB signal. 3D ST cone and frustum filters are attractive for the SKA midband due to their inherent capability of processing BB signals directly that is without converting to narrowband signals and using narrowband signal processing techniques [29][30][31]. Furthermore, although some 3D ST techniques that are suitable to processing BB signal have been proposed [26][28], to achieve effective performance and improvement in terms of signal-to-interference-plus-noise ratio (SINR); the current research is seeking to develop 3D ST techniques with efficient computations and effective performance, such as the method proposed in [32][33], to implement in the SKA and other applications.

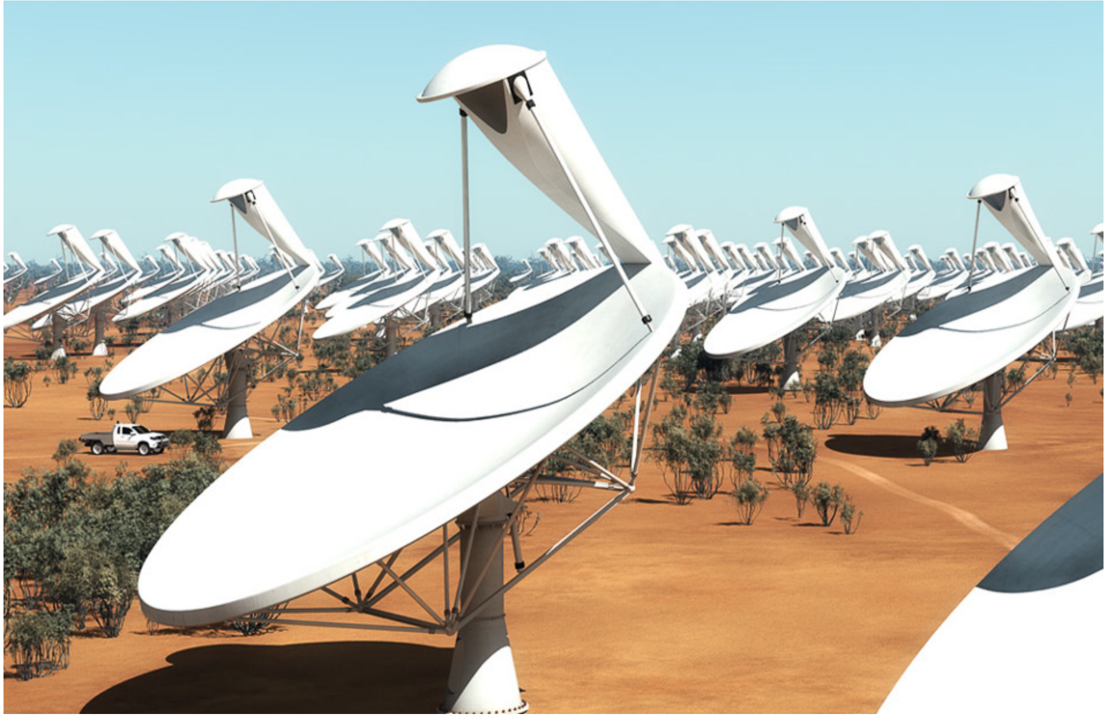

Figure 1.1: The visualisation of the SKA,(created by Swinburne 3D Productions, source: http:/petergarnick.com.au/exhibitions/atcex/)

1.1 Contributions of the Thesis

The main objectives of this thesis are to explore the design and implementation of various uniform and non-uniform 3D ST Finite Impulse Response (FIR) cone and frustum filters by utilizing well-known filter banks, and to test the performance of the designed 3D cone and frustum filters in radio astronomy applications.

In this thesis, two uniform 3D ST FIR cone filters, based on well-known filter banks, are proposed to achieve effective performance and efficient implementation. The two proposed uniform 3D ST cone filters are based on the well-known filter banks: the quadrature mirror cosine modulated (QM-CM) filter banks [34], and directly designed filter banks (DDFBs) [35]. Moreover, two uniform 3D ST FIR frustum filters are derived from the two originally proposed uniform 3D ST cone filters. The proposed 3D ST cone and frustum filters have shown some improvement in terms of SINRs over existing 3D MDFT cone filters [32][33]. Two illustrative examples for the proposed 3D ST cone and frustum filters confirm the effective performance of the proposed 3D uniform cone and frustum filters. In addition, the efficient implementation using poly-phase representations for the proposed uniform 3D ST cone and frustum filters are presented and evaluated.

The second contribution of this thesis is design and implementation of two non-uniform ST FIR cone filters based on the non-uniform QM-CM filter bank [36] and DDFBs [35]. Furthermore, we derive two non-uniform 3D ST frustum filters from the two proposed non-uniform 3D ST cone filters. The non-uniform 3D ST cone filters are proposed to investigate the non-uniform bandwidth 3D ST cone and frustum filters that have not been intensively investigated, and to evaluate their performance in some selective filtering applications where the BB SOI is nearly intervened with RFI signals at low temporal frequency. The performance of the two proposed non-uniform 3D ST cone filters, the two proposed uniform 3D ST QM-CM filter bank and DDFBs cone filters, and the existing modified discrete Fourier transform (MDFT) 3D cone filter in [32][33] are evaluated and compared to observe the performance of the non-uniform 3D ST method.

1.2 Organization of the Thesis

This thesis consists of six chapters, and three appendices following the bibliography. In Chapter 2, various uniform filter banks that are used in the design of the uniform 3D ST cone filters are reviewed. The design methods and derivation of analysis and synthesis filters of uniform MDFT [37], quadrature mirror cosine modulated [34] and directly designed [35] filter banks are presented and illustrated in Section 2.2. In Section 2.3, the entire M-band MDFT, QM-CM, and DDFBs are analyzed, and their performances are compared in terms of aliasing distortion and amplitude responses. The analysis of partial bands of MDFT, QM-CM, and DDFBs is presented with examples in Section 2.4.

In Chapter 3, a review of the non-uniform filter banks especially the QM-CM [36] and DDFBs [35] that are used to implement the non-uniform 3D ST cone and frustum filters is presented. Section 3.2 provides a general review of the development of non-uniform filter banks theories and design methods. An analysis concerning the design of non-uniform QM-CM filter banks is discussed in Section 3.3. A review of the non-uniform DDFBs is presented in Section 3.4.

In Chapter 4, the design of the two proposed uniform 3D ST FIR cone filters is presented. A review of the previously proposed 3D ST MDFT cone filter [32][33] is addressed in Section 4.2. The design of the two proposed 3D ST QM-CM and DDFBs cone filters is discussed in details in Section 4.3 and 4.4, respectively. In Section 4.5, a comparison between the two proposed uniform 3D ST cone and frustum filters and previously proposed MDFT cone and frustum [32][33] filters are presented in term of magnitude response, aliasing distortion, and amplitude distortion. In Section 4.6, the comparison is extended to evaluate the SINR values and compare the performance of the 3D QM-CM, DDFBs and MDFT [32][33] cone and frustum filters in selective filtering of BB signals received by DAAs and FPAs. Finally, a comparison of the computational complexity required by the 3D ST QM-CM, DDFBs, and MDFT cone and frustum filters to process samples is demonstrated in Section 4.7.

Chapter 5 concerns the design of the two proposed non-uniform 3D ST cone filters with an application in selective filtering of BB signals. In Section 5.2, the design details of the non-uniform 3D ST FIR QM-CM cone filter is presented, while Section 5.3, describes the second non-uniform 3D ST FIR DDFBs cone filters. A comparison of amplitude and aliasing distortion between the two proposed non-uniform 3D ST QM-CM and DDFBs cone filters is presented in Section 5.4. In Section 5.5, the performance of previously proposed uniform 3D cone filters in Chapter 4, 3D ST MDFT cone filters and the proposed non-uniform 3D ST cone filters are analyzed in selective filtering and their SINRs are evaluated and compared.

Finally, Chapter 6 summarizes the previous chapters and important conclusions and addresses the future applications of the 3D ST cone and frustum filters.

Chapter 2

A Review of Various Uniform Filter Banks

2.1 Introduction

Uniform M-band digital filter banks have various applications in such areas as subband coding, image processing, speech processing, radar signal processing, communications, adaptive filtering, and implementation of 3D cone and frustum filters [26][33][38][39][40][41][42][43][44][45][46][47]. Many classes of M-band digital filter banks have been designed such as modulated discrete Fourier transform (DFT) filter banks [38]-[47], modulated modified discrete Fourier transform (MDFT) filter banks [37][48][49][50], quadrature mirror cosine modulated (QM-CM) [38][42][34] filter banks, cosine modulated (CM) filter banks [38][40], and directly-designed filter banks (DDFBs) [35][51] in order to meet the requirements of various applications.

In literature, uniform M-band digital filter banks can be classified as modulated filter banks and directly designed filter banks. In the modulated filter bank classes, the M analysis and M synthesis filters are obtained from one or more prototype filter(s) by appropriate modulations such as cosine, DFT, etc. The M analysis and M synthesis filters of the directly designed filter banks are directly obtained. In order to meet various objectives, numerous methods and optimization techniques are used in the design of these filter banks, for instance, to achieve perfect reconstruction (PR) conditions, or to achieve near-PR conditions [38]. Perfect reconstruction systems are recognized as having an output that is a shifted version of its input; therefore, the PR filter bank is free from aliasing distortion, amplitude distortion, and phase distortion. As the name implies, the near-PR systems introduce some errors, and so only approximate the performance of the PR systems.

Throughout this chapter, the analysis concerns uniform maximally-decimated filter banks. Generally, the uniform M-band digital filter banks consist of M analysis filters, down-samplers, up-samplers, and M synthesis filters. The down-samplers' and up-samplers' factors are equal to the number of bands (M) so these systems are called maximally-decimated. The M analysis filters divide the spectrum of the input signal into M equally-spaced 'uniform' sub-bands. Down-samplers stretch the spectrum of each sub-band signal; conversely, the up-samplers contract the spectrum of the expanded sub-band signals. Finally, the M synthesis filters recombine the up-sampled signals into the reconstructed signal. In this chapter, MDFT filter banks, QM-CM filter banks, and DDFBs as proposed in the papers [37][34][35] are overviewed and studied in detail. In Section 2.2, the MDFT, QM-CM, and directly-design methods are explained. As well, the prototype filters' requirements and design methods for the MDFT and the QM-CM filter banks are reviewed; moreover, the complex DFT modulation and real cosine modulation are discussed. The method for obtaining analysis and synthesis filters for the DDFBs is illustrated. Finally, the relationships between the input and output of MDFT, QM-CM, and DDFBs are identified, and the amplitude distortion functions and aliasing distortion functions are derived. In Section 2.3, the performance of each of the entire M-band[1], MDFT, QM-CM, and DDFBs is analyzed and compared. The comparison criteria are well-established in order to make the comparison reasonable; furthermore, the performances of the entire M-band MDFT, QM-CM and DDFBs compared to the PR conditions are addressed. We study the performance of three sets of MDFT, QM-CM, and DDFBs in terms of aliasing distortion and amplitude distortion. The three sets consist of $2M$-band MDFT, M-band QM-CM, and M-band DDFBs. Finally, the section is concluded with the comparison results to show the performance of all filter banks, and to check the perfect reconstruction conditions of these filter banks.

Section 2.4 analyses and explores the performance of partial[2] MDFT, QM-CM, and DDFBs. Detailed analyses of amplitude and aliasing distortion for partial MDFT, QM-CM, and DDFBs are provided. In addition, the aliasing distortions of the partial 4, 8, and 16-band QM-CM, and 4, 8, and 16-band DDFBs are extensively investi-

---

[1] Entire M-band means implementing M analysis and M synthesis filters to evaluate the performance of filter banks.

[2] Partial means implementing some analysis and synthesis filters to evaluate the performance of filter banks.

gated, using the filtering application of three band pass signals. The normalized RMS distortion values of the partial and the entire 4, 8, and 16-band QM-CM, and DDFBs are compared to see the level of aliasing distortion, and a solution to eliminate aliasing distortion of partial QM-CM and DDFBs is introduced. Finally, in Section 2.5, the analyse of MDFT, QM-CM, and DDFBs is concluded.

2.2 A Review of MDFT, QM-CM and DDFBs

In this section, the design methods of the MDFT, QM-CM, and DDFBs, as proposed in the papers [37][34][35], are reviewed in order to illustrate how these filter banks are designed. Each subsection presents a brief overview of the design methods and structures of one of MDFT, QM-CM, or DDFBs. As well, we investigate the various designs of prototype filters, and different modulations such as complex modulation and cosine modulation. In addition, the generation of analysis and synthesis filters is discussed for these filter banks. Finally, the relationship between the input and output of filter banks is provided, and the distortion and aliasing functions are derived from the input and output equations.

2.2.1 MDFT Filter Banks

Overview of MDFT Filter Banks

The MDFT filter banks [37][48]-[50] are complex DFT-modulated filter banks. Figure 2.1 presents the general structure of the M-band MDFT filter bank. The MDFT filter banks design involves a prototype filter with certain requirements, plus complex modulations.

The M-band MDFT filter banks consist of M analysis filters to decompose the input signal into M-bands, and M synthesis filters to reconstruct the processed signal. The down-sampling of each sub-band of the MDFT filter bank is obtained by two steps: the first down-sampler decimates the input signal by a factor of $(M/2)$ (M is the number of bands, and is an even number), and the second down-sampler decimates the signal by two. In addition, the decimation steps are accomplished with and without a delay of one sampling period. Similarly, two interpolation steps are implemented in each sub-band: in the first step the sub-band signal is up-sampled by two, and in the second the signal is up-sampled by $(M/2)$. Similar to the decimation steps, the interpolation steps are performed with and without delay, as illustrated in Figure 2.1.

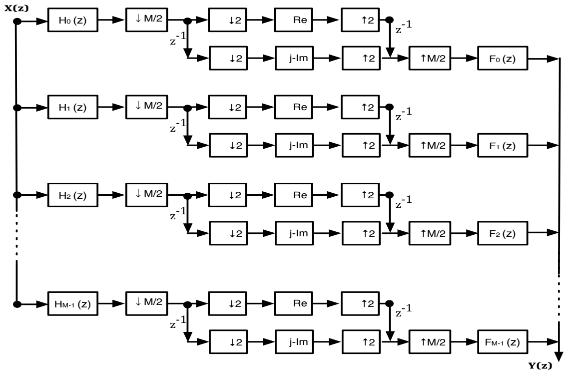

Figure 2.1: M-band MDFT filter bank general structure [37]

Each sub-band of the MDFT consists of a real part and an imaginary part: the real part processes real input signals, and the imaginary part processes imaginary input signals. If the input signal is complex, then the real part processes the real sequence of the input signal and the imaginary part processes the imaginary sequence of the input signal.

The MDFT filter bank can be efficiently realized using two DFT poly-phase filter banks [37][48]-[50], as shown in Figure 2.2. The symbols $G_k(z)$ and $R_k(z)$ represent the type-1 poly-phase of analysis filters and type-3 poly-phase of synthesis filters [38], respectively.

Prototype Filter for MDFT Filter Banks

The prototype filter, $p(n)$, for MDFT filter banks is a zero-phase low-pass filter with a bandwidth of $-\pi/M$ to π/M. The ideal frequency response of the prototype filter is plotted in Figure 2.3. Constrained non-linear optimization techniques [52][53] can be used to design the prototype filters, $P(z)$, that can satisfy the perfect reconstruction (PR) conditions. In [53], low-pass linear phase prototype filters are designed with a length of $N = 4M$; moreover, these prototype filters have stop-band attenuation around $-40\ dB$. In [54], an interesting closed-form equation, Eq. (2.1), is developed to generate low-pass linear phase prototype filters with length of $N = 2M$ and around $-20\ dB$ stop-band attenuation.

$$p(n) = \sqrt{\frac{2}{16} + \frac{1}{8}\cos(\frac{\pi}{2M}(2n + 2M))} \quad where, n = -M + 0.5, \ldots, M - 0.5 \quad (2.1)$$

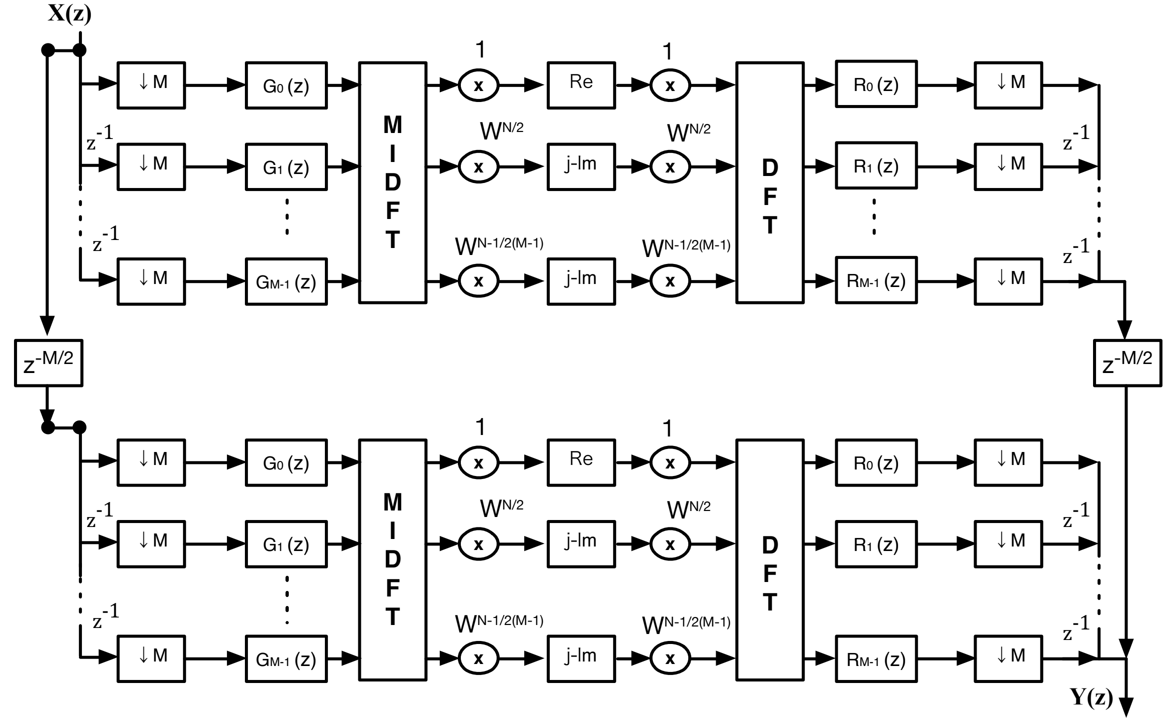

Figure 2.2: Poly-phase realization of MDFT filter bank [37]

Analysis and Synthesis Filters of MDFT Filter Banks

The analysis filters and synthesis filters are derived from a low-pass linear phase prototype filter with complex modulation. The analysis and synthesis filters are linear phase filters because complex modulation does not affect the linear phase property. Eq. (2.2) presents the complex modulation of the prototype filter; moreover, Eq. (2.3) presents the synthesis filters, which equal to the analysis filters. Note that in order to make the filters causal, a delay of $(N-1)/2$ is applied to the prototype filter. The analysis and synthesis can be expressed in z-domain, as in Eq. (2.4).

$$h_k(n) = p_k(n - (\frac{N-1}{2})) = p(n - \frac{N-1}{2}) W_M^{-k(n - \frac{N-1}{2})} \tag{2.2}$$

$$h_k(n) = f_k(n) \tag{2.3}$$

$$p(n)\, is\, the\, prototype\, filter$$

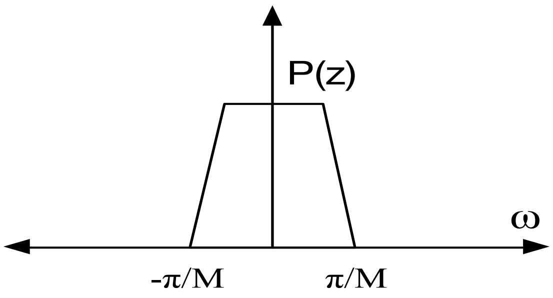

Figure 2.3: Ideal frequency response of low-pass prototype filter for MDFT filter bank

$$n = 0, 1, ..., N-1$$

$$k = 0, 1, ..., M-1$$

$$H_k(n) = F_k = z^{(\frac{N-1}{2})} P_k(z) = z^{(\frac{N-1}{2})} P(zW_M^k) \tag{2.4}$$

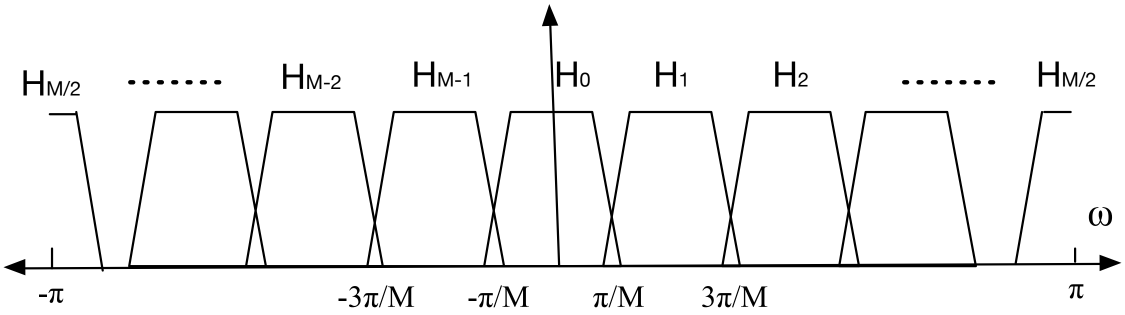

Figure 2.4: Ideal frequency response of low-pass prototype filter for MDFT filter bank

The frequency response of analysis and synthesis filters are shifted versions of the prototype filter. Figure 2.4 illustrates the ideal frequency response of modulated analysis filters. Since the filters have complex coefficients, each filter consists of only one shifted spectrum.

Input and Output Relation of MDFT Filter Banks

The reconstructed signal of MDFT filter banks can be expressed in z-domain as in Eq. (2.5) [37].

$$Y(z) = \frac{z^{-(M/2)}}{2} \sum_{k=0}^{M-1} \sum_{l=0}^{M/2-1} F(z) H(zW_M^{2l}) X(zW_M^{2l}) \tag{2.5}$$

Analyzing the input-output relationship of Eq. (2.5), we notice that the odd aliasing terms are cancelled. This is one advantage of the MDFT filter bank structure. Eq. (2.6) clarifies how the odd aliasing terms are cancelled. For more detail on how the odd aliasing cancelled, see [37].

$$\sum_{l=0}^{M/2-1} X(zW_M^{2l}) \left(\sum_{l=0}^{M/2-1} P(zW_M^{2l}) P(zW_M^{2l+1-2k}) - \sum_{l=0}^{M/2-1} P(zW_M^{2l}) P(zW_M^{2l+1-2k}) \right) = 0 \tag{2.6}$$

The distortion function, Eq. (2.7), of the MDFT filter bank is flat 'all-pass' with a unity gain for all frequencies; moreover, it has a linear phase property because both the analysis and synthesis filters are linear phase. The total aliasing distortion is expressed in Eq. (2.8), and it is almost equal to zero. The MDFT filter bank satisfies the PR conditions since there is no phase distortion, the absolute of amplitude distortion is flat and equal to unity at all frequencies, and the aliasing distortion is almost equal to zero at all frequencies.

$$D(z) = \frac{1}{M} \sum_{k=1}^{M-1} F(z) H(z) \tag{2.7}$$

$$A(z) = \left(\sum_{l=0}^{M/2-1} |\frac{1}{M} \sum_{k=0}^{M-1} F(z) H(zW_M^{2l})|^2 \right)^{1/2} \tag{2.8}$$

2.2.2 QM-CM Filter Banks

Overview of QM-CM Filter Banks

Another class of modulated filter banks is quadrature mirror cosine modulated (QM-CM) filter banks [34][38][42]. The design of QM-CM filter banks totally depends on designing a prototype filter(s) with special properties and real cosine modulations.

The name quadrature mirror implies that the synthesis filters are mirror images of the analysis filters, according to the mirror image condition [34][38]. In [34][52][53], although the QM-CM filter banks are designed using real cosine modulation of a prototype filter, their prototype filters are differently designed. In [52], the prototype filters are obtained by spectral factorization and they are not linear phase; furthermore, the length of the prototype filters are $N = mM$. On the other hand, in [53], the prototype filter is linear phase but not a spectral factor. It is designed using optimization to minimize an objective function, which consists of the overall magnitude distortion and the stop-band attenuation. However, the prototype filter in [34] is constrained to be linear phase and is a spectral factor of a $2Mth$ band filter. The novel design of QM-CM [34] filter banks leads to near-PR filter banks. The filter bank transfer function has a linear phase, and it is free of amplitude distortion. The only error is aliasing distortion; furthermore, the significant aliasing terms are cancelled, but insignificant aliasing error is not cancelled and is comparable to stop-band attenuation.

Figure 2.5 presents the structure of the M-band QM-CM filter banks. The QM-CM filter bank consists of M analysis filters that decompose the spectrum of the input signal into M equally-spaced bands. The analysis filters are followed by down-samplers that expand the spectrum of the signal. After the down-samplers, the signal is up-sampled. The synthesis filters recombine the signal to generate the reconstructed signal.

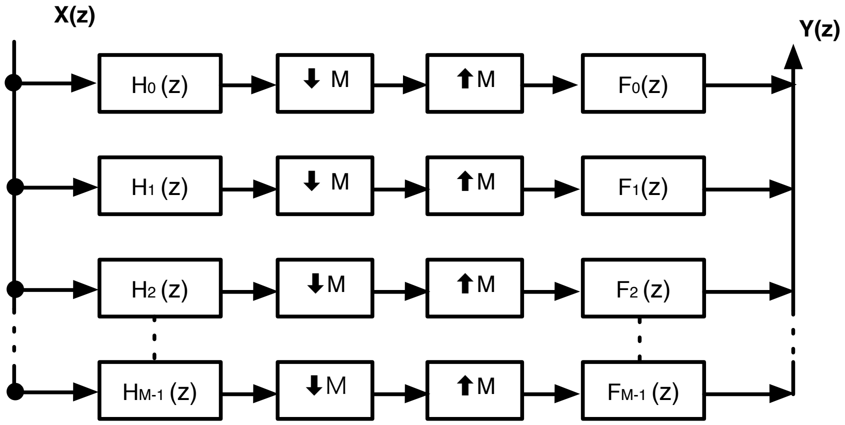

Figure 2.5: Structure of a QM-CM filter bank [34]

Prototype Filter of QM-CM Filter Banks

The prototype filter, $p_0(n)$ in [34], can be designed with either an even or an odd length. For the even length, $N = 2(mM + m_1)$; for the odd length, $N = 2(mM + m1) + 1$, where $0 \leq m_1 \leq M - 1$, and m is an arbitrary positive integer. The prototype filter must be designed to satisfy the linear-phase spectral factor of a $2Mth$ band filter constraint. In addition, *the prototype filter must have very high stop-band attenuation.* The prototype filter has m quadratic constraints, besides the stop-band energy that need to be minimized. Therefore, the prototype filter is designed using non-linear constrained optimization algorithms as in [52][53][55][56]; for more details of the optimization problem formulation, see [34]. Figure 2.6 shows the ideal response of a prototype filter that is symmetric with respect to $\omega = 0$, and with a cutoff frequency of $\pi/2M$.

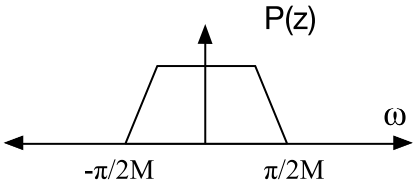

Figure 2.6: Ideal response of a prototype filter in a QM-CM filter bank

Analysis and Synthesis Filters of QM-CM Filter Banks

The analysis and synthesis filters are obtained by cosine modulation of a prototype filter. The modulation of analysis and synthesis filters can be obtained as in Eq. (2.9 a-b).

$$h_k(n) = 2p_k \cos((2k+1)\frac{\pi}{2M}(n - \frac{N-1}{2}) + (-1)^k\frac{\pi}{4}) \tag{2.9a}$$

$$f_k(n) = 2p_k \cos((2k+1)\frac{\pi}{2M}(n - \frac{N-1}{2}) - (-1)^k\frac{\pi}{4}) \tag{2.9b}$$

The analysis and synthesis filters can be expressed in z-domain as in Eq. (2.10); the synthesis filters are the mirror images of the analysis filters. Figure 2.7 shows the ideal response of analysis filters: there are M filters, and they are symmetric with respect to zero frequency.

$$H_k(n) = a_k c_k P_0(zW^{(k+1/2)}) + a_k^* c_k^* P_0 - (zW^{(k+1/2)}) \tag{2.10a}$$

$$F_k(z) = z^{-(N-1)} \widetilde{H}_k(z) \tag{2.10b}$$

$$0 \leqslant k \leqslant M-1$$

$$a_k = e^{j\Theta_k}$$

$$c_k = W^{-(k+1/2)(N-1)/2}$$

$$\Theta_k = (-1)^k \frac{\pi}{4}$$

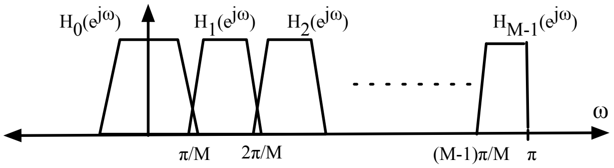

Figure 2.7: The ideal responses of analysis filters, and they are symmetric with respect to zero frequency

Input and Output Relation of QM-CM Filter Banks

The input and output of a QM-CM filter bank are related as in Eq. (2.11). Furthermore, the distortion function and aliasing distortion of the filter bank are denoted by D(z) in Eq. (2.12), and A(z) in Eq. (2.13), respectively.

$$Y(z) = \frac{1}{M} \sum_{k=0}^{M-1} \sum_{l=0}^{M-1} F(z) H(zW_M^l) X(zW_M^l) \tag{2.11}$$

$$D(z) = \frac{z^{-1}}{M} \sum_{k=0}^{M-1} F(z) H(z) \tag{2.12}$$

$$A(z) = \left(\sum_{l=0}^{M-1} | \frac{1}{M} \sum_{k=0}^{M-1} F(z) H(zW_M^l)|^2 \right)^{1/2} \tag{2.13}$$

The transfer function, D(z), is a delay and the significant aliasing terms in Eq. (2.13) are cancelled. Therefore, the only aliasing error that remains is small, and it is comparable to stop-band attenuation of the prototype filter $p_0(n)$.

2.2.3 Directly Designed Filter Banks (DDFBs)

Overview of DDFBs

The DDFBs [35] are designed using optimization, where the optimization problem is formulated as two equivalent quadratic functions. Each objective function consists of two terms: the first term is the PR condition, and the second term is the stop-band energy of the analysis and synthesis filters. The optimization problem is approached by iteratively minimizing the weighted square root error of the objective functions. The DDFBs [35] design method is generally used to design various types of filter bank, such as uniform and non-uniform filter banks. Furthermore, critically-sampled and over-sampled uniform filter banks can be designed; as well, the method can be used to design non-uniform filter banks with compatible and non-compatible sampling sets.

Figure 2.8 illustrates the general structure of the DDFBs. Note that in the case of a maximally-decimated uniform filter bank, each factor in the sampling vector $n_0, n_1, \cdots, n_{M-1}$ is equal to M, so the sampling vector is equivalent to $M, M, \cdots, M$. The structure of DDFBs consists of the analysis bank followed by the synthesis bank, which is the same as the general design of a filter bank structure.

Analysis and Synthesis Filters of DDFBs

The analysis and synthesis filters of modulated filter banks are obtained with proper modulation of one or more prototype filter(s). However, the approach to obtain analysis and synthesis filters with DDFBs is totally different. With DDFBs, the coefficients of analysis and synthesis filters are directly obtained. The variables used in the formulation of the quadratic objective functions are the analysis filters' coefficients and the synthesis filters' coefficients. During the minimization of the two objective functions, each iteration the synthesis filters' coefficients are kept fixed and the analysis filters' coefficients are updated; then, the analysis filters' coefficients are kept fixed

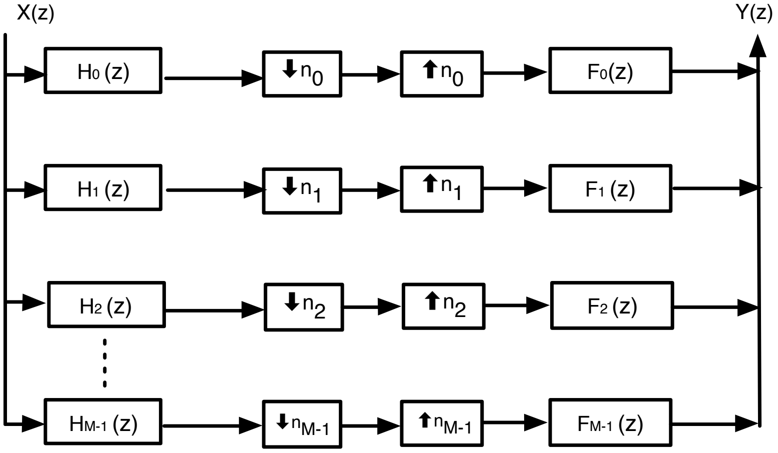

Figure 2.8: General structure of DDFBs [35]

and the synthesis filters' coefficients are updated, until the functions converge. Once the functions converge, the final analysis filters' coefficients and synthesis filters' coefficients are obtained. After the convergence, the frequency response of analysis and synthesis filters of DDFBs [35] has *significantly high stop-band attenuation* and some ripples in its pass band; however, the total filter bank response is ripple-free.

Input and Output Relation of DDFBs

The relationship between the input and output of the DDFBs can be expressed mathematically, as in Eq. (2.14). Looking at Eq. (2.14), we can express the distortion function and aliasing function, as in Eq. (2.15) and Eq. (2.16)[35], respectively.

$$Y(z) = \frac{\alpha_{k,l}}{n_k} \sum_{k=0}^{M-1} \sum_{l=0}^{M-1} F(z)H(zW_M^l)X(zW_M^l) \tag{2.14}$$

$$D(z) = \frac{z^{-\triangle}}{n_k} \sum_{k=0}^{M-1} F(z)H(z) \tag{2.15}$$

$$A(z) = \sum_{k=0}^{M-1} \sum_{k=1}^{M-1} \frac{\alpha_{k,l}}{n_k} F(z)H(zW_M^l) \tag{2.16}$$

2.3 Performance Analyses of the Entire M-band MDFT, the Entire M-band QM-CM, and the Entire M-band DDFBs

In this section, a thorough study to compare the performance of the entire M-band MDFT, QM-CM, and DDFBs is discussed in detail. First of all, the comparison criteria are defined in order to make the comparison equitable. In addition, the PR conditions are highlighted for filter bank systems. Several 2M-band MDFT, M-band QM-CM, and M-band DDFBs are designed and their amplitude distortion and aliasing error are presented and compared.

2.3.1 Comparison Schemes

In order to make the comparison between the entire M-band MDFT, QM-CM, and DDFBs reasonable, the length equivalence of filters, and the symmetry of the frequency response of filter banks are considered during the comparison.

The first important aspect concerns the number type of the filters' coefficients: real or complex. The analysis and synthesis filters of the MDFT filter banks have complex coefficients, which means that if the length of a filter is N, then there are $2N$ coefficients: N real coefficients, and N imaginary coefficients. On the other hand, both the QM-CM and the DDFBs have real coefficients. Therefore, during the design and comparison, double the filter's length as in the MDFT filter bank will be used in the QM-CM and the DDFBs filters. In other words, if the length of the MDFT filters is N, then a length of $2N$ will be used for the filters of QM-CM and DDFBs. The second important aspect is the symmetry of frequency response in each type of filter. Because the MDFT filters are complex, their frequency responses are a shifted version of the prototype filter: each filter has a single spectrum as a frequency response. Conversely, the QM-CM and DDFBs filters possess symmetric properties: each filter of the CM-QM and the DDFBs has two spectra, which are symmetric around the zero frequency.

Combining these two aspects, the coefficient types and the frequency response symmetry, leads to the requirement to design and compare $2M$-band MDFT filter banks with (a filter length of N), M-band QM-CM filter banks with (a filter length of $2N$), and M-band DDFBs with (a filter length of $2N$).

2.3.2 Perfect Reconstruction Conditions

The PR system must have its output equal to the delayed version of its input. This can be achieved if the system satisfies the following three conditions:

1. The transfer function is all-pass with a unity gain for all frequencies, which ensures that there is no amplitude distortion;
2. The phase response of the transfer function is linear, which guarantees that there is no phase distortion; and,
3. Aliasing Distortion is equal to zero for all frequencies. Systems with very small aliasing distortion can approximate the PR system [38].

All of the MDFT filter banks [37] and the DDFBs [35] are designed to satisfy PR system performance; however, the QM-CM [34] approximate the PR system because their aliasing error is comparable to stop-band attenuation.

2.3.3 Performance of the Entire M-band MDFT, the Entire M-band QM-CM, and the Entire M-band DDFBs

Eight-band MDFT, 4-band QM-CM, and 4-band DDFBs Performance

The length of the analysis and synthesis filter of the 8-band MDFT is ($N = 4M$), ($N = 32$) complex coefficients; these coefficients are obtained from [37]. However, the length of 4-band QM-CM and 4-band DDFBs is ($N = 64$) real coefficients; these coefficients are obtained from [57][58]. Note that the length of filters is equivalent for all filter banks because although the 8-band MDFT has only 32 complex coefficients, the number of bands is different. Figures 2.9, 2.10, and 2.11 present aliasing distortion and amplitude distortion for the 8-band MDFT, the 4-band QM-CM, and the 4-band DDFBs.

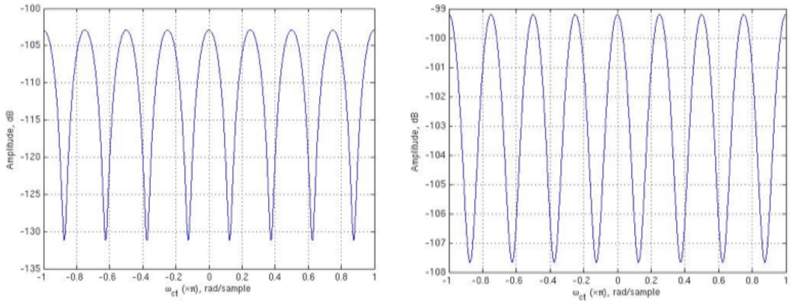

Figure 2.9: Aliasing and amplitude distortion for the 8-band MDFT FB

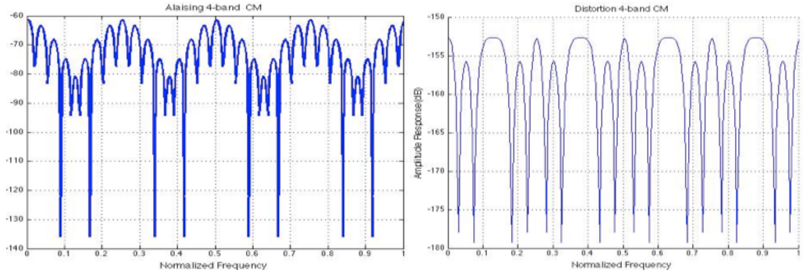

Figure 2.10: Aliasing and amplitude distortion for the 4-band QM-CM FB

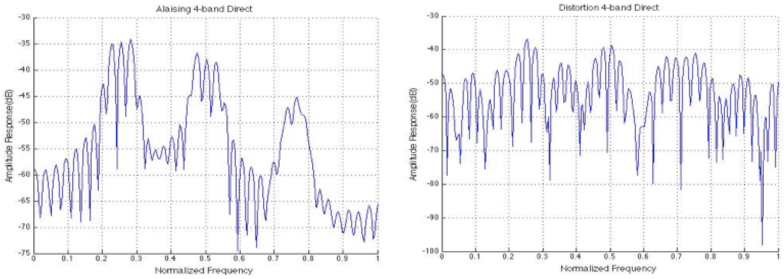

Figure 2.11: Aliasing and amplitude distortion for the 4-band DDFBs

Sixteen-band MDFT, 8-band QM-CM, and 8-band DDFBs Performance

In this subsection, we double the number of bands and the length of filters to examine the amplitude distortion and aliasing distortion with more bands and longer filters. The length of the analysis and synthesis filters of the 16-band MDFT ($N = 4M$), ($N = 64$) complex coefficients; these coefficients are obtained from [37]. While, the length of the 8-band QM-CM and the 8-band DDFBs filters is ($N = 128$) real coefficients; these coefficients are obtained from [57][58]. Figures 2.12, 2.13, and 2.14

illustrate aliasing distortion and amplitude distortion for 16-band MDFT, 8-band QM-CM, and 8-band DDFBs.

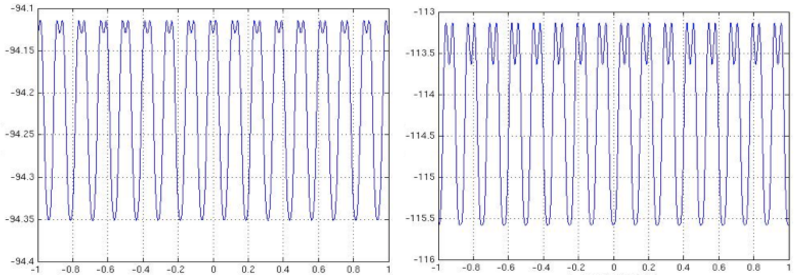

Figure 2.12: Aliasing and amplitude distortion for the 16-band MDFT FBs

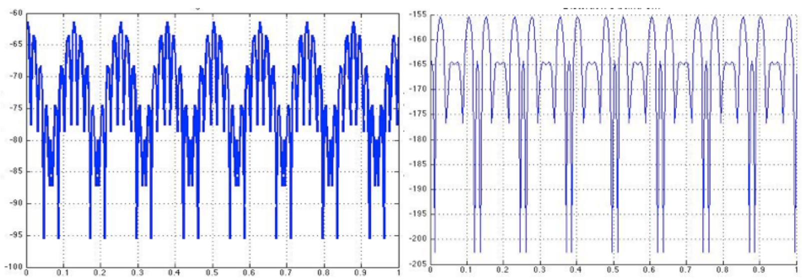

Figure 2.13: Aliasing and amplitude distortion for the 8-band QM-CM FBs

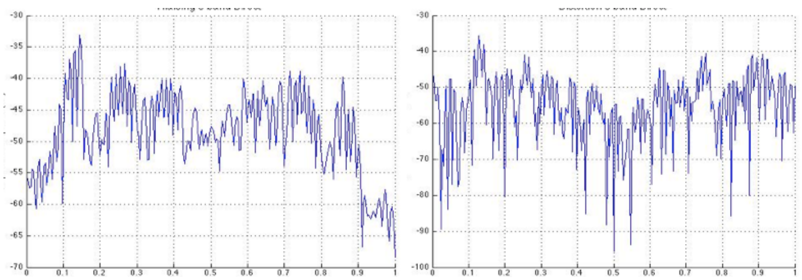

Figure 2.14: Aliasing and amplitude distortion for the 8-band DDFBs

Thirty-two-band MDFT, 16-band QM-CM, and 16-band DDFBs Performance

In this test, we further increase the number of bands and the number of coefficients, for the analysis and synthesis filters of all filter banks, to check the amplitude distortion and the aliasing errors. The length of the analysis and synthesis filter of the 32-band

MDFT is ($N = 4M$), ($N = 128$) complex coefficients; these coefficients are obtained from [37]. Similarly, the length of the 16-band QM-CM and the 16-band DDFBs filters is ($N = 256$) real coefficients; these coefficients are obtained from [57][58]. All filter banks have the same length because the MDFT have complex coefficients; however, their band numbers are different. Figures 2.15, 2.16, and 2.17 show the aliasing distortion and the amplitude distortion for the 32-band MDFT, the 16-band QM-CM, and the 16-band DDFBs.

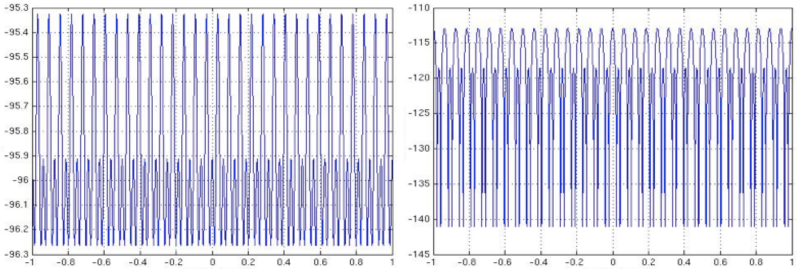

Figure 2.15: Aliasing and amplitude distortion for the 32-band MDFT FB

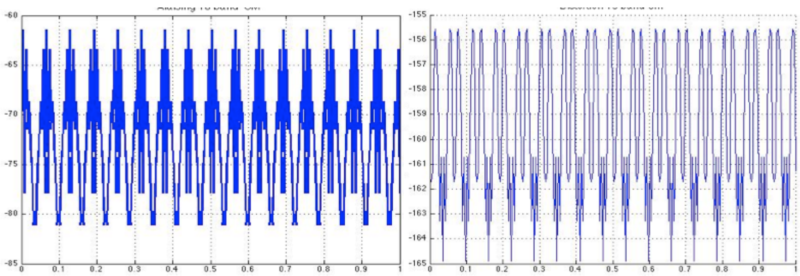

Figure 2.16: Aliasing and amplitude distortion for the 16-band QM-CM FB

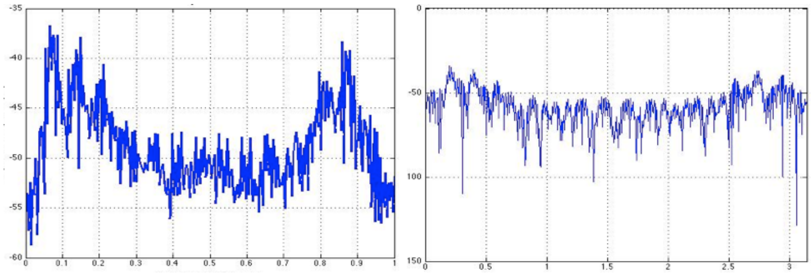

Figure 2.17: Aliasing and amplitude distortion for the 16-band DDFBs

2.3.4 Comparison of MDFT, QM-CM and DDFBs Performance

In the previous subsections, several 2M-band MDFT filter banks, M-band QM-CM filter banks, and M-band DDFBs are designed, and their amplitude distortion and aliasing distortion are presented. In this subsection, the aliasing error and amplitude distortion are compared.

Figure 2.18 shows the aliasing error for the MDFT filter banks, the QM-CM filter banks, and the DDFBs. The 8-, 16-, and 32-band MDFT filter banks outperform all filter banks in term of minimum aliasing distortion. The 4-, 8-, and 16-band QM-CM filter banks have insignificant aliasing error of about -60 dB, which is comparable to the stop-band attenuation of their prototypes filters. However, the 4-, 8-, and 16-band DDFBs have aliasing error around -40 dB; however, the DDFBs can perform better if N, the length of filter, is increased for the analysis and synthesis filters.

The amplitude distortion for the MDFT filter banks, the QM-CM filter banks, and the DDFBs is illustrated in Figure 2.19. The 4-, 8-, and 16-band QM-CM filter banks achieve the best performance among all filter banks, with amplitude distortion levels around -150 dB and less. Similarly, the 8-, 16-, and 32-band MDFT filter banks have excellent performance with insignificant amplitude distortion less than -100 dB Conversely, the 4-, 8-, and 16-band DDFBs have higher amplitude distortion than the other filter banks, with values around -40 dB. Of note, the transfer functions of the MDFT, QM-CM, and DDFBs is linear phase; therefore, there are no phase distortion for all presented filter banks.

In conclusion, although the MDFT prototype filters have stop-band attention around -45 dB, the MDFT filter banks match PR system conditions because their aliasing error is insignificant, and their amplitude distortion is relatively very small along the lines of -100 dB. Similarly, the QM-CM filter banks excellently approximate the performance of PR systems. Significantly, the QM-CM filter banks have low amplitude distortion; as well, the aliasing distortion is very low, and it is comparable to stop-band attenuation, with values less than -60 dB. Moreover, the analysis and synthesis filters of QM-CM filter banks have high stop-band attention of around -80 dB. Finally, although the DDFBs performance shows high amplitude distortion and aliasing error, the DDFBs filters have very high stop-band attenuation. Therefore, the DDFBs may approximate the PR properties, and their design is more flexible than the other two filter banks. The performance of the DDFBs can be adequately improved to meet the PR system performance, with less amplitude and aliasing distortion, if the length of their analysis and synthesis filters is increased. This is because the design of DDFBs depends on optimizations; therefore, if the length of filter increases, the degree of freedom increases for obtaining better performance.

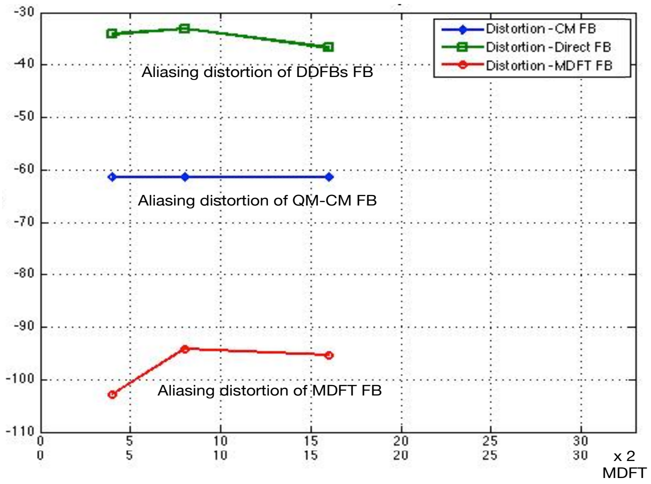

Figure 2.18: The aliasing error for the MDFT FBs, QM-CM FBs and DDFBs

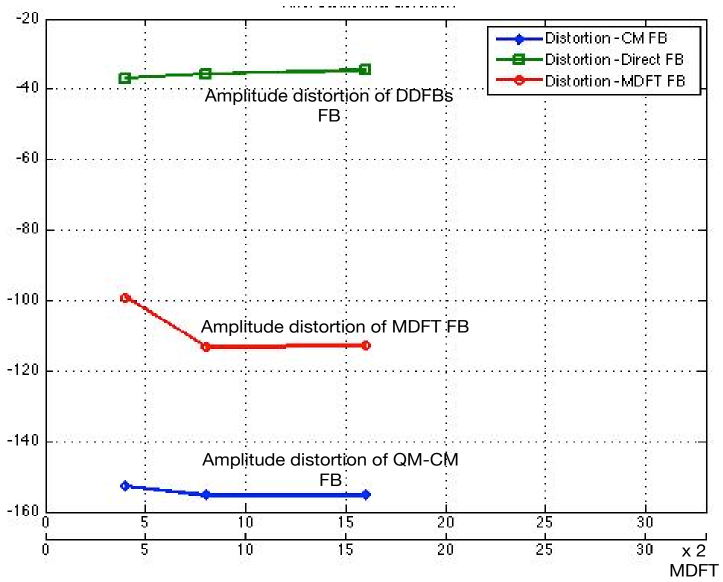

Figure 2.19: Amplitude distortion for the MDFT FBs, QM-CM FBs and DDFBs

2.4 Analysis of Partial MDFT FBs, QM-CM FBs, and DDFBs and Filtering Applications

It is important to implement partial filter banks in some digital signal processing applications, such as implementation of 3D frustum filters [32][33]. In addition, in other applications, it is computationally efficient to process a band pass signal with a partial filter bank that has a band pass bandwidth, instead of the entire M-band filter bank.

In this section, we study partial MDFT filter banks, partial QM-CM filter banks, and partial DDFBs. The distortion and aliasing errors of the partial MDFT, QM-CM, and DDFBs are analysed. In addition, partial-filtering applications using the partial QM-CM and DDFBs are examined. The normalized RMS distortion values of the partial filter banks and the entire filter banks are evaluated to compare the distortion effects of partial filter banks.

2.4.1 Analysis of Aliasing Distortion for Partial MDFT FBs, QM-CM FBs and DDFBs

In Section 2.3, the analyses of the PR conditions are presented and we conclude that the entire M-band MDFT filter banks are PR systems. Moreover, the entire M-band QM-CM filter banks, and the entire M-band DDFBs approximate the PR systems because these filter banks have insignificant aliasing and amplitude distortions. In this section, we analyse the partial filter banks.

Analysis of Partial MDFT FBs

The M analysis and synthesis filters of the MDFT filter bank are complex modulation of a prototype filter; therefore, the frequency response of each filter occupies a single spectrum. Furthermore, the M-band MDFT filter bank has $(M-1)/2$ aliasing terms because the odd aliasing terms are cancelled, as in Eq. (2.6). The total aliasing distortion of each band is approximately equal to zero. This is can be verified by Eq. (2.17), because both analysis filters and synthesis filter can be expressed in terms of a prototype filter [37][59].

$$F(z)H(zW_M^{2l}) \simeq 0 \tag{2.17a}$$

$$z^{-(N-1)}P_k(z)P_k(zW_M^{2l}) \simeq 0 \tag{2.17b}$$

$$z^{-(N-1)}P(zW_M^{k})P(zW_M^{2l+k}) \simeq 0 \tag{2.17c}$$

$$z^{-(N-1)}P(z)P(zW_M^{2l}) \simeq 0 \tag{2.17d}$$

In order to check the aliasing distortion, we implement (using Matlab) a partial band pass with $|0.25 - 0.75|\pi$ of a 32-band MDFT filter bank. Figure 2.20 shows the amplitude response (blue) and the aliasing distortion (red) for the partial 32-band MDFT with a band pass of $|0.25 - 0.75|\pi$. The aliasing error is suppressed, and it is equivalent to stop-band attenuation [59]. Figure 2.20 confirms Eq. (2.17), and it shows that the partial MDFT filter banks have aliasing distortion compared to stop-band attenuation of its filters at around -45 dB; therefore, the partial MDFT filter banks approximate the PR conditions, because there is only small aliasing distortion.

Figure 2.20: Band pass amplitude response (blue) and the aliasing distortion (red) of partial MDFT filter bank

Analysis of Partial QM-CM FBs

The QM-CM filter bank has real analysis and synthesis filters because the cosine modulation is real; consequently, the frequency response of each modulated filter consists of a symmetric spectrum. Each sub-band of the M-band QM-CM filter banks has M-1 aliasing terms. If all bands of the M-band QM-CM filter bank are used, then the aliasing terms cancel each other leading to a filter bank that is almost aliasing-free, as per Subsection 2.2.2. However, if a low-pass portion of the QM-CM filter bank is implemented, then an aliasing term of around -10 dB at the high edge is not cancelled. Similarly, if a high-pass portion of the QM-CM filter bank is used, then an aliasing term of around -10 dB at the low edge is not cancelled. Hence, if a band pass portion of the QM-CM filter bank is implemented, then two aliasing terms at the edges of the band pass are not cancelled. Figure 2.21 illustrates the amplitude response (blue) and aliasing distortion (red) for a partial 16-band QM-CM filter bank with a band pass equal to $|0.25 - 0.75|\pi$. The two aliasing terms have distortion of around -10 dB at the edges. As a result, in filtering applications, these aliasing distortion terms may distort the edges of filtered signals.

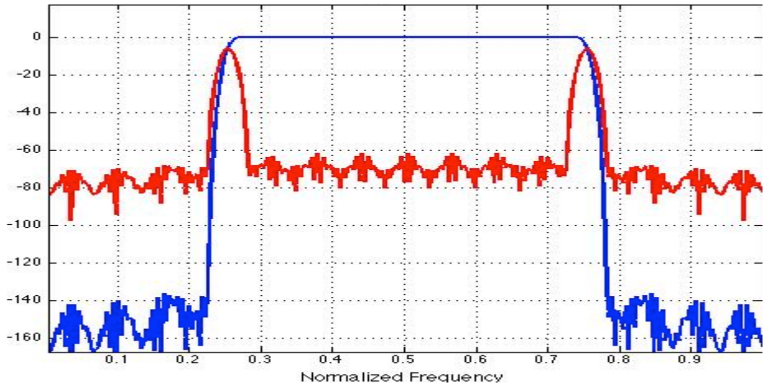

Figure 2.21: Band pass amplitude response (blue) and the aliasing distortion (red) of partial 16-band QM-CM filter bank

Analysis of Partial DDFBs

The DDFBs have real analysis and synthesis filters; thus, the frequency response of each filter consists of a symmetric spectrum. Each sub-band of the M-band DDFBs consists of $M-1$ aliasing terms. If all bands of a filter bank are implemented, the aliasing terms of the bands cancel each other. Similar to QM-CM filter banks, if a low-pass portion of the DDFBs is implemented, then one aliasing term at the high edge remains. Similarly, if a high-pass part of the DDFBs is used, then one aliasing term at the low edge is not cancelled. Therefore, if a band pass part of the DDFBs is used, two aliasing terms on the high and low edges remain. Figure 2.22 illustrates the amplitude response (blue) and aliasing distortion (red) for a partial 16-band DDFBs with a band pass equal to $|0.25 - 0.75|\pi$. The two aliasing terms have distortion around -10 dB on the edges. During filter applications of a band pass signal, aliasing may affect the edges of the filter signals.

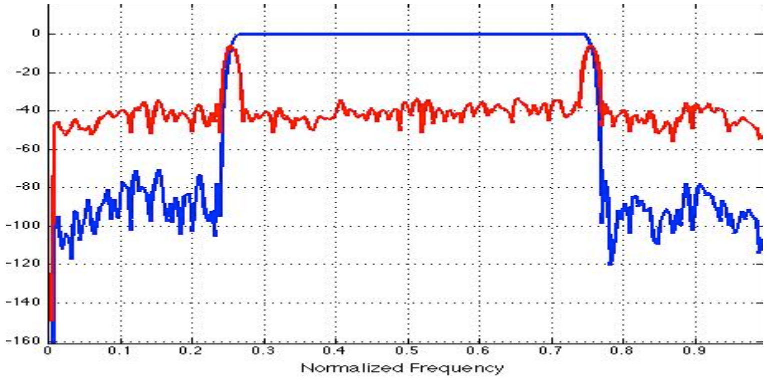

Figure 2.22: Band pass amplitude response (blue) and aliasing distortion (red) of partial 16-band DDFBs filter bank.

2.4.2 Analysis of Aliasing Distortion for the Partial QM-CM and DDFBs, with Filtering Applications

As mentioned in Subsection 4.2.1, the aliasing distortion for the partial band pass QM-CM and DDFBs may affect the edges of signals. In order to objectively evaluate the effect of the aliasing distortion of the partial QM-CM and DDFBs, filtering applications of both are tested. In this subsection, filtering applications for the entire M-band QM-CM and DDFBs and for the partial M-band QM-CM and DDFBs are implemented to compare aliasing distortion. We evaluate the normalized RMS distortion values [60] for both the entire M-band QM-CM and DDFBs, and for the partial band pass QM-CM and DDFBs. Then, we objectively compare the normalized RMS distortion values of the entire M-band QM-CM and DDFBs with the partial band pass QM-CM and DDFBs. During filtering applications, three band pass signals, with bandwidths of $[0.25 - .75]\pi$, $[0.30 - .70]\pi$, and $[0.35 - .65]\pi$, are used which are shown in Figures 2.23a, 2.23b, and 2.23c, respectively. These choices of band pass are preferred because the band pass of all partial filter banks is $[0.25 - .75]\pi$. The 4-band, 8-band, and 16-band QM-CM and DDFBs with the entire M-band, or partial band pass of $[0.25 - .75]\pi$, are used in filtering applications. Table 2.1 presents the normalized RMS distortion values of the filtered signals using these entire M-band and partial band pass QM-CM and DDFBs. Figures 2.24 and 2.25 illustrate the three original signals (blue) and the three filtered signals (red), using partial band pass 16-band QM-CM and DDFBs. In addition, Figures 2.26 and 2.27 present the three original signals (blue) and the three filtered signals (red), using the partial band pass 4-band QM-CM and DDFBs.

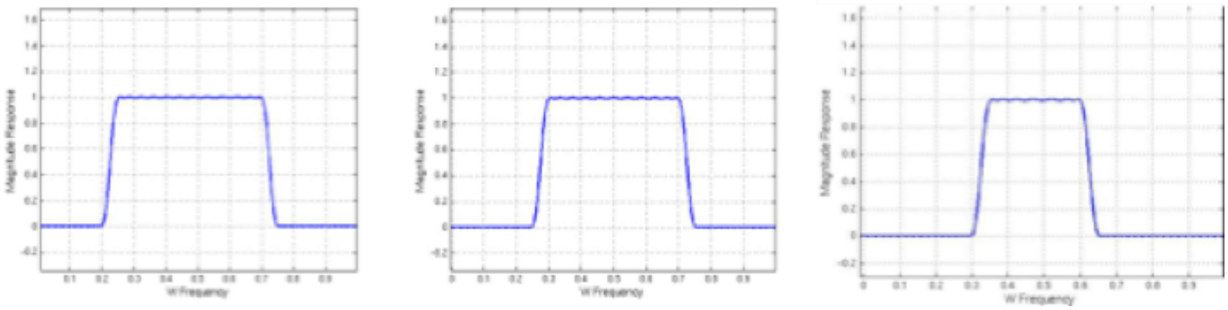

a. **[0.25-.75]π** **b.** **[0.30-.70]π** **c.** **[0.35-.65]π**

Figure 2.23: Three band pass signals, with bandwidths of: a. $[0.25 - .75]\pi$, b. $[0.30 - .70]\pi$, and c. $[0.35 - .65]\pi$.

Figures 2.24 and 2.25 are showing the partial 16-band QM-CM and DDFBs, it is obvious that the band pass signals with a bandwidth of $[0.25 - 0.75]\pi$ have a small distortion in the left edges; however, the $[0.30 - 0.70]\pi$ and $[0.35 - .65]\pi$ band pass signals are not distorted. The normalized RMS distortion values for the partial QM-CM and DDFBs confirm that the distortion for the band pass signals with a bandwidth of $[0.25 - 0.75]\pi$ are small values in the order of 10^{-3}. Furthermore, the normalized RMS distortion values of the partial QM-CM and DDFBs for the other two band pass signals are very tiny and are almost equal to the normalized RMS distortion values of the entire M-band QM-CM and DDFBs.

A glance at Figures 2.26 and 2.27 shows that the partial 4-band QM-CM and DDFBs affect the filtered band pass signals with bandwidths of $[0.25 - .75]\pi$ and $[0.30 - 0.70]\pi$ from the edges only, while the band pass signal with a bandwidth of $[0.35 - 0.65]\pi$ is not distorted at all. The normalized RMS distortion values of the partial 4-band QM-CM and DDFBs demonstrate that the first two band pass signals have small distortions in the order of 10^{-3}; furthermore, they show that the last band pass signal is not corrupted by the partial 4-band QM-CM and DDFBs, and that their normalized RMS distortion values are comparable to RMS distortion values of the entire M-band QM-CM and DDFBs.

To conclude, the filtering performance of partial 8- and 16-band QM-CM and

signal bandwidth	Normalized RMS Distortion Values 4-band Filter Banks			
	Partial QM-CM	Entire QM-CM	Partial DDFBs	Entire DDFBs
$[0.25$ - $.75]\pi$	0.0044	1.1523×10^{-5}	0.0038	3.1246×10^{-4}
$[0.30$ - $.70]\pi$	0.0030	1.0598×10^{-5}	0.0012	2.5328×10^{-4}
$[0.35$ - $.65]\pi$	2.3344×10^{-4}	1.0980×10^{-4}	3.0112×10^{-4}	2.7801×10^{-4}
	Normalized RMS Distortion Values 8-band Filter Banks			
	Partial QM-CM	Entire QM-CM	Partial DDFBs	Entire DDFBs
$[0.25$ - $.75]\pi$	0.0080	1.3563×10^{-5}	0.0067	1.9644×10^{-4}
$[0.30$ - $.70]\pi$	8.9060×10^{-4}	1.2240×10^{-5}	3.0334×10^{-4}	1.6919×10^{-4}
$[0.35$ - $.65]\pi$	1.2892×10^{-4}	1.2519×10^{-5}	1.9839×10^{-4}	1.6644×10^{-4}
	Normalized RMS Distortion Values 16-band Filter Banks			
	Partial QM-CM	Entire QM-CM	Partial DDFBs	Entire DDFBs
$[0.25$ - $.75]\pi$	0.0072	1.6471×10^{5}	0.0052	8.8075×10^{-5}
$[0.30$ - $.70]\pi$	2.1929×10^{-5}	1.5797×10^{-5}	3.4871×10^{-4}	8.6241×10^{-5}
$[0.35$ - $.65]\pi$	1.2282×10^{-4}	1.7872×10^{-5}	3.0096×10^{-4}	8.9969×10^{-5}

Table 2.1: Normalized RMS Distortion Values of all QM-CM and DDFBs filtered signals

DDFBS, with the two band pass signals with bandwidths of $[0.30-0.70]\pi$ and $[0.35-0.65]\pi$, is similar to the entire 8- and 16-band QM-CM and DDFBs, because the normalized RMS distortion values assure that there is no distortion. However, the band pass signals with a bandwidth of $[0.25-0.75]\pi$ have a small distortion in the order of 10-3. Additionally, the filtering performance of the partial 4-band QM-CM and DDFBs with the third band pass signal is equivalent to the performance of the entire 4-band QM-CM and DDFBs, while the performance of the partial 4-band QM-CM and DDFBs with the first two signals show small distortion in the order of 10^{-3}. The analysis confirm that the partial QM-CM and DDFBs have small distortion at the edges of the filtered signal.

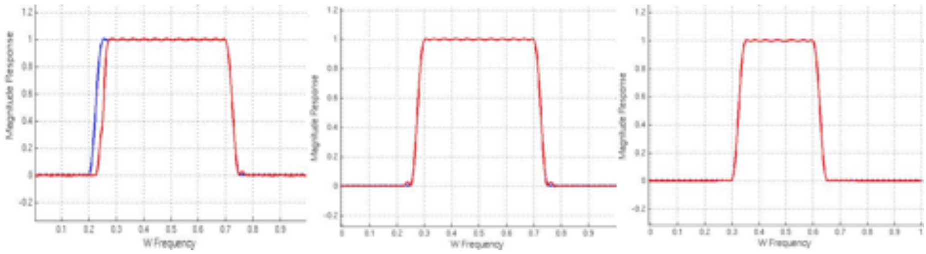

Figure 2.24: The three original signals (blue) and the three filtered signals (red) of the partial 16-band QM-CM with band pass of $[0.25 - .75]\pi$

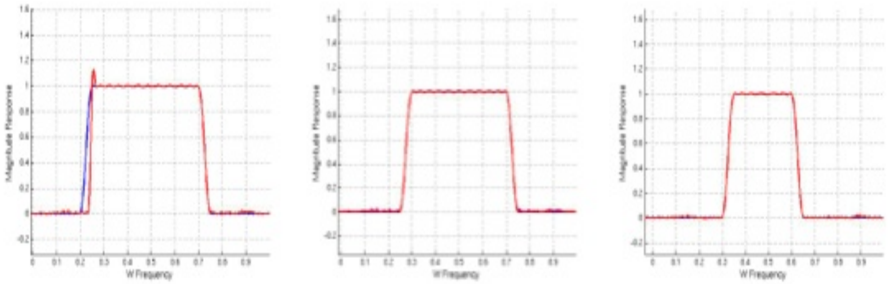

Figure 2.25: The three original signals (blue) and the three filtered signals (red) of the partial 16-band DDFBs with band pass of $[0.25 - .75]\pi$

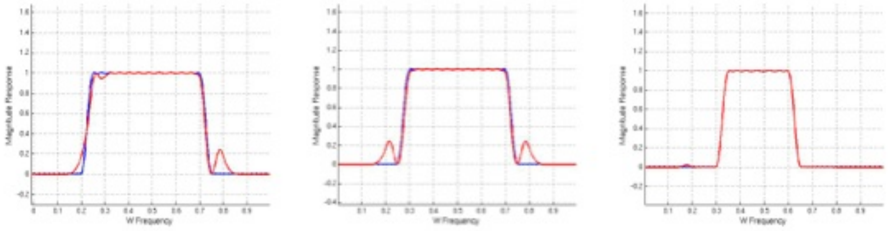

Figure 2.26: The three original signals (blue) and the three filtered signals (red) of the partial 4-band QM-CM filter bank with band pass of $[0.25 - 0.75]\pi$.

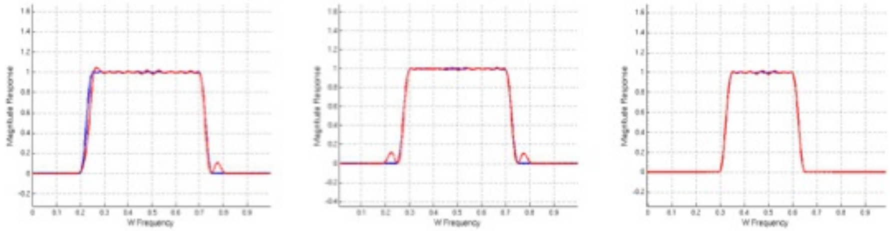

Figure 2.27: The three original signals (blue) and the three filtered signals (red) of the partial 4-band DDFBs with band pass of $[0.25 - 0.75]\pi$

2.4.3 Aliasing Distortion Cancellation for Partial QM-CM and DDFBs

Section 2.4.2 covered the aliasing distortion of the partial band pass QM-CM and DDFBs in filtering applications. Although the aliasing distortion is not severe, it can be permanently cancelled. The cancellation of aliasing can be achieved by introducing similar but negative aliasing distortion to the system [59]. In other words, if there is one aliasing term that is not cancelled, an opposite aliasing term is introduced to the system to eliminate the original aliasing term and to obtain an aliasing-free system. Similarly, if the system has two aliasing terms, two similarly negative aliasing terms are implemented with the system to totally cancel aliasing.

Figures 2.21 and 2.22 illustrate the amplitude responses and the aliasing distortion of the partial 16-band QM-CM and DDFBs. In the each figure, two aliasing terms remain: one is at the low edge, and the second is at the high edge. With appropriate analysis of the partial filter banks, we can introduce negative aliasing terms to totally cancel the aliasing distortion.

In Figures 2.21 and 2.22, eight analysis and synthesis filters, specifically the 5^{th} to 12^{th} filters, are used in the implementation of the partial 16-band QM-CM and DDFBs. There are two aliasing terms: the aliasing term at the low edge is introduced from the 5^{th} filter, and the aliasing term at the high edge is introduced from the 12^{th} filter. Two proper aliasing terms, one at the low edge and one at the high edge, must be subtracted from the system to eliminate aliasing distortion. The choice of the two terms depend on the number of bands and M^{th} filters implemented to obtain the partial filter banks. The low-edge aliasing term can be appropriately chosen by Eq. (2.18), following these steps:

1. Set min to the lowest-used M^{th} filter; and,

2. Set M to the number of bands in the filter bank.

$$Aliasing\,term\,(l) = M - min + 1 \qquad Filter\,number\,(k) = min - 1 \tag{2.18}$$

$$we\,can\,write\,the\,term\,of\,analysis\,and\,synthesis\,filter\,as:$$

$$-F(z)_k H_k(zW_M^l)$$

Similarly, the high edge aliasing term can be appropriately chosen by Eq. (2.19), following these steps:

1. Set max to the highest-used M^{th} filter; and,

2. Set M to the number of bands in the filter bank.

$$Aliasing\,term\,(l) = M - max \qquad Filter\,number\,(k) = max + 1 \tag{2.19}$$

$$we\,can\,write\,the\,term\,of\,analysis\,and\,synthesis\,filter\,as:$$

$$-F_k(z)H_k(zW_M^l)$$

Note that both Eq. (2.18) and (2.19) are valid for any partial band pass QM-CM and DDFBs.

The aliasing terms in Figures 2.21 and 2.22 can be cancelled by introducing two aliasing terms for each system. The following step illustrate the choices:

The partial filter banks are 16-band, and only the 5^{th} to 12^{th} filters are implemented: therefore,

$$M = 16$$

$$max = 12\,the\,maximum\,M^{th}\,filter\,used$$

$$min = 5\,the\,minimum\,M^{th}\,filter\,used$$

To cancel the low edge aliasing term, the following term is introduced

$$Alising\,term\,(l) = 16 - 5 + 1 = 12$$

$$filter\,number\,(k) = 5 - 1 = 4$$

$$-F_4(z)H_4(zW_M^{12})$$

$$That\,is\ ,12^{th}\,aliasing\,term\,of\,the\,4^{th}\,filter$$

To cancel the high edge aliasing term, the following term is introduced

$$Alising\,term\,(l) = 16 - 12 = 4$$

$$filter\,number\,(k) = 12 + 1 = 13$$

$$-F_{13}(z)H_{13}(zW_M^{4})$$

$$that\,is\,,\ 4^{th}\,aliasing\,term\,of\,the\,13^{th}\,filter$$

Figures 2.28 and 2.29 present the amplitude response and the aliasing distortion for partial 16-band QM-CM and DDFBs, respectively, after introducing the appropriate terms to eliminate aliasing distortion.

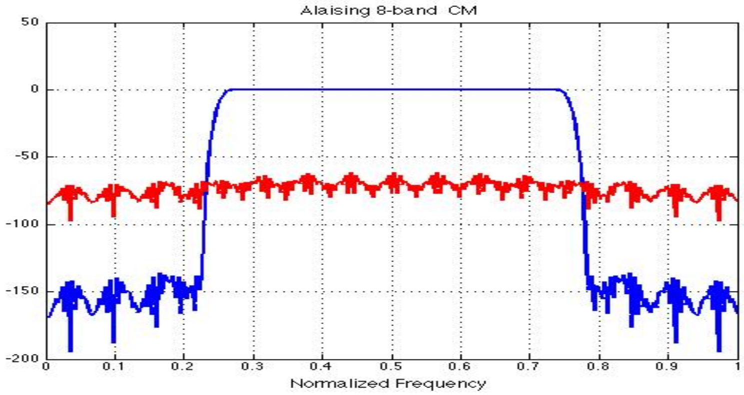

Figure 2.28: The amplitude response (blue) and the aliasing distortion (red) for the partial 16-band QM-CM with band pass of after introducing the appropriate aliasing cancellation terms

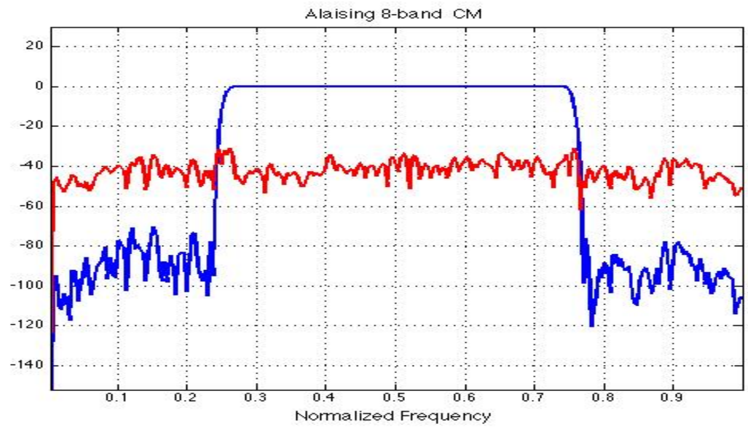

Figure 2.29: The amplitude response (blue) and the aliasing distortion (red) for the partial 16-band DDFBs with band pass of after introducing the appropriate aliasing cancellation terms

2.5 Summary

In conclusion, the analysis and the review of the MDFT [37], QM-CM [34], and DDFBs [35] illustrate that the design of MDFT and QM-CM filter banks is simple, because they require only designing a prototype filter(s) with pulse complex or cosine modulations. These prototype filters can be designed using optimization, or other methods, such as close form. On the other hand, the DDFBs are achieved directly with optimization technique, without requiring modulation. Moreover, the design method is more broad and flexible, because various filter banks can be designed.

The entire M-band MDFT filter banks outperform the entire M-band QM-CM and DDFBs in term of minimal aliasing distortion. The entire M-band QM-CM filter banks have insignificant aliasing distortion, which is comparable to the stop-band attenuation of their filters. The entire M-band DDFBs have higher aliasing distortion compared to MDFT and QM-CM; however, this aliasing distortion can be minimized if the length of the filter increases. In terms of amplitude distortion, the entire M-band QM-CM filter banks have the least among all filter banks. The amplitude distortion of entire M-band MDFT filter banks is insignificant; however, it is around -40 dB for the DDFBs. The DDFBs and QM-CM filters have significantly high stop-band attenuation while the MDFT filters have stop-band attenuation around -40 dB.

After analysis, it is concluded that the partial band pass MDFT filter banks have small aliasing distortion, which is equivalent to the stop-band attenuation of their filters. On the other hand, the partial band pass QM-CM and DDFBs have aliasing distortion at the edges. The filtering applications of band pass signals verify that this aliasing distortion is not severe and it has an insignificant impact, in the order of 10^{-3}, on the filtered signals. Moreover, introducing similar but negative aliasing distortion to the systems can eliminate aliasing distortion of partial band pass QM-CM and DDFBs.

Chapter 3

A Review of Non-uniform Filter Banks (NUFBs)

3.1 Introduction

Although uniform filter banks (UFBs) have fulfilled several digital signal processing applications [38]-[47] that require uniform divisions of the spectrum of signals, there are many other applications - such as digital image processing, audio signal processing for hearing aids, etc. [61][62][63][64][65][66][67][68][69][70][71] that demand non-uniform time-frequency signal decomposition and processing. In addition, non-uniform filter banks (NUFBs) can improve computational efficiency of some applications that are processed with UFBs.

NUFBs have a structure similar to UFBs because both filter banks consist of analysis filters, down-samplers, up-samplers, and synthesis filters. However, the responses of NUFBs filters are, as the name implies, non-uniformly spaced. Figures 3.1 and 3.2 illustrate the differences between the frequency response of NUFBs and UFBs, respectively. In addition to frequency responses differences, NUFBs can have integer or rational decimation factors. Therefore, the structures of NUFBs can be categorized into NUFBs with integer decimation factors Figure 3.3, and NUFBs with rational decimation factors Figure 3.4. The difference between the two is that NUFBs with rational decimation factors have an extra up-sampler before the analysis filters, and an extra down-sampler after the synthesis filters.

In this chapter, a review and analysis of NUFBs is presented. An overview of the development of the theory and design methods of NUFBs is introduced in Section

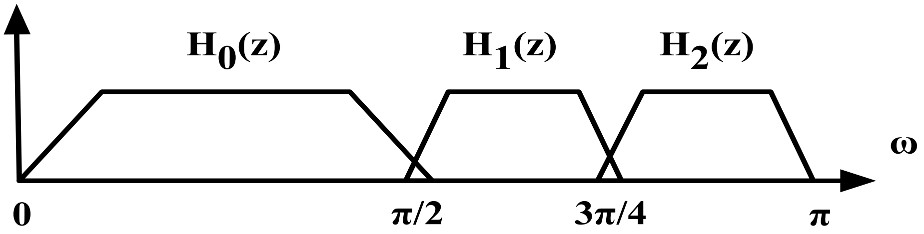

Figure 3.1: Ideal frequency response of an analysis bank of [2 4 4] NUFBs

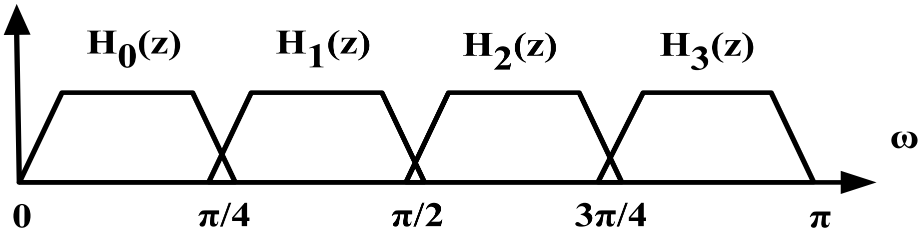

Figure 3.2: Ideal frequency response of an analysis bank of [4 4 4 4] UFBs

3.2. In Section 3.3, a detailed study of QM-CM NUFBs [36] is presented, including an overview of their design method, and the analysis of the generation of NUFBs from an equivalent UFB, with illustrative examples. The concept of feasibility [36] of sampling sets is reviewed and verified with examples. In Section 3.4, we further investigate the use of DDFBs [35] for the design of NUFBs. The aliasing cancellation in NUFBs using the pairing-up concept is clarified with an example. A summary is presented in Section 3.5.

3.2 The Development of NUFBs: Theories and Designs

In literature various studies and analyses have been conducted in order to develop and design NUFBs to meet many requirements in various applications. Generally, the design of NUFBs can be classified as either direct or indirect. The direct NUFBs can be designed directly using optimization and other techniques; however, the indirect NUFBs require using various modulated UFBs in combination, or through cascading various prototype filters to obtain the required frequency bandwidth, as in the tree

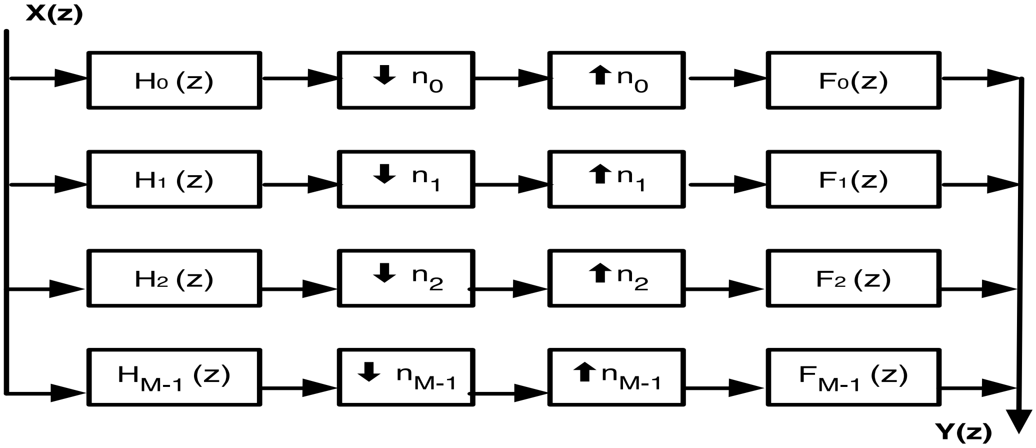

Figure 3.3: Structure of NUFBs with integer sampling factors [71]

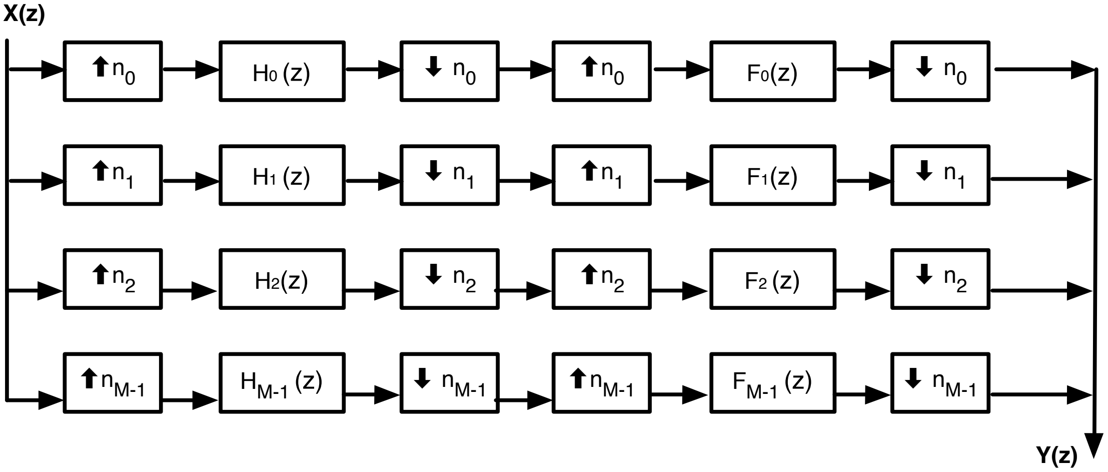

Figure 3.4: Structure of NUFBs with rational sampling factors [71]

structure method [38]. NUFBs with integer and rational decimation factors can also be designed using direct and indirect methods.

The simplest NUFBs can be obtained by cascading two-band QM-CM UFBs, as in the tree structure filter bank method [38](See chapter 5.8 for more detail). Several NUFBs with different integer decimation factors can be implemented using the tree structure method. Figure 3.5 illustrates the implementation of a NUFB, with decimation factor [2 4 8 8], from two-band UFBs using the tree structure method. In addition to simplicity, the use of the tree structure method can achieve PR NUFBs, as long as the basic two-band UFB satisfies the PR conditions [38] (See chapter 5.8 for more detail). Another similar but interesting design proposes using tree structure methods with the aid of optimization to design NUFBs with integer sampling factors [66][67]. Basically, these methods involve designing several prototype filters, using windowing techniques like Blackman in method [66] and modified Cosh, Exponential, and Kaiser in [67]. In both methods [66][67], the required NUFBs are constructed with a tree structure by using these designed prototype filters. Then, the magnitude response is minimized in order to improve the cutoff frequency of each constructed filter. The simulation results in [66][67] show that the aliasing error and amplitude distortion in both methods are insignificant and that near-PR systems can be achieved. Although the simplicity is an attractive feature of the tree structure technique, it suffers drawbacks; for instance, the limitation of the decimation factors. Moreover, the repeatable cascading of prototype filters results in a longer delay.

In 1989, the theory and design of NUFBs started to evolve. In [68], the authors study and analyse indirect NUFBs in order to derive the necessary conditions to eliminate aliasing distortion, and minimize the amplitude and phase distortion. Maximally decimated QM-CM NUFBs are analysed in [68], and can be defined, as in Eq. (3.1).

$$\sum_{k=0}^{M-1} 1/n_k = 1 \tag{3.1}$$

$$n_k \ are \ the \, sampling \, factors$$

As a result of [68]'s study of NUFBs, the concept of compatibility of decimation factors is introduced as a necessary condition to obtain aliasing cancellation: **Compatibility is defined as: For any decimation set** $[n_1, n_2, ..., n_{M-1}]$**, each sampler** n_k **must be a factor of any other sampler** n_k **[68][69].** Similarly, the authors of [69][70] investigate the design of NUFBs and develop other necessary and sufficient conditions for achieving PR systems. Moreover, an algorithm is developed in [70] to find a closed compatible set of any given sampling set.

In [71][72], a novel time-domain analysis method is introduced to analyse the design of NUFBs; it is an extension of time-domain analysis used for UFBs [51]. This method analyses NUFBs in the time domain, derives the PR conditions in matrix and vector formulation, and uses iterative optimization techniques to achieve PR conditions, as well as some frequency specification conditions. The time-domain analysis implements direct NUFBs with integer decimation factors, rational decimation factors, and block decimation - which consists of rational decimation factors [72]. The

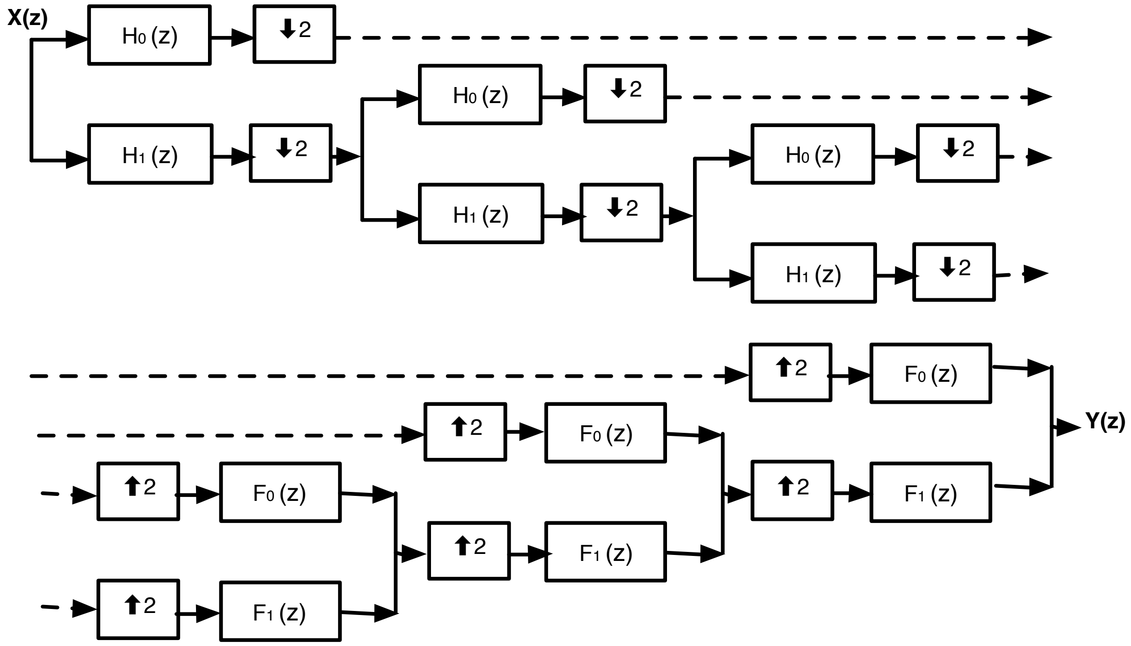

Figure 3.5: The implementation of [2 4 8 8] NUFBs from two-band UFBs using the tree structure method [38]

method analyses the NUFBs in three parts: the analysis bank, the down/up sampling, and the synthesis bank; and then these parts are combined to express the total system input-output equation. In addition, special modifications are applied to NUFBs with rational decimation, so they can be analysed and treated like integer ones. NUFBs with block decimation [72] can be approached both directly and indirectly. In the direct approach, the system is analysed directly and a set of time-domain conditions is derived; however, in the indirect approach, the system is converted into an equivalent parallel uniform system and then is analysed. The analysis in [71]-[72] concerns NUFBs with compatible sampling sets. In [73], the authors investigate the problem of aliasing cancellation of NUFBs with incompatible decimation factors, where it is impossible to obtain PR systems as in [68]. In [73] the authors approach the problem of NUFBs with incompatible factors by presenting each filter with several filters, in order to increase the degree of freedom to achieve almost PR systems. In [74], dual-rate structure succeeds in eliminating impossible aliasing distortion in NUFBs with incompatible sampling sets, as in [68]. A similar design format [35], explained previously in Subsection 2.2.3, is used to design UFBs and NUFBs with compatible and incompatible decimation factors. The problem in [35] is formulated in frequency-domain as a Toeplitz matrix and is solved by optimizations. In Section 3.4, we will review how aliasing is cancelled in the case of NUFBs.

In [75], Liu and Bruton have presented a NUFB design method for arbitrary two-band rational decimation factor. The design method is based on the QM UFBs and it involves optimization in order to achieve an almost PR system. The optimization involves minimizing the aliasing error and amplitude distortion function; therefore, the error function consists of an aliasing term and a distortion term in the frequency-domain. The method shows excellent results, with minimal aliasing and distortion error. Furthermore, in [76], Liu and Bruton have extended the method in [75] to design any M-band NUFB. Similarly in [77], a frequency-domain formulation method for designing direct NUFBs with integer and rational sampling factors is proposed. In this method, the PR conditions of distortion function and aliasing function are formulated in frequency-domain as least-square error. Then, minimizing the least-square errors solves the problem. Interestingly, the method can also be used to design linear phase NUFBs.

One indirect method in designing NUFBs emerges from the combination of uniform cosine-modulated (CM) and quadrature mirror cosine modulated (QM-CM) filter banks. The method is simple and it shows great success in achieving near-PR non-uniform systems. In [36][78][79], the authors propose simple indirect design methods for NUFBs from CM [78][79] and QM-CM filter banks [36]. The non-uniform method reported in [36] will be studied in detail in Section 3.2. In [78][79], the CM NUFBs are designed from CM UFBs by combining adjacent analysis and synthesis uniform filters to form the desirable non-uniform response; moreover, the conditions of feasibility, aliasing cancellation, and minimal distortions are investigated.

Another similar and simple method to indirectly design NUFBs to achieve near-PR with linear phase property, is called *Partial cosine-Modulation* [80][81]. In this method both the analysis and synthesis filters of the NUFBs are obtained from two low-pass and two high-pass prototype filters for the analysis and synthesis banks, with cosine modulations. This method is called partial cosine-modulation because the analysis and synthesis filter are obtained by modulation of various prototype filters. Furthermore, the authors investigate and analyse the effect of phase angle on aliasing, in order to achieve better performance. With the partial cosine-modulation method, linear phase NUFBs with integer and rational decimation factors, that achieve near-PR with small aliasing error, can be designed.

In [82][83][84], two different methods are proposed to design Discrete Fourier Transform (DFT) NUFBs. In [82], the design is approached by semi-definite programming techniques to achieve a near-PR system. The formulation of the optimization problem is aimed at minimizing an objective function, which consists of aliasing distortion, while constrained the magnitude and phase distortions to a prescribed level. Alternatively, in [83] the method of designing the DFT NUFBs is an extension of DFT UFBs in [84]. In [83], the design method follows a very interesting approach to minimizing the aliasing distortion, phase distortion, and magnitude distortion. The design method involves two steps: firstly, instead of cancelling aliasing error in the analysis bank, the analysis bank is design to have minimal aliasing error; secondly, in order to suppress this minimal aliasing error, the synthesis bank is designed to make the analysis bank response coincides with the synthesis bank response.

In [85][86][87], direct-design techniques of NUFBs with linear phase property, with integer and rational decimation factors are proposed. The design problem in [85] is specified with a set of conditions on the integer samplers and aliasing terms. Therefore, the problem is *simplified to design several individual filters* that lead to near-PR systems, with less effort and low complexity. The authors extend the design method in [85] to a broad design method that involves the design of linear phase NUFBs with a rational decimation set. The direct-design methods in [85]-[87] are relatively simple, with low delay and high stop-band attenuation.

3.3 Review of QM-CM NUFBs Design

The idea of designing QM-CM NUFBs in [36] is based on combining relevant filters in QM-CM UFBs [34] to get the desired non-uniform bands. This method is simple and straightforward because it only requires designing a prototype type filter, cosine-modulation, and combination of modulated filters. In this method, maximally decimated as per Eq. (3.1) near-PR QM-CM NUFBs can be designed, *if the decimation factors are feasible*; feasibility is defined with examples below. In the case of infeasible sampling sets, aliasing cannot be cancelled with direct implementation; however, aliasing cancellation can be achieved by a modified structure, for details, see [36].

Definition of feasibility [36]

Consider a sampling set $n_i = [n_0, n_1, ..., n_{m-1}]$, where $i = 0, 1, ..., m-1$; and let M be the least common multiple of n_i. Let us define $R_i = M/n_i$. For a given feasibility set, where $k = 0, 1, ..., m-1$:

$$\sum_{k=0}^{k-1} R_k = R_k P_k \tag{3.2}$$

$$P_k\, must\, be\, an\, integer\, for\, k = 0, 1, ..., m-1$$

Examples: Lets consider two sampling sets: Case A: n_i = [2 6 3] and Case B: n_i = [6 2 3]

Case A:

$$n_i = [2\,6\,3]$$

$$The\, least\, common\, multiple\, , M = 6$$

$$R_i = M/[2\,6\,3] = [3\,1\,2\,]$$

$$\sum_{k=0}^{k-1} R_k = R_k P_k$$

$$**\, for\, k = 0$$

$$\sum_{k=0}^{-1} R_k = R_0 P_0$$

$$3 = 3P_0 \Rightarrow P_0 = 1$$

$$**\, for\, k = 1$$

$$\sum_{k=0}^{0} R_k = R_1 P_1$$

$$3 = 1P_1 \Rightarrow P_1 = 3$$

$$**\, for\, k = 2$$

$$\sum_{k=0}^{1} R_k = R_2 P_2$$

$$4 = 2P_2 \Rightarrow P_2 = 2$$

$$in\, case\, A,\, we\, conclude\, that\, all\, P_k\, are\, integers;\, therefore,\, the\, set\, is\, feasible.$$

Case B:

$$n_i = [6\,2\,3]$$

$$The\,least\,common\,multiple\,,M = 6$$

$$R_i = M/[6\,2\,3] = [1\,3\,2\,]$$

$$\sum_{k=0}^{k-1} R_k = R_k P_k$$

$$**\,for\,k = 0$$

$$\sum_{k=0}^{-1} R_k = R_0 P_0$$

$$1 = 1P_0 \Rightarrow P_0 = 1$$

$$**\,for\,k = 1$$

$$\sum_{k=0}^{0} R_k = R_1 P_1$$

$$1 = 3P_1 \Rightarrow P_1 = 1/3$$

$$**\,for\,k = 2$$

$$\sum_{k=0}^{1} R_k = R_2 P_2$$

$$4 = 2P_2 \Rightarrow P_2 = 2$$

$$in\,case\,B,\;we\,see\,that\,P_1\,is\,not\,an\,integer;\;therefore,\;the\,set\,is\,infeasible.$$

3.3.1 Analysis and Synthesis Filters of QM-CM NUFBs

Generally, the analysis and synthesis filters of QM-CM NUFBs [36] can be obtained directly by merging relevant analysis and synthesis filters of equivalent QM-CM UFBs [34]. For clarity, let us consider an example of NUFBs with sampling set [2 4 4]. First, we first design an equivalent QM-CM UFB with sampling set with [4 4 4 4], and then we combine the first and second filters of the analysis and synthesis banks to obtain the required bandwidth. Figures 3.6 and 3.7 illustrate the structure of the equivalent

UFB and NUFB.

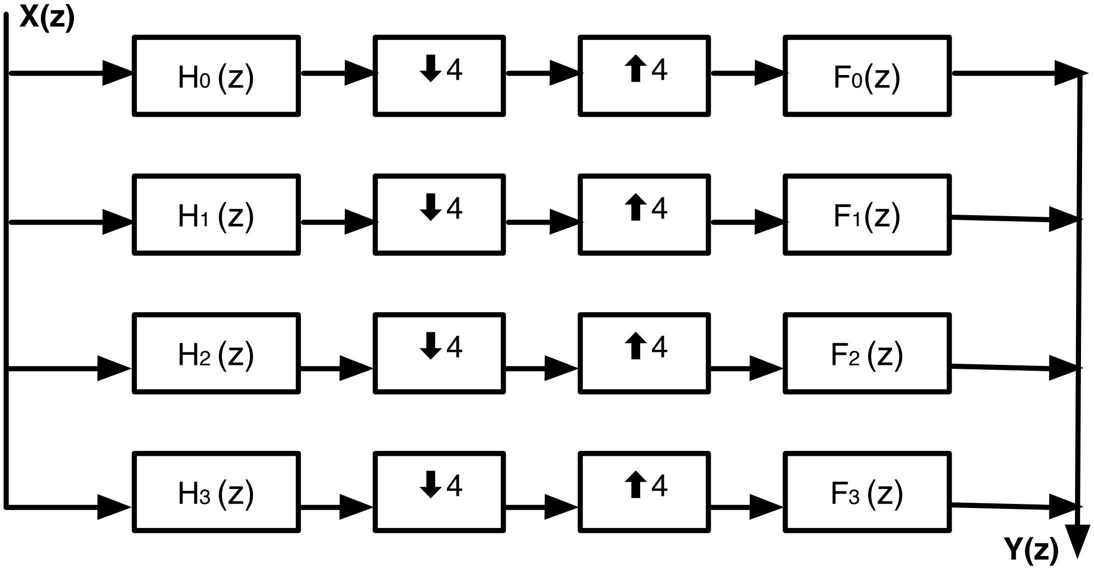

Figure 3.6: The structure of an equivalent UFB with sampling factors [4 4 4 4]

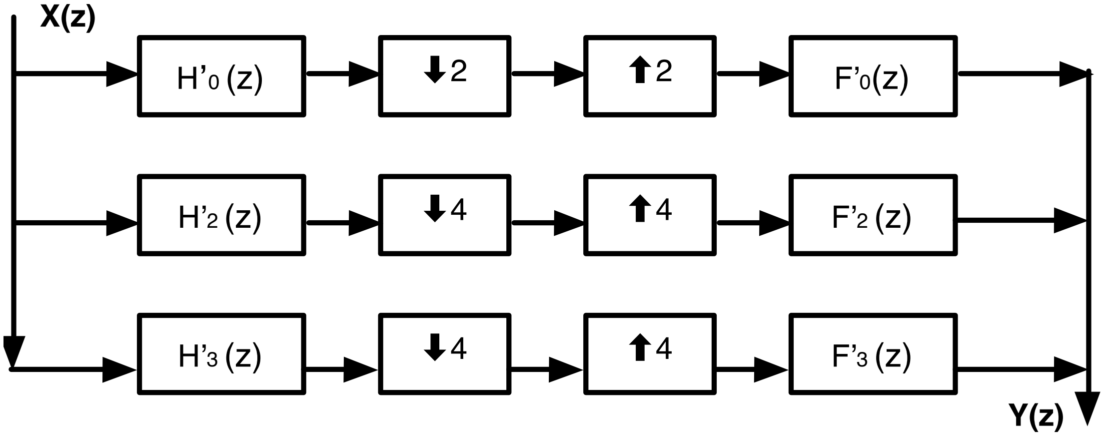

Figure 3.7: The structure of NUFBs with sampling factors [2 4 4]

Let the analysis and synthesis filter of the UFB equal to Eq. (3.3):

$$\begin{aligned} H_k(z) &= H_k(z) \\ F_k(z) &= F_k(z) \\ for\, k &= 0, 1, 2, 3 \end{aligned} \tag{3.3}$$

Now, the analysis and synthesis filters of NUFB can be derived from the UFB as in Eq. (3.4), (3.5)

$$\begin{aligned} &for\, k = 2, 3 \\ &\acute{H}_k(z) = H_k(z) \\ &\acute{F}_k(z) = F_k(z) \end{aligned} \tag{3.4}$$

$$\begin{aligned} &however\, for\, k = 0 \\ &\acute{H}_k(z) = \frac{1}{\kappa}\sum_{k=0}^{1} H_k(z) \\ &\acute{F}_k(z) = \frac{1}{\kappa}\sum_{k=0}^{1} F_k(z) \\ &\kappa = \frac{M}{n_i} \end{aligned} \tag{3.5}$$

As illustrated, non-uniform bands can be obtained by merging the relevant uniform bands of an equivalent UFB. This merging concept is applicable for a feasible set only.

3.3.2 Input and Output Relation of QM-CM NUFBs

The input and output of QM NUFBs are related, as in Eq. (3.6). Further, the amplitude distortion, $D(z)$, and aliasing distortion, $A(z)$, of the filter bank is represented by Eq. (3.7) and Eq. (3.8), respectively.

$$Y(z) = \sum_{k=0}^{M-1}\sum_{l=0}^{n_k-1} \frac{1}{n_k}\acute{F}(z)\acute{H}(zW_M^l)X(zW_M^l) \tag{3.6}$$

$$D(z) = z^{-1}\sum_{k=0}^{M-1} \frac{1}{n_k}\acute{F}(z)\acute{H}(z) \tag{3.7}$$

$$A(z) = \sum_{k=0}^{M-1}\sum_{l=1}^{n_k-1} \frac{1}{n_k}\acute{F}(z)\acute{H}(zW_M^l) \tag{3.8}$$

The amplitude distortion function, $D(z)$, has insignificant distortion. On the other hand, the aliasing function consists of two parts: first-order aliasing, which is a result of adjacent bands, and higher-order aliasing, which is a result of non-adjacent bands [36]. The higher-order aliasing is considered significant compared to first-order aliasing; therefore, the first-aliasing part is cancelled but the second-aliasing can only be minimized to obtain a near-PR system.

3.3.3 An Illustrative Example of QM-CM NUFBs

In order to illustrate the performance of QM-CM NUFBs [36], an example of implementing a QM-CM NUFB with decimation factors [2 4 4] from an equivalent QM-CM FB with decimation factors [4 4 4 4] is demonstrated; as first presented in Subsection 3.3.1. The length of the analysis and synthesis filters is equal to 64. The frequency response of the analysis filters, total amplitude distortion, and aliasing distortion of the QM-CM NUFB are presented in Figures 3.8 to 3.10. The results show that the frequency response of the filters has no ripples in pass band, and the distortion function is almost flat. In addition, the aliasing distortion is insignificant, and it is comparable to the stop-band of the filters.

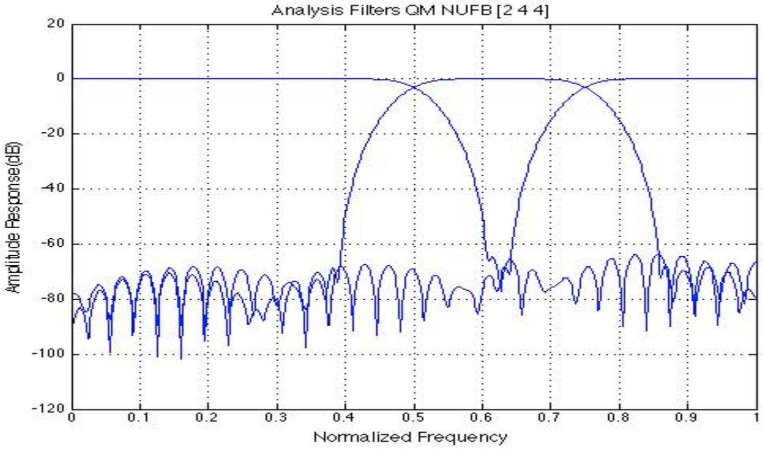

Figure 3.8: Frequency response of [2 4 4] QM-CM NUFBs

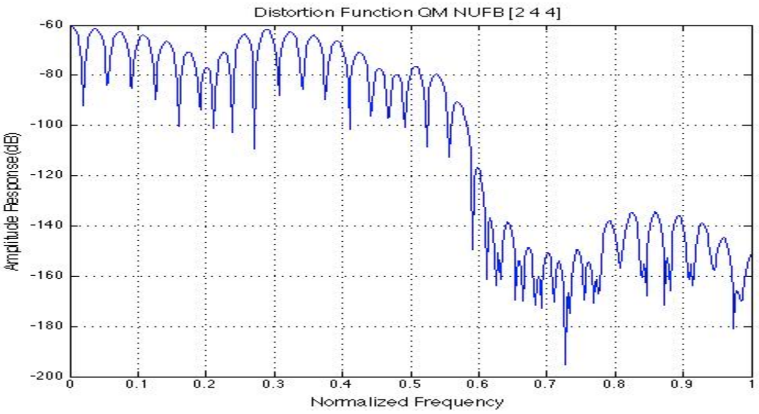

Figure 3.9: Amplitude distortion of [2 4 4] QM-CM NUFBs

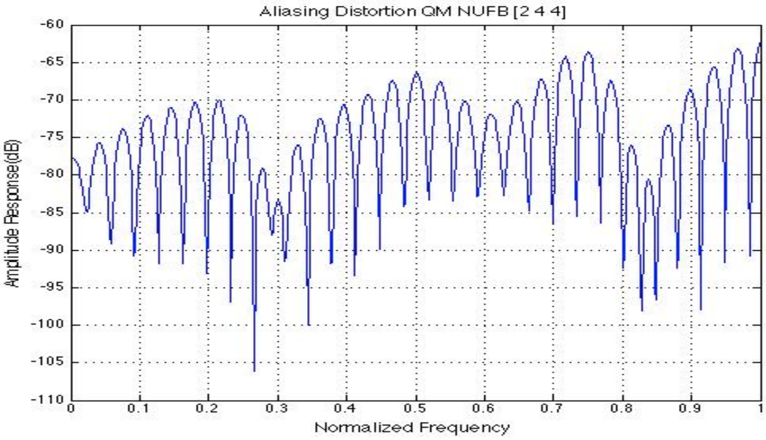

Figure 3.10: Aliasing distortion of [2 4 4] QM-CM NUFBs

3.4 Review of Directly Design Non-uniform Filter bank

In Subsection 2.2.3, we reviewed and analysed the design of DDFBs [35]. The method in [35] is used to design UFBs and NUFBs with compatible and incompatible sampling sets. See Subsection 2.2.3 for an overview of the problem formulation, generation of analysis and synthesis filters, input and output relation analysis, and distortion analysis; further details can be found in [35]. In this section, we investigate one important concept in aliasing cancellation for the case of NUFBs. This concept is known as pairing-up of aliasing components [35][68].

3.4.1 Aliasing Cancellation with Pairing up

Let us recall the PR conditions for DDFBs, as shown in Eq. (2.14) to (2.16) from Subsection 2.2.3. In [35], the PR condition is formulated as a linear equation, just like Eq. (3.9):

$$\mathbf{H}f = b \tag{3.9}$$

H is a Toeplitz matrix consisting of analysis filters coefficients and aliasing terms.
f is a column vector consists of synthesis filters coefficient.
b is a column vector consists of zeros except one element.

This linear equation represents the convolution operation between the analysis and synthesis filters. Considering PR conditions in frequency-domain, Eq. (3.9) can be presented as a matrix and vector multiplication, as in Eq. (3.10):

$$\begin{bmatrix} \frac{1}{n_0}H_0(z) & \cdots & \frac{1}{n_{M-1}}H_{M-1}(z) \\ \vdots & \ddots & \vdots \\ \frac{\alpha}{n_0}H_0(zW_M^l) & \cdots & \frac{\alpha}{n_{M-1}}H_{M-1}(zW_M^l) \end{bmatrix} \times \begin{bmatrix} f_0(z) \\ \vdots \\ f_{M-1}(z) \end{bmatrix} = \begin{bmatrix} 1 \\ 0 \\ 0 \end{bmatrix} \tag{3.10}$$

Alpha, α must be equal to:

$$\alpha_{k,l} = \begin{cases} 1 & \text{for } W_M^l \in \{e^{\frac{2\pi(1)}{n_k}}, \cdots, e^{\frac{2\pi(n_k-1)}{n_k}}\} \\ 0 & \text{otherwise} \end{cases}$$

This operator,α , ensures that the aliasing term is set to zero, if it does not occur in the M^{th} sub-band. However, when the aliasing term shows up in the M^{th} sub-band, the factor α is set to unity. This is the idea of pairing-up aliasing components; below, an example of a NUFB with sampling set of [2 4 4] is presented for clarification. The PR condition can be written in matrix and vector formulation in the frequency domain as:

$$\begin{bmatrix} \frac{1}{2}H_0(z) & \frac{1}{4}H_1(z) & \frac{1}{4}H_2(z) \\ \frac{0}{2}H_0(ze^{\frac{j2\pi(1)}{4}}) & \frac{1}{4}H_1(ze^{\frac{j2\pi(1)}{4}}) & \frac{1}{4}H_2(ze^{\frac{j2\pi(1)}{4}}) \\ \frac{1}{2}H_0(ze^{\frac{j2\pi(2)}{4}}) & \frac{1}{4}H_1(ze^{\frac{j2\pi(2)}{4}}) & \frac{1}{4}H_2(ze^{\frac{j2\pi(2)}{4}}) \\ \frac{0}{2}H_0(ze^{\frac{j2\pi(3)}{4}}) & \frac{1}{4}H_1(ze^{\frac{j2\pi(3)}{4}}) & \frac{1}{4}H_2(ze^{\frac{j2\pi(3)}{4}}) \end{bmatrix} \times \begin{bmatrix} f_0(z) \\ f_1(z) \\ f_2(z) \end{bmatrix} = \begin{bmatrix} 1 \\ 0 \\ 0 \\ 0 \end{bmatrix} \tag{3.11}$$

Note that: $W_M^l,(e^{\frac{j2\pi(1)}{4}}, e^{\frac{j2\pi(3)}{4}})$ does not show in case of $H_0(ze^{\frac{j2\pi(1)}{2}})$; therefore, the the operator α is set to zero, so pairing-up of aliasing ensures that there is no high-aliasing distortion [35][68].

3.4.2 Illustrative Example of NUFBs of DDFBs method

In order to illustrate the performance of NUFBs with DDFB method [35], the following example implements a NUFB with decimation factors [2 4 4] using Matlab simulation code of the DDFBs method [58]. The length of the analysis and synthesis filters is equal to 64. Frequency response of the analysis filters, total amplitude distortion, and aliasing distortion of the NUFB are presented in Figures 3.11 and 3.13. The results show that the frequency response of the filters has some ripple in pass band; however, the total response of the filter bank is ripple-free. In addition, the amplitude distortion and aliasing distortion are around -40 dB, and they can be improved if the length of the filters is increased.

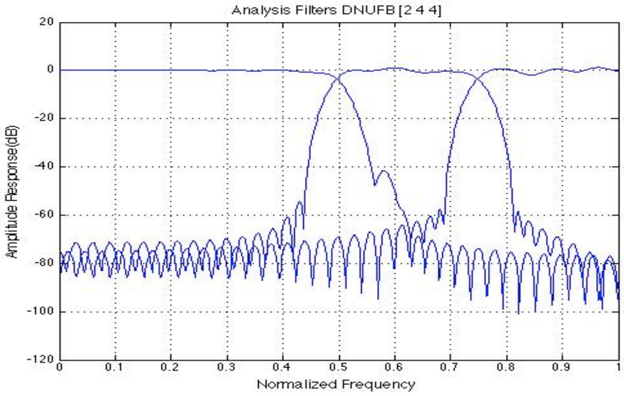

Figure 3.11: Frequency response of NUFBs with decimation factors [2 4 4] designed by DDFBs method

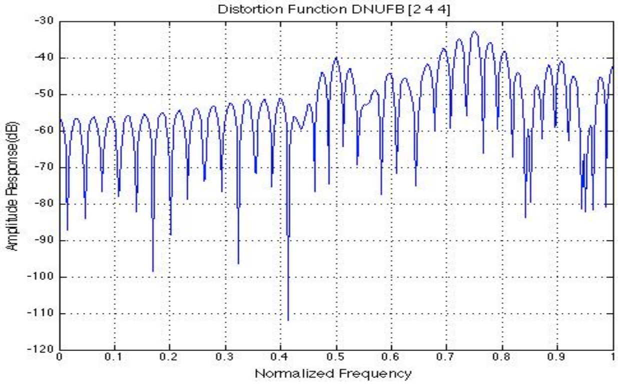

Figure 3.12: Amplitude distortion of NUFBs with decimation factors [2 4 4] designed by DDFBs method

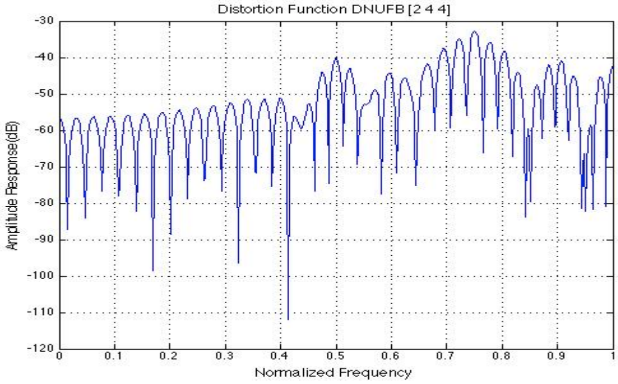

Figure 3.13: Aliasing distortion of NUFBs with decimation factors [2 4 4] designed by DDFBs method

3.5 Summary

The design of NUFBs is not as easy as the design of the UFBs because several limitations and constraints on the decimation factors are involved in order to achieve near-PR or PR NUFBs. However, in literature, several theories and design methods have been proposed to achieve near-PR or PR systems. In addition, during the development of UNFBs, several necessary and sufficient conditions have been developed to satisfy near-PR or PR systems. Therefore, various design methods have involved these conditions in their design formulation, and have shown success in designing near-PR or PR NUFBs.

The QM-CM NUFB [36] design method is a simple indirect-design method. The NUFBs in this method totally depend on designing equivalent UFBs, and merging adjacent filters to obtain the desirable non-uniform response. The method can implement NUFBs with feasible sets; NUFBs with infeasible sets can be obtained with modified structures [36]. Generally, QM-CM NUFBs have minimal aliasing and amplitude distortion; furthermore, the phase response is not affected at all.

On the other hand, the DDFBs method is robust and flexible because it can design various filter banks, such as maximally-decimated and over-sampled UFBs, as well as NUFBs with compatible and incompatible sampling sets. Even though the aliasing and amplitude distortion seem to be high in the example presented, the distortions will reduce if the filter length is increased.

Chapter 4

3D Spatio-Temporal (ST) Uniform Cone and Frustum Filters

4.1 Introduction

Three-dimensional (3D) spatio-temporal (ST) cone filters have been utilized in 3D filtering applications in many areas such as wireless communications, digital video processing, biomedical imaging, and radio astronomy [10][15][17][88][89][90][91][92][93]. In these applications, the objectives are to pass or enhance a desired signal, and to reject or attenuate an undesirable signal. In radio astronomy applications [5][16][26][32], 3D cone and frustum filters are implemented to enhance plane wave (PW) BB signals of interest (SOI) and attenuate radio frequency interference (RFI) and noise according to their direction of arrival.

A variety of methods have been proposed to design 3D cone and frustum filters. In [88][89], two similar methods are proposed to design a 3D recursive cone filters. Both methods in [88][89] have approached the desired 3D cone filters by multiplying two 2D velocity fan filters. Computationally efficient methods that employ optimization and symmetries to design 3D cone filters have been proposed in [90][91]. In [17], 3D cone filters are obtained by coefficients transformation of 2D circularly symmetric filters. A general design method has been introduced in [92] to design various 3D FIR and IIR filters with various band pass shapes. In this method, the design of a 3D filter is transformed to design several 1D filters; the frequency response of each designed 1D filter is optimized. In [10][18][19][26][27][32][33][93], a class of 3D ST cone filters based on filter banks has been emerging. Some of these 3D cone filters are designed based on filter bank structure [19], and others are designed by cascading a 1D filter bank with 2D spatial filters. Two 3D IIR cone filters have been proposed in [93] for selective filtering of 3D ST BB signals and for video applications. The proposed 3D cone filters are designed based on under-decimated DFT filter bank. Similarly, a 3D cone filter is proposed in [26] for radio astronomy applications with objectives to enhance SOI and attenuate radio RFI and noise. The designed cone filter in [26] is achieved by utilizing an under-decimated DFT filter bank as in [93]; however, the difference between the 3D cone filters in [26][93] is that the latter is a 3D FIR cone filter. Recently, in [32][33], 3D ST DFT poly-phase FIR cone and frustum filters are proposed with objective of reducing the computational complexity of the under-decimated DFT cone filter [26]. The structure of the DFT poly-phase cone and frustum filters consists of a maximally decimated DFT filter bank and 2D spatial filters [32][33]. The reduction in computational complexity of poly-phase 3D cone and frustum filters [32][33] is achieved because of the efficient poly-phase implementation of the temporal filter bank. Although the maximally-decimated poly-phase DFT cone filter [32][33] has reduced the computational complexity, the DFT filter bank cannot achieve near perfect reconstructions. Therefore, the author of [32][33] substituted the DFT filter bank with the modified DFT filter bank to achieve an almost perfect reconstruction performance [32].

In this chapter, we further develop two new uniform 3D ST FIR cone filter; moreover, we derive two 3D frustum filters from the two new proposed 3D ST FIR cone filters. Following the filter bank structure in designing 3D ST cone filters [32][33], these two proposed 3D ST cone filters are designed by employing well-known 1D uniform QM-CM filter bank Subsection 2.2.2 [34] and DDFBs Subsection 2.2.3 [35] in the temporal domain. The design details of the new proposed 3D cone filters are presented and their applications in 3D filtering broadband (BB) signals received by DAAs and FPAs are investigated.

This chapter is organized by first providing an overview of modified DFT (MDFT) 3D cone and frustum filters [32][33] in Section 4.2. In the Section 4.4 and 4.5, the two proposed uniform 3D QM-CM and DDFBs cone filters and the derived 3D frustum filters are discussed in detail. The performance of MDFT, QM-CM, and DDFBs 3D cone filters in terms of magnitude response and aliasing distortion is illustrated and compared in Section 4.5. 3D filtering of BB signals received by DAAs and FPAs and the SINRs evaluation for various 3D cone and frustum filter is investigated and presented in Section 4.6. In Section 4.7, the computational complexity of the MDFT and the new proposed 3D cone filters are compared. Finally, summary of the analysis among MDFT, QM-CM and DDFBs cone and frustum filters is presented in the concluding Section 4.8.

4.2 A Review of the 3D ST Modified DFT (MDFT) Cone Filter

The 3D ST MDFT cone filter is designed by employing a uniform M-band maximally-decimated MDFT filter bank Subsection 2.2.1 [37] in the temporal domain with 2D spatial circularly symmetric low pass filters [5]. The structure of the M-band 3D MDFT cone filters is illustrated in Figure 4.1 [32][33]. The structure of the 3D MDFT cone filter consists of a MDFT filter bank and additional 2D spatial filters that are placed after the analysis bank. Note that each complex band of the 3D MDFT cone filter consists of a real part and an imaginary part; therefore, the same 2D spatial filters are placed with the real and imaginary parts in each band. The decimation and interpolation are only implemented in the temporal direction; therefore, $\mathbf{M_1}$ and $\mathbf{M_2}$ are diagonal matrices given by Eq. (4.1)-(4.2) [32][33].

$$\mathbf{M}_1 = diag[1 \quad 1 \quad M/2] \tag{4.1}$$

$$\mathbf{M}_2 = diag[1 \quad 1 \quad 2] \tag{4.2}$$

As mentioned in Subsection 2.2.1, the MDFT filter bank is complex modulated and does not possess the symmetric properties; therefore, the frequency response of each filter of the MDFT filter bank occupies a single spectrum except for the first low pass filter, which has symmetric response [37]. Consequently, each band of the 3D MDFT cone filter Figure 4.1 constructs a single non-symmetric disc with a height of $2\pi/M$ and proper radius that depends on the number of bands to approximate the shape of double-cone as shown in Figure 4.2 [32][33]. Note that only the low pass filter $H_0(z_{ct})$ possesses the symmetric around the ω_{ct} axis, as shown in Figure 4.2 [32][33].

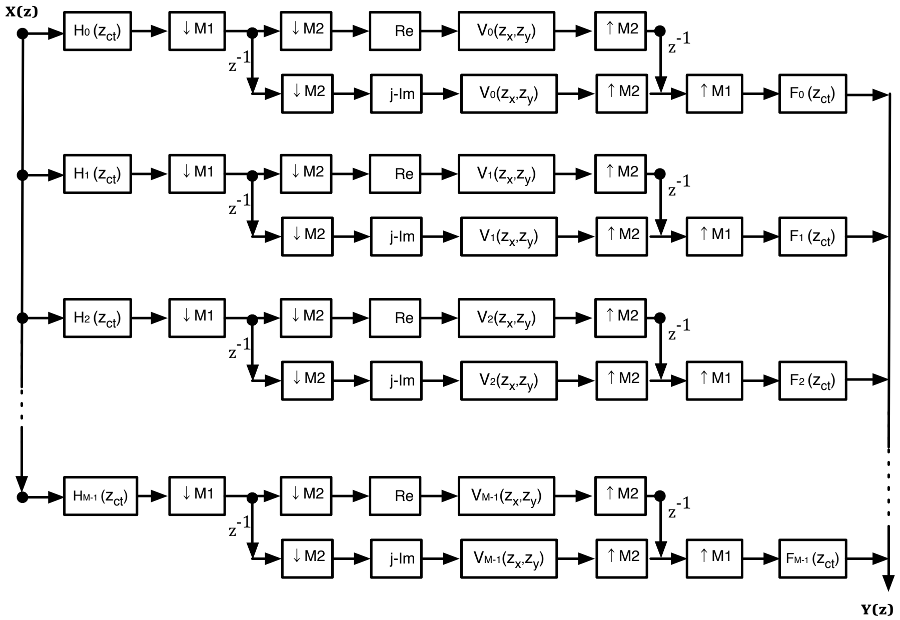

Figure 4.1: The 3D MDFT cone filter structure, which consists of 1D MDFT filter bank and 2D M spatial filters [32][33]

4.2.1 2D Spatial Circularly symmetric Low Pass Filters Design

The ideal frequency response of the 2D spatial circularly symmetric low pass filters is given by Eq. (4.3) [5].

$$V_k(e^{j\omega_x}, e^{j\omega_y}) = \begin{cases} 1, & \sqrt{\omega_x^2 + \omega_y^2} \leq \omega_{sc,k} \\ 0, & \text{otherwise} \end{cases} \tag{4.3}$$

$$\omega_{sc,k} = \begin{cases} \dfrac{\pi}{M} \tan\varepsilon, & k = 0 \\ \dfrac{2k\pi}{M} \tan\varepsilon, & k = 1, \cdots, M/2 \\ \dfrac{2(M-k)\pi}{M} \tan\varepsilon, & k = (M/2+2), \cdots, (M-1) \end{cases} \tag{4.4}$$

ε is the half-cone angle

It is observed that the cutoff frequencies $\omega_{sc,k}$ for $k = 1, ..., (M/2-1)$, is equal to $k = (M/2+1), ..., (M-1)$, as in Eq. (4.5) [32][33],

$$\omega_{sc,k} = \omega_{sc,M-k} \tag{4.5}$$

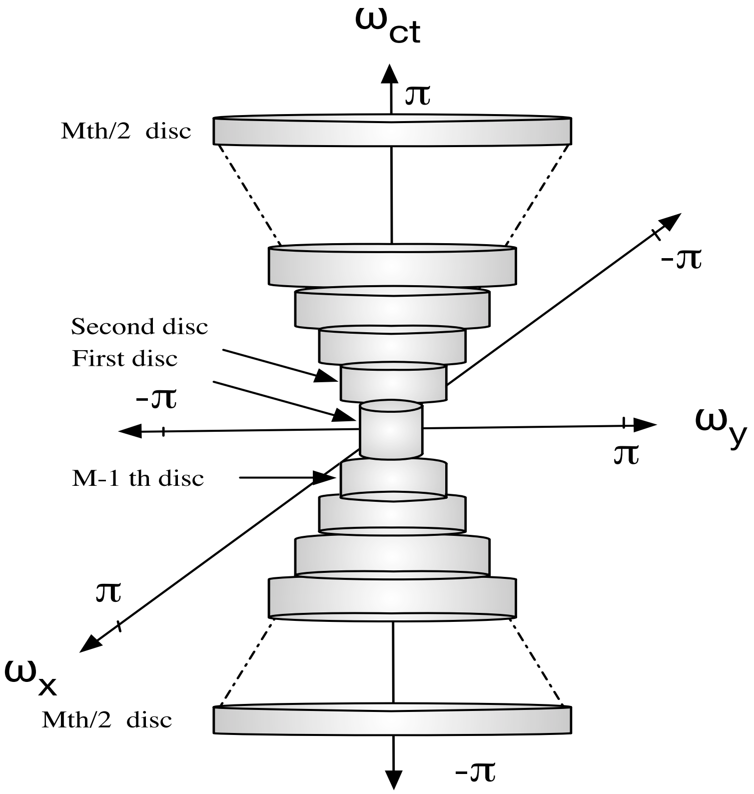

Figure 4.2: Double cone shape of 3D MDFT cone filter, only the first disc is symmetric around the temporal domain [32]

This implies that the 2D spatial filters with index (k and $M - k$) are equal; therefore, during designing of the 3D MDFT cone filter, only ($M/2 + 1$) 2D spatial filters are designed. This results in reducing the design cost of 2D spatial filters to almost half [32][33]. In the time domain, the 2D spatial infinite impulse response $v_{I,k}(n_x, n_x)$ is expressed as in Eq. (4.6) [32][33][5],

$$v_{I,k}(n_x, n_y) = \frac{\omega_{sc,k}}{2\pi\sqrt{n_x^2 + n_y^2}} J(\omega_{sc,k}\sqrt{n_x^2 + n_y^2}) \tag{4.6}$$

where $J(.)$ is the 1st order Bassel function. In order to design a 2D finite extend impulse response $v_k(n_x, n_x)$ of $v_{I,k}(n_x, n_y)$, various windowing techniques can be used [5]. In [32][33], the 2D infinite impulse response $v_{I,k}(n_x, n_y)$ is multiplied with 2D Hamming window with finite length (N_x, N_y) to obtained $v_k(n_x, n_x)$ with finite length of (N_x, N_y) Eq. (4.7).

$$v_k(n_x, n_y) = v_{I,k}(n_x, n_y) w_{2DHam}(n_x, n_y) \tag{4.7}$$

Note that, the 2D Hamming window $w_{2DHam}(n_x, n_y)$ is extended from the 1D Hamming window [5].

4.2.2 Poly-phase Implementation of the 3D MDFT Cone Filter

The 3D MDFT cone filter can be efficiently implemented by realizing the MDFT filter bank with two-1D DFT poly-phase filter bank [32][33], as discussed in Subsection 2.2.1. Figure 4.3 presents the efficient poly-phase implementation of the 3D MDFT cone filter [32][33]. Note that $G_k(z)$ are the type-1 poly-phase representations of the first analysis filter and $R_k(z)$ are type-3 poly-phase representations of the first synthesis filter [32][33]. The filtering of the analysis, synthesis filters, and spatial filters is proceeded at lower rates because down-sampling and up-sampling matrix $\mathbf{M}$, which is given by (4.8), are moved before the analysis and after the synthesis filters.

$$\mathbf{M} = diag[1 \quad 1 \quad M] \tag{4.8}$$

where M is the number of bands

4.2.3 Input and Output Relationship of the 3D ST MDFT Cone Filter

The input and output equation $Y(z_x, z_y, z_{ct})$ of the 3D MDFT cone filter are expressed in z-domain as Eq. (4.9) [32][33].

$$Y(z_x, z_y, z_{ct}) = \frac{z_{ct}^{-(M/2)}}{M} \sum_{k=0}^{M-1} \sum_{l=0}^{M/2-1} H_k(z_{ct} W_M^{2l}) V_k(z_x, z_y) F_k(z_{ct}) X(z_x, z_y, z_{ct} W_M^{2l}) \tag{4.9}$$

$$D(z_x, z_y, z_{ct}) = z_{ct}^{-(M/2)} \sum_{k=0}^{M-1} H_k(z_{ct}) V_k(z_x, z_y) F_k(z_{ct}) \tag{4.10}$$

$$A(z_x, z_y, z_{ct}) = \frac{1}{M} \sum_{k=0}^{M-1} \sum_{l=0}^{M/2-1} H_k(z_{ct} W_M^{2l}) V_k(z_x, z_y) F_k(z_{ct}) \tag{4.11}$$

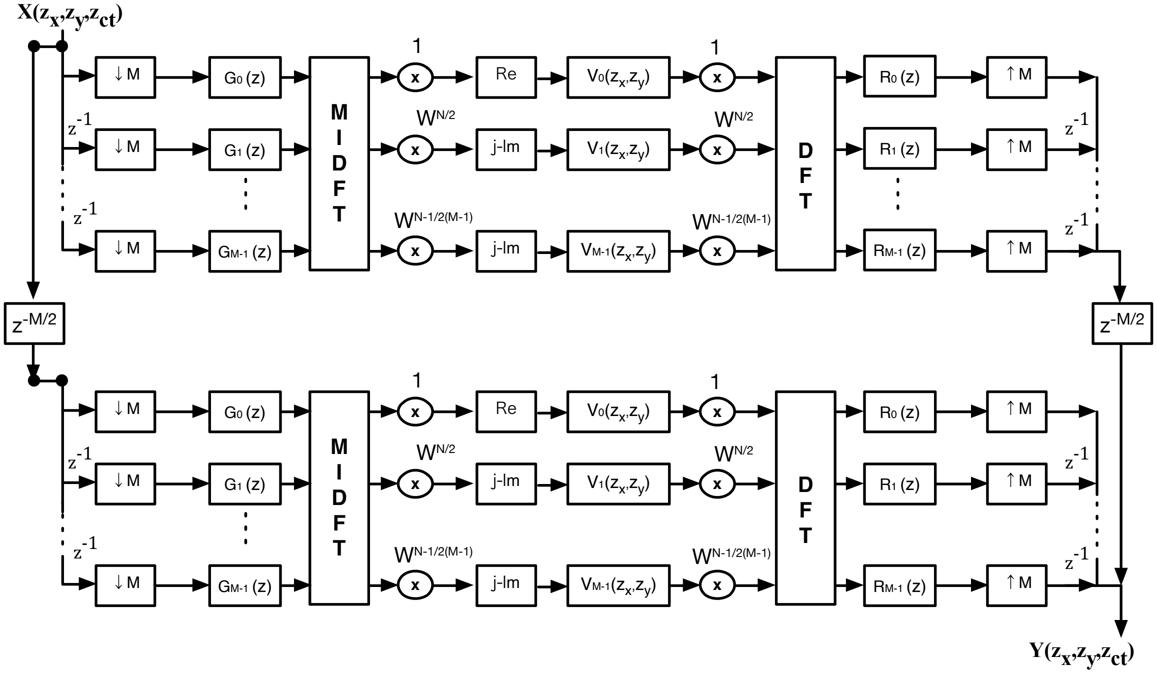

Figure 4.3: Efficient poly-phase realization of the 3D MDFT cone filter [32][33]

Both the distortion function $D(z_x, z_y, z_{ct})$ and aliasing function $A(z_x, z_y, z_{ct})$ can be expressed as in Eq. (4.10)-(4.11), respectively. The 3D MDFT cone filter is an almost aliasing-free system because it has a small aliasing distortion and minimum magnitude distortion. The analysis of aliasing distortion and magnitude response will be discussed and verified with an example.

4.2.4 The Design of 3D MDFT Frustum Filter

A double-frustum shape band pass is illustrated in Figure 4.4. From the figure, one can notice that the double-frustum shape is a portion of a double-cone. Therefore, in [32][33], the author derives the 3D MDFT frustum filter from the original proposed 3D MDFT cone filter by simply implementing a required set $\mathcal{F}$ of discs that can approximate the desirable 3D double-shape frustum filters. During the implementation of the 3D ST frustum filter, a partial MDFT filter bank with a set $\mathcal{F}$ of filters is implemented in the temporal domain; furthermore, only the corresponding 2D spatial filters are implemented to approximate the required 3D frustum filter. For example, if the required 3D frustum filter has a temporal band pass $[0.25 - 0.75]\pi$ and the MDFT filter bank has 16 bands, then only 3^{ed} to 6^{th} analysis, synthesis, and

2D spatial filters are implemented to approximate the upper frustum band pass and 10^{th} to 13^{th} analysis, synthesis, and 2D spatial filters are implemented to achieve the lower frustum. In [32][33], a special algorithm is developed to choose the required set of filters $\mathcal{F}\, that\, \mathcal{F} \in k$, k is $0, 1, ..., M-1$ filters to implement a desirable 3D frustum filter.

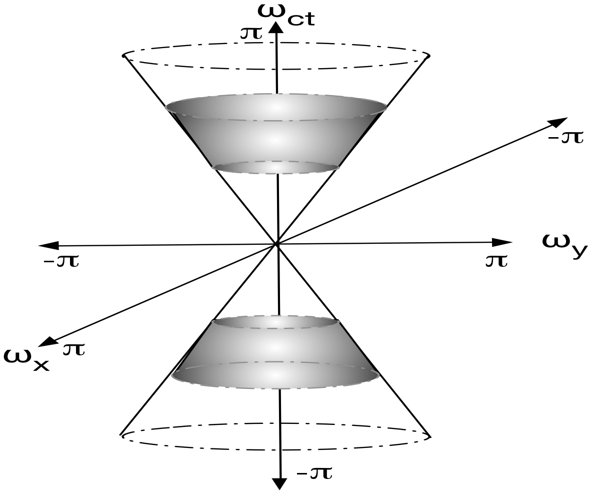

Figure 4.4: 3D double frustum band pass filter shape

Note that in order to efficiently implement the required 3D MDFT frustum filter with poly-phase as in Figure 4.3, all M analysis and synthesis filters are efficiently implemented and the required 2D spatial fillers are implemented. However, the non-required 2D spatial filters are disregarded by substituting their actual values with zeros [32][33].

The input and output relation $Y_{frus}(z_x, z_y, z_{ct})$ Eq. (4.12) of the 3D MDFT frustum filter can be derived from the input and output relation of 3D MDFT cone filter Eq. (4.9) [32][33]. Moreover, the distortion function $D_{frus}(z_x, z_y, z_{ct})$ Eq. (4.13) and aliasing function $A_{frus}(z_x, z_y, z_{ct})$ Eq. (4.14) are derived from Eq. (4.9)[32][33].

$$Y_{frus}(z_x, z_y, z_{ct}) = \frac{z_{ct}^{-(M/2)}}{M} \sum_{k \in F} \sum_{l=0}^{M/2-1} H_k(z_{ct} W_M^{2l}) V_k(z_x, z_y) F_k(z_{ct}) X(z_x, z_y, z_{ct} W_M^{2l}) \tag{4.12}$$

$$D_{frus}(z_x, z_y, z_{ct}) = z_{ct}^{-(M/2)} \sum_{k \in F} H_k(z_{ct}) V_k(z_x, z_y) F_k(z_{ct}) \tag{4.13}$$

$$A_{frus}(z_x, z_y, z_{ct}) = \frac{1}{M} \sum_{k \in F} \sum_{l=0}^{M/2-1} H_k(z_{ct} W_M^{2l}) V_k(z_x, z_y) F_k(z_{ct}) \tag{4.14}$$

4.3 Proposed 3D ST Uniform QM-CM Cone Filter

In this section, a detail discussion of the first proposed uniform 3D ST cone filter is presented. The proposed ST 3D cone filter is based on filter bank structure, specifically, uniform QM-CM filter bank Subsection 2.2.2 [34]. Therefore, we refer to this 3D cone filter as the 3D ST QM-CM cone filter. The structure of the proposed 3D ST QM-CM cone filter in Figure 4.5 consists of M real uniform bands, where M is the number of band (can be an even or odd number). Each band of the 3D QM-CM cone filter Figure 4.5 consists of an analysis filter $H_k(z_{ct})$, a down-sampler given by a diagonal matrix $\mathbf{M}$ Eq. (4.15), a 2D circularly symmetric low pass filter $V_k(z_x, z_y)$, an up-sampler given by the same diagonal matrix $\mathbf{M}$ as in Eq. (4.15), and a synthesis filter $F_k(z_{ct})$. The decimation and interpolation are performed in the temporal domain ω_{ct} and the filter bank is maximally decimated.

$$\mathbf{M} = diag[1 \quad 1 \quad M] \tag{4.15}$$

In contrast to 3D MDFT cone filter, the proposed 3D QM-CM cone filter have real analysis $H_k(z_{ct})$ and synthesis $F_k(z_{ct})$ filters; consequently, the frequency responses of analysis and synthesis filters posses symmetric response around the temporal axis ω_{ct}. Each band of the 3D QM-CM cone filter constructs a symmetric-disc around the temporal axis ω_{ct}, as shown in Figure 4.6. Each single disc has height of π/M, which depends on the number of band, M, and proper radius that increases as the band number increases.

The design of a M-band 3D QM-CM cone filter is equivalent to design a prototype filter, real cosine modulation of the prototype filter, and designing M 2D low pass spatial filters. For detail discussion of the QM-CM filter bank, its prototype filter(s), analysis and synthesis filters, modulation and performance analysis of QM-CM filter bank, see Subsection 2.2.2 and [34].

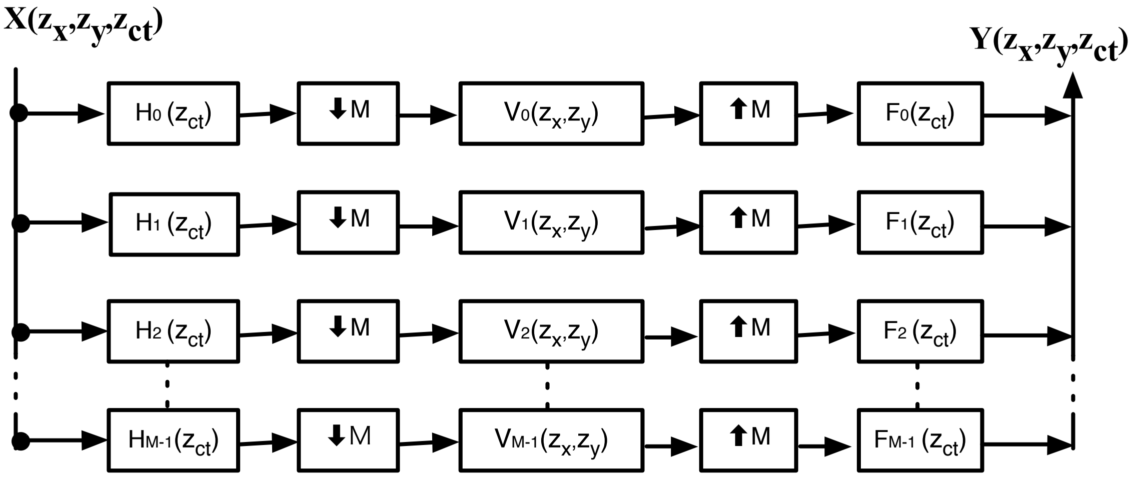

Figure 4.5: Proposed 3D QM-CM cone filter structure that is based on 1D uniform maximally decimated QM-CM Sec (2.4) [34] in temporal domain and 2D circularly symmetric low pass filters.

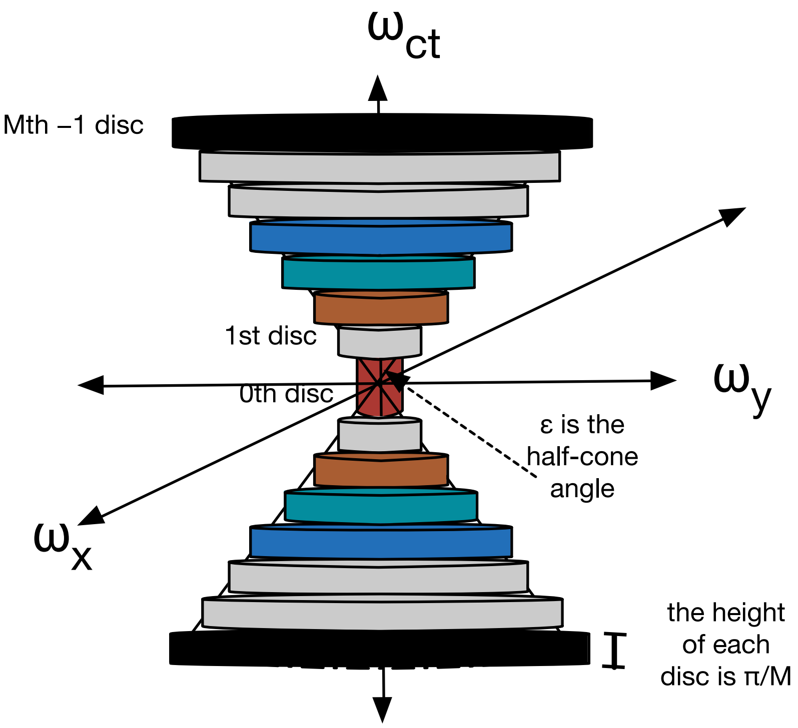

Figure 4.6: The ideal double-cone shape of 3D QM-CM cone filter

4.3.1 2D Spatial Circularly Symmetric Low Pass Filters Design

The ideal frequency response of the 2D spatial circularly symmetric low pass filters is given by Eq. (4.3) [32][33][5]. The 2D spatial filters for 3D QM-CM cone can be similarly designed as the 2D spatial filter of MDFT cone filter [32][33]. However, for the 3D QM-CM cone filter the cutoff frequency for the 2D spatial filters is given by Eq. (4.16).

$$\omega_{sc,k} = \frac{(k+1)\pi}{M}\tan\varepsilon \qquad (4.16)$$
$$k = 0, 1, \cdots, M-1$$

This implies that for M-band 3D QM-CM cone filter, M 2D spatial filters are designed to approximate the double-cone shape.

4.3.2 Efficient Poly-phase Implementation of 3D QM-CM Cone Filter

Efficient implementations of any maximally decimated filter bank can be realized with two poly-phase matrices is demonstrated in Section B.1 [38]. In addition, a special efficient implementation of QM-CM filter bank using $2M$ poly-phase representations of a prototype filter and a matrix T is illustrated in Section B.2 [38]. Both efficient implementation methods in Sections B.1-B.2 can be utilized to efficiently implement the 3D QM-CM cone filter. Here, the efficient implementation of 3D QM-CM cone filter using $2M$ poly-phase representations of the prototype filter and matrix T is utilized in Figure (4.7). In this representation, the computation complexity is reduced because the filtering is performed at lower rates and the analysis and synthesis filters are represented as the $2M$ poly-phase of the prototype filter [38]. Note that $G_k(-z^2)$ for $k = 0, \cdots, 2M-1$ are the $2M$ poly-phase of a prototype filter with any length $N = mM$, where m is an integer, and T matrix given by Eq. (B.6) is a real matrix that consist of the cosine modulation components. Therefore, the analysis filter are given by $H_k(z) = Tg(z)$ and the synthesis filter are given by $f_k^T(z) = z^{-N}\ H^T$ $z^{-1} = z^{-N}g^T z^{-1}T^T$, where g(z) is given by (B.9) as,

$$g(z) = \begin{vmatrix} G_0(-z^{2M}) \\ z^{-1}G_1(-z^{2M}) \\ \vdots \\ z^{2M-1}G_{2M-1}(-z^{2M}) \end{vmatrix}$$

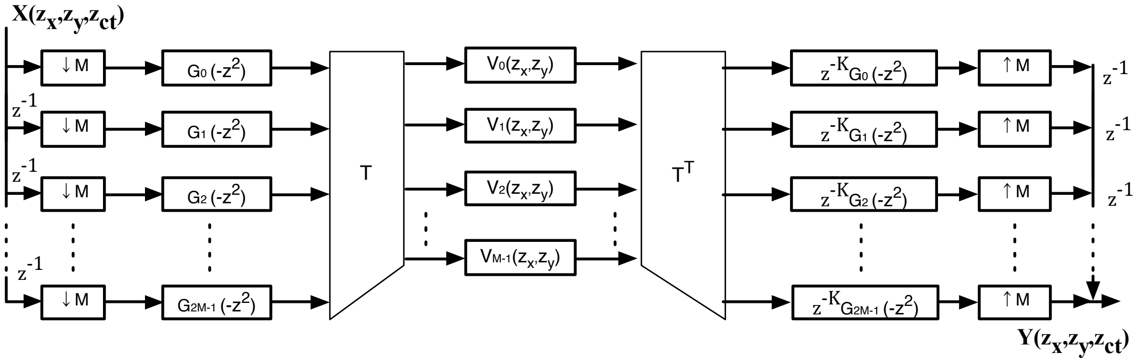

Figure 4.7: Efficient implementation of 3D QM-CM cone filter using $2M$ poly-phase and matrix T.

4.3.3 Input and Output Relationship of the 3D QM-CM Cone Filter

The QM-CM filter bank input and output are related in Eq. (2.11); the desired transfer function $D(z)$ and aliasing distortion $A(z)$ are expressed in Eq. (2.12)-(2.13) Subsection 2.2.2 [34]. Realizing the QM-CM filter bank input and output Eq. (2.11) and the structure of the 3D QM-CM cone filter Figure 4.5, the 3D output signal of 3D QM-CM cone filter $Y_{QM-CM}(z_x, z_y, z_{ct})$ can be expressed as in Eq. (4.17). In addition, aliasing distortion function $A_{QM-CM}(z_x, z_y, z_{ct})$ and the desired magnitude function $D_{QM-CM}(z_x, z_y, z_{ct})$ are derived as in Eq. (4.18)-(4.19), respectively.

$$Y_{QM-CM}(z_x, z_y, z_{ct}) = \frac{1}{M}\sum_{k=0}^{M-1}\sum_{l=0}^{M-1} H_k(z_{ct}W_M^l)V_k(z_x, z_y)F_k(z_{ct})X(z_x, z_y, z_{ct}W_M^l) \tag{4.17}$$

$$A_{QM-CM}(z_x, z_y, z_{ct}) = \frac{1}{M}\sum_{k=0}^{M-1}\sum_{l=0}^{M-1} H_k(z_{ct}W_M^l)V_k(z_x, z_y)F_k(z_{ct}) \tag{4.18}$$

$$D_{QM-CM}(z_x, z_y, z_{ct}) = \frac{1}{M}\sum_{k=0}^{M-1} H_k(z_{ct})V_k(z_x, z_y)F_k(z_{ct}) \tag{4.19}$$

Note that the aliasing function $A_{QM-CM}(z_x, z_y, z_{ct})$ consists of $M-1$ aliasing terms; moreover, the desired component $D_{QM-CM}(z_x, z_y, z_{ct})$ is almost free from distortion so it is equivalent to a delay.

4.3.4 The Design of 3D QM-CM Frustum Filter

The idea of designing a 3D double frustum from a 3D cone filters is simple because it is involves approximating a 3D cone filter with discs and then implementing the required discs to achieve the desirable 3D frustum filter. In Subsection 4.2.4, the 3D MDFT frustum filter has been obtained by implementing set $\mathcal{F}$ of sub-band $\mathcal{F}\in$k, $k = 0, ..., M - 1$ indexes of filters.

Similarly, any desirable 3D QM-CM frustum filter can be implemented. As mentioned in the previous section, each band of the 3D QM-CM cone filter constructs a symmetric-disc, each individual disc with a height of π/M and a proper radius. Any 3D QM-CM frustum filter can be obtained from a corresponding 3D QM-CM cone filter by implementing the required set, disc, or band $\mathbb{F}$, $\mathbb{F}\in k$, (k contains all bands of 3D cone filter, $k = 0, ..., M - 1$) and disregarding the rest of bands. For example, to design a 3D QM-CM frustum filter with bandwidth $[0.25 - 0.75]\pi$ from a corresponding 16-band 3D QM-CM cone filter, the set of sub-band or set of filters that include analysis, 2D spatial and synthesis, $\mathbb{F}$ consists of k= 4,5,...,11 are implemented and the rest sub-band are disregarded. *Note that in order to achieve efficient implementation of the 3D QM-CM frustum filter, the entire M-band QM-CM filter bank must be efficiently implemented and the required 2D spatial filter are implemented. However, the non-required 2D spatial filters are disregarded and their actual values are replaced with zeros.*

The 3D output signal $Y_{QM-CM\,frus}(z_x, z_y, z_{ct})$ Eq. (4.20) of the 3D QM-CM frustum filter can be derived from the $Y_{QM-CM}(z_x, z_y, z_{ct})$ Eq. (4.17). The aliasing distortion $A_{QM-CM\,frus}(z_x, z_y, z_{ct})$ and transfer function $D_{QM-CM\,frus}(z_x, z_y, z_{ct})$ can be expressed as in Eq. (4.21)-(4.22).

$$Y_{QM-CM\,frus}(z_x, z_y, z_{ct}) = \frac{1}{M} \sum_{k\in\mathbb{F}} \sum_{l=0}^{M-1} H_k(z_{ct}W_M^l)V_k(z_x, z_y)F_k(z_{ct})X(z_x, z_y, z_{ct}W_M^l) \tag{4.20}$$

$$A_{QM-CM\,frus}(z_x, z_y, z_{ct}) = \frac{1}{M} \sum_{k\in\mathbb{F}} \sum_{l=0}^{M-1} H_k(z_{ct}W_M^l)V_k(z_x, z_y)F_k(z_{ct}) \tag{4.21}$$

$$D_{QM-CM\,frus}(z_x, z_y, z_{ct}) = \frac{1}{M} \sum_{k\in\mathbb{F}} H_k(z_{ct})V_k(z_x, z_y)F_k(z_{ct}) \tag{4.22}$$

4.4 Proposed 3D ST Uniform DDFBs Cone Filter

Similarly to 3D QM-CM cone filter, another 3D cone filter is proposed and its design details are represented. The proposed cone filter is designed in a similar manner to the 3D MDFT and QM-CM cone filters. The proposed cone filter is titled the 3D DDFBs cone filter because its structure consists of 1D uniform Directly Designed Filter Bank (DDFBs) Section 2.4 [35] in temporal domain cascaded with 2D circularly symmetric spatial low pass filters. The structure of 3D DDFBs cone filter is exactly identical to the structure of QM-CM 3D cone filter, as in Figure 4.5. The 3D DDFBs cone filter consists of M real bands where each band contains an analysis filter, down-sampler M that is a diagonal matrix and it is given by Eq. (4.15), a 2D spatial filter, and up-sampler M Eq. (4.15), and a synthesis filter. Note that similar to previous cone filters, the decimation and interpolation are only performed in the temporal dimension and the system is maximally decimated. Each band of the 3D DDFBs cone creates a symmetric disc around the temporal domain ω_{ct} because the DDFBs possesses even symmetric frequency response. Therefore, the M bands can approximate that double-cone shape as in Figure 4.6.

The design of M-band 3D DDFBs cone filter costs designing a 1D uniform M-band DDFBs Section 2.4 [35] and M 2D circularly symmetric low pass spatial filters [5]. The design of 3D DDFBs cone filter can be flexible because the design of its 1D filter bank is very flexible. This flexibility of 1D filter bank enables us to design any number of uniform bands with any length of filters.

4.4.1 2D Spatial Circularly Symmetric Low Pass Filters Design

The designed of M-band 3D DDFBs cone filter requires M-band 1D DDFBs and M 2D spatial circularly symmetric low pass filters. The 2D spatial filters for the 3D DDFBs cone filter are identical to the 2D spatial filter of the 3D QM-CM cone filter. For more detail on the 2D spatial filters, refer to Subsection 4.3.1.

4.4.2 Efficient Poly-phase Implementation of 3D DDFBs Cone Filter

The analysis and synthesis banks of any M-band maximally decimated filter bank can be represented using M poly-phase representation [38]. In Section B.1, the representation of M-band maximally decimated filter bank is demonstrated [38]. The analysis filters are presented as matrix $\mathbf{E}(\mathbf{z^M})$ Eq. (B.1),(B.3) using poly-phase type-1 and synthesis filters are presented as matrix $\mathbf{R}(\mathbf{z^M})$ Eq. (B.2),(B.4) using poly-phase type-3 [38].

These representation can be utilized to implement the 3D DDFBs cone filter where the analysis and synthesis filter will be represented with matrices $\mathbf{E}(\mathbf{z^M})$ and $\mathbf{R}(\mathbf{z^M})$ as in Eq. (B.3)-(B.4) Figure 4.8. Furthermore, with noble identities [38], the down-samplers can be moved before the $\mathbf{E}(\mathbf{z^M})$ matrix and the up-samplers can be moved after the $\mathbf{R}(\mathbf{z^M})$ matrix depicted in Figure 4.9 to achieve computationally efficient implementations . With efficient implementation Figure 4.9, the computational complexity is reduced because the filtering is performed at the lowest rates.

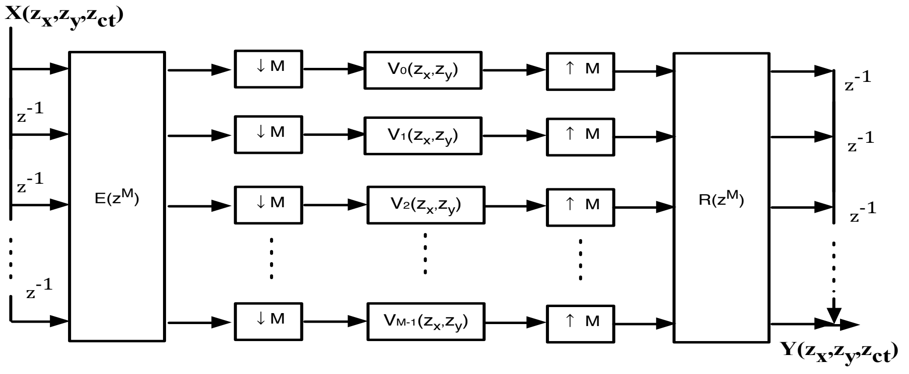

Figure 4.8: Poly-phase representation of 3D DDFBs cone filter where the analysis and synthesis filter are represented with matrices

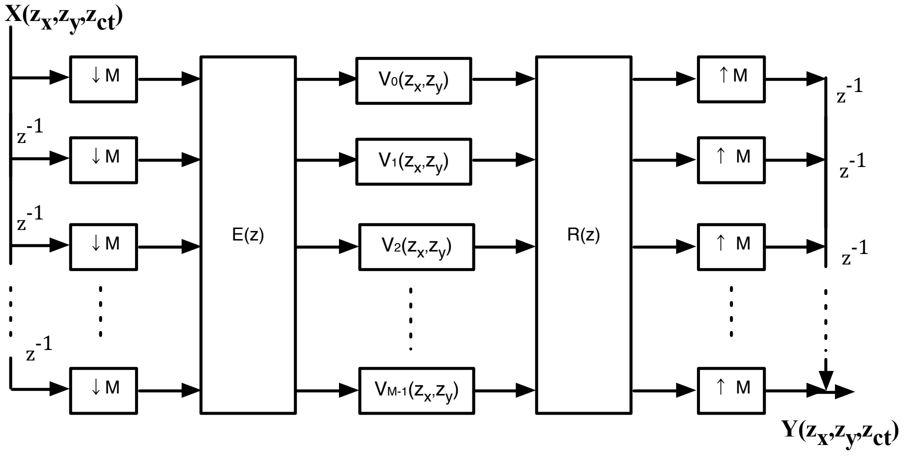

Figure 4.9: Efficient poly-phase implementation of 3D DDFBs cone filter

4.4.3 Input and Output Relationship of the 3D DDFBs Cone Filter

The input and output of equation of DDFBs is discussed in Subsection 2.2.3 and it is expressed in Eq. (2.14) [35]. Since the 3D DDFBs cone filter implementation involves 1D DDFBs in temporal domain, the 3D reconstructed signal $Y_{DDFBs}(z_x, z_y, z_{ct})$ can be obtained by combining the 1D temporal DDFBs with the 2D spatial filters. Therefore, the 3D reconstructed signal $Y_{DDFBs}(z_x, z_y, z_{ct})$ of 3D DDFBs can be expressed as in Eq. (4.23). Moreover, the aliasing distortion function and desired transfer function are derived from Eq. (4.23) as in Eq. (4.24)-(4.25).

$$Y_{DDFBs}(z_x, z_y, z_{ct}) = \sum_{k=0}^{M-1} \sum_{l=0}^{M-1} \frac{\alpha_{k,l}}{n_k} H_k(z_{ct} W_M^l) V_k(z_x, z_y) F_k(z_{ct}) X(z_x, z_y, z_{ct} W_M^l) \tag{4.23}$$

$n_k = M$, the number of band

$$\alpha_{k,l} = 1$$

$$A_{DDFBs}(z_x, z_y, z_{ct}) = \sum_{k=0}^{M-1} \sum_{l=0}^{M-1} \frac{\alpha_{k,l}}{n_k} H_k(z_{ct} W_M^l) V_k(z_x, z_y) F_k(z_{ct}) \tag{4.24}$$

$$D_{DDFBs}(z_x, z_y, z_{ct}) = \sum_{k=0}^{M-1} \frac{1}{n_k} H_k(z_{ct}) V_k(z_x, z_y) F_k(z_{ct}) \tag{4.25}$$

4.4.4 The Design of 3D DDFBs Frustum Filter

The 3D DDFBs frustum filter is designed in the same manner as the 3D QM-CM frustum filter. Any desirable 3D DDFBs frustum filter can be designed from a corresponding 3D DDFBs cone filter by implementing the required set of bands $\mathbb{F}\in$k and disregarding the rest of the bands. The 3D output signal of the 3D DDFBs frustum can be derived from the 3D output signal $Y_{DDFBs}(z_x, z_y, z_{ct})$ of the 3D DDFBs cone filter Eq. (4.23). In the following, the 3D output signal of the frustum filter $Y_{DDFBs\,frus}(z_x, z_y, z_{ct})$, aliasing distortion $A_{DDFBs\,frus}(z_x, z_y, z_{ct})$ and magnitude function $D_{DDFBs\,frus}(z_x, z_y, z_{ct})$ are expressed in (4.26), (4.27), and (4.28), respectively. Note, 3D DDFBs frustum filters can be efficiently implemented by constructing polyphase matrices $\mathbf{E}(\mathbf{z})$ and $\mathbf{R}(\mathbf{z})$ that correspond to the analysis and synthesis filters required for approximating the double-frustum shape and cascade them with the required set $\mathbb{F}$ of 2D spatial filters.

$$Y_{DDFBs\,frus}(z_x, z_y, z_{ct}) = \sum_{k\in\mathbb{F}} \sum_{l=0}^{M-1} \frac{\alpha_{k,l}}{n_k} H_k(z_{ct}W_M^l) V_k(z_x, z_y) F_k(z_{ct}) X(z_x, z_y, z_{ct}W_M^l) \tag{4.26}$$

$$A_{DDFBs\,frus}(z_x, z_y, z_{ct}) = \sum_{k\in\mathbb{F}} \sum_{l=0}^{M-1} \frac{\alpha_{k,l}}{n_k} H_k(z_{ct}W_M^l) V_k(z_x, z_y) F_k(z_{ct}) \tag{4.27}$$

$$D_{DDFBs\,frus}(z_x, z_y, z_{ct}) = \sum_{k\in\mathbb{F}} \frac{1}{n_k} H_k(z_{ct}) V_k(z_x, z_y) F_k(z_{ct}) \tag{4.28}$$

4.5 Performance Analysis of ST 3D MDFT, QM-CM and DDFBs Cone and Frustum Filters

In this section, 3D MDFT with temporal filters' length (N=128 complex cof.), QM-CM, and DDFBs with temporal filters' length (N=256 real cof.) cone and frustum filters are implemented in order to compare their magnitude response, aliasing distortion, and amplitude distortion. The magnitude responses are investigated to determine the accuracy of cone approximations. The aliasing and amplitude distortion illustrate the distortion effects.

The magnitude response and aliasing distortion for 32-band 3D MDFT cone filter, 16-band 3D QM-CM cone filter, 16-band 3D DDFBs cone filter, 32-band 3D QM-CM cone filter, and 32-band 3D DDFBs cone filter are plotted in Figures 4.10-4.14. The magnitude responses of the 32-band 3D MDFT cone filter, the 16-band 3D QM-CM cone filter, the 16-band 3D DDFTs cone filter Figures 4.10-4.12 have similar double-cone approximation because all cone filters are constructed with around 30 to 32 discs. Note that although the number of band of the MDFT cone filter is double the number of band of the QM-CM and DDFBs cone filters, the magnitude responses are similar because the QM-CM and DDFBs filter banks possess even symmetries. The 32-band 3D QM-CM and the 32-band 3D MDFT cone filters achieve very excellent and accurate approximation for the required double-cone shape in Figure 4.13-4.14. The edges of the discs for the 32-band 3D QM-CM and the 32-band 3D MDFT cone filters are very smooth because the normalized height of each disc is equal to $(1/M) = (1/32)$.

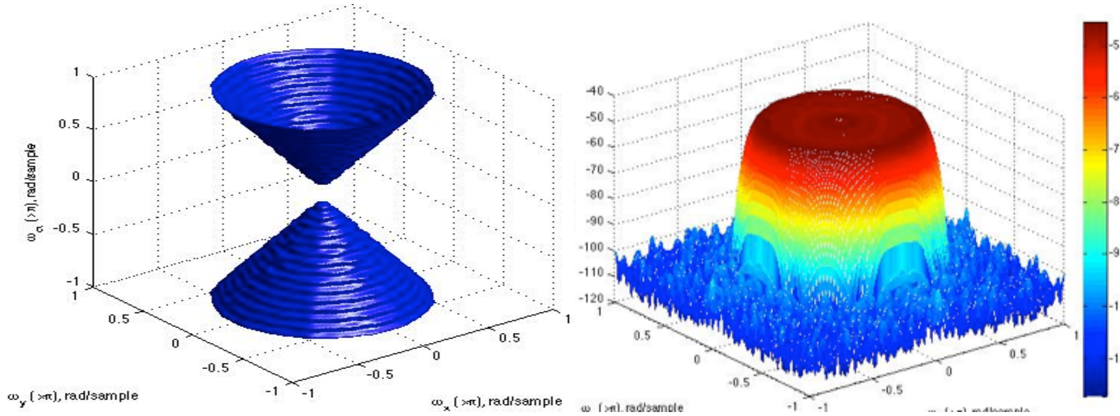

Figure 4.10: The normalized magnitude response of 32-band MDFT cone filter and the maximum aliasing distortion for each spatial frequency for 32-band 3D MDFT cone filter [32]

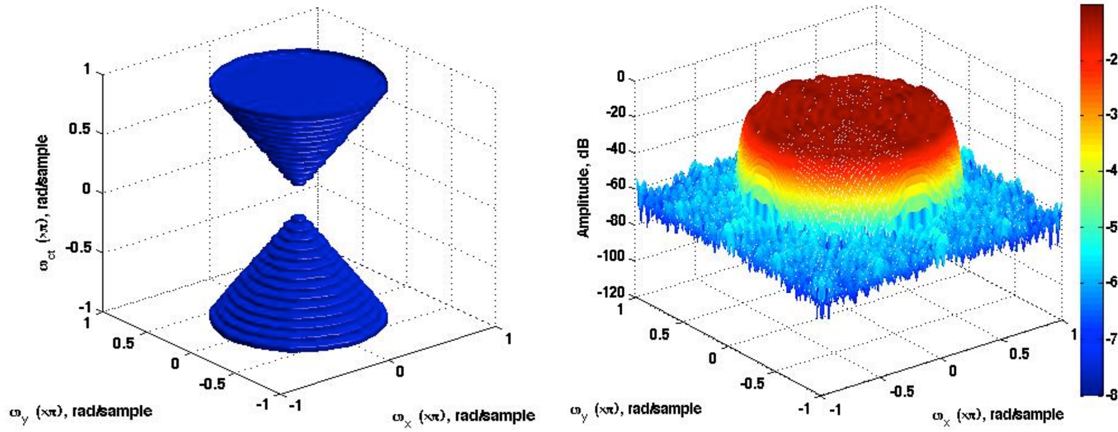

Figure 4.11: The normalized magnitude response of 16-band QM-CM cone filter and the maximum aliasing distortion for each spatial frequency for 16-band QM-CM cone filter

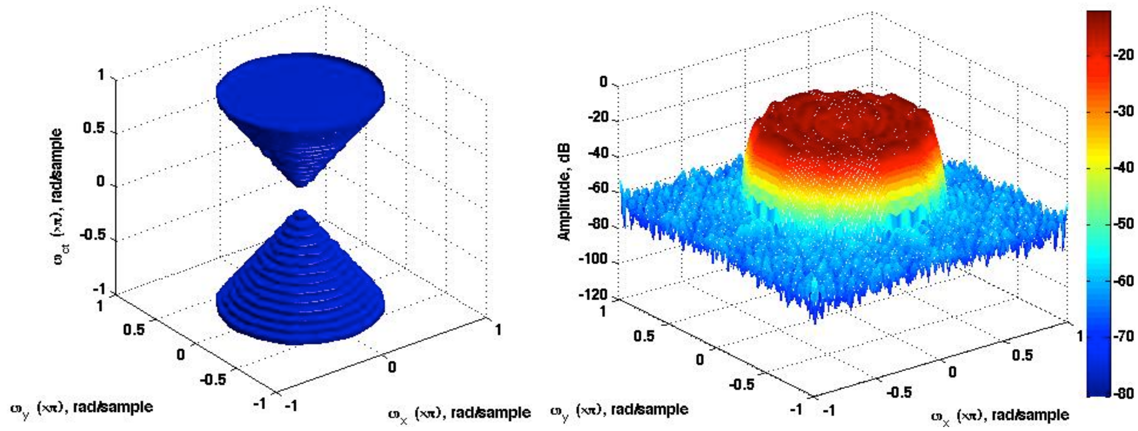

Figure 4.12: The normalized magnitude response of 16-band DDFBs cone filter and the maximum aliasing distortion for each spatial frequency for 16-band DDFBs cone filter

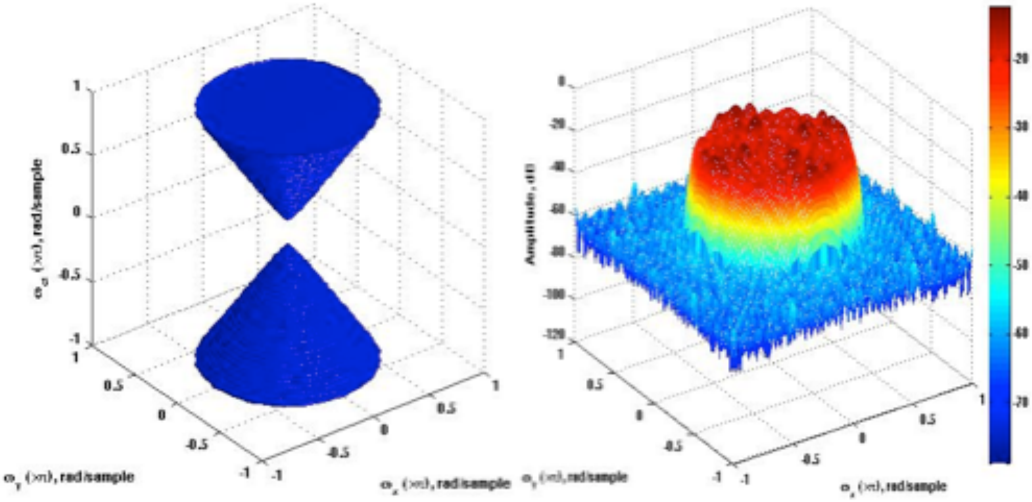

Figure 4.13: The normalized magnitude response of 32-band QM-CM cone filter and the maximum aliasing distortion for each spatial frequency for 32-band QM-CM cone filter

With regard to aliasing distortion, the 32-band MDFT cone filter outperforms all others 3D cone filter with minimal aliasing distortion Figure 4.10. On the other hand, the maximum aliasing distortion for 3D QM-CM and DDFBs cone filters Figures 4.11-4.14 are quite higher than the maximum aliasing distortion of 32-band 3D MDFT cone filter. However, the aliasing distortion for the DDFBs and QM-CM has negligible effect during 3D filtering applications as will be illustrated in Subsection 4.6.1. The amplitude distortion for all of the implemented 3D cone filters is small and equivalent to -50 dB.

For the 3D frustum filters with normalized bandwidth $[0.25 - 0.75]$, Figures 4.15-4.17 present the magnitude response and maximum aliasing distortion of 3D MDFT, QM-CM, and DDFBs frustum filters, respectively. The magnitude response of these 3D frustum filters has similar double frustum shape approximation. Note that the 3D MDFT frustum filter is created with 18 bands out of 32-band 3D MDFT cone filter. On the other hand, only 8-band out 16-band are used to approximate the 3D QM-CM and DDFBs frustum filters. Furthermore, Figures 4.18-4.19 show the amplitude response and aliasing distortion for 3D QM-CM and DDFBs frustum filters that are designed with 16-band out of 32-band cone filters. The magnitude responses of frustum filters Figures 4.18-4.19 have double the accuracy as the magnitude responses of frustum filters in Figures 4.15-4.17. This double accuracy is achieved because the frustum filters are constructed with double the band number.

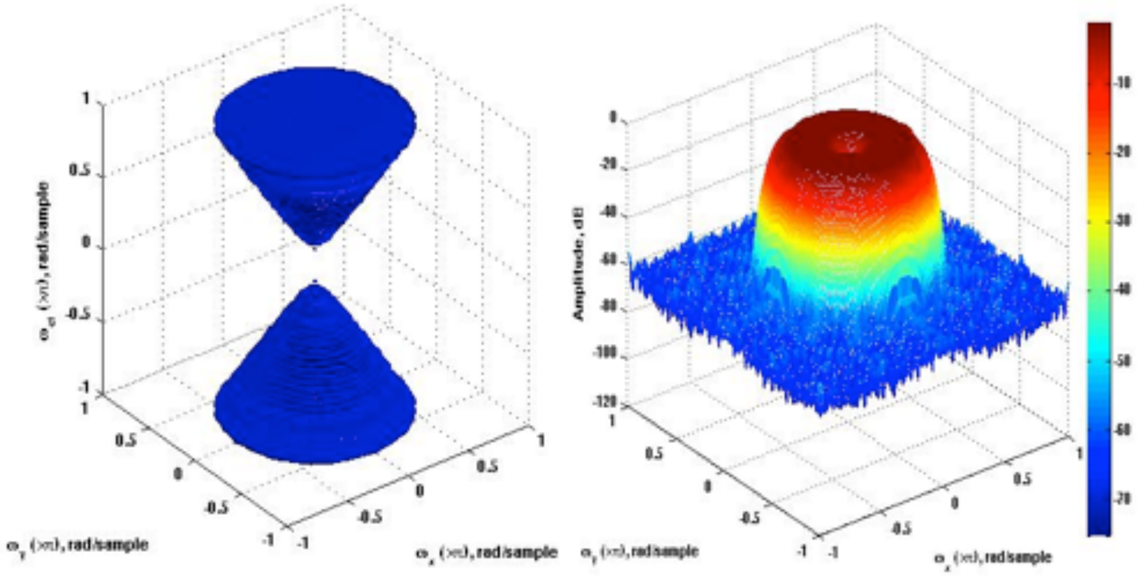

Figure 4.14: The normalized magnitude response of 32-band DDFBs cone filter and the maximum aliasing distortion for each spatial frequency for 32-band DDFBs cone filter

On the other hand, the MDFT frustum has the minimum aliasing distortion among all designed frustum filters. The aliasing distortion for the other 3D QM-CM and DDFBs frustum filters are higher than the 3D MDFT frustum filters; however, it has a minor effect during 3D filtering application, as illustrated in Subsection 4.6.2. Similar to implemented 3D cone filters, the amplitude distortion for all of the implemented 3D frustum filters is small and equivalent to -60 dB. The aliasing effect of the proposed uniform 3D ST QM-CM and DDFBs is analysed in the example provided in Appendix C.

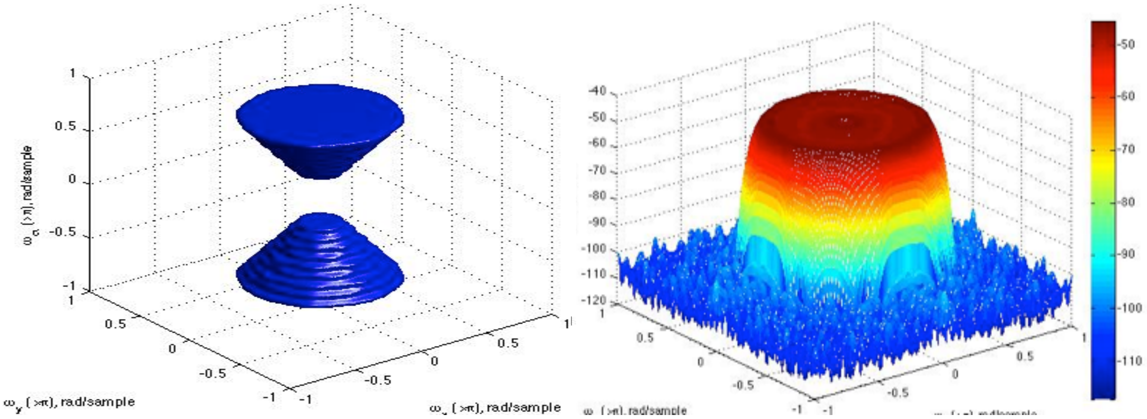

Figure 4.15: The normalized magnitude response of 32-band MDFT frustum filter and the maximum aliasing distortion for each spatial frequency 32-band 3D MDFT frustum filter [32]

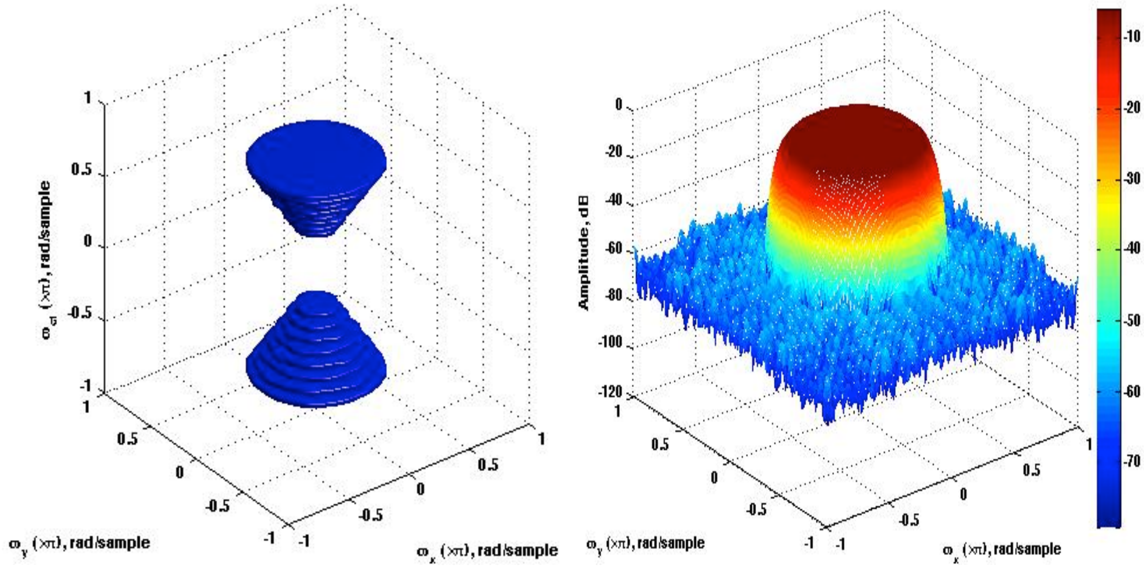

Figure 4.16: The normalized magnitude response of 16-band QM-CM frustum filter and the maximum aliasing distortion for each spatial frequency for 16-band QM-CM frustum filter

4.6 Analysis and Comparison of SINR Obtained with 3D MDFT, QM-CM and DDFBs Cone and Frustum filters with DAAs and FPAs

In the section, a thorough analysis is done to demonstrate and compare the performance and SINR values of the existing 3D MDFT [32], and the proposed 3D CM-CM

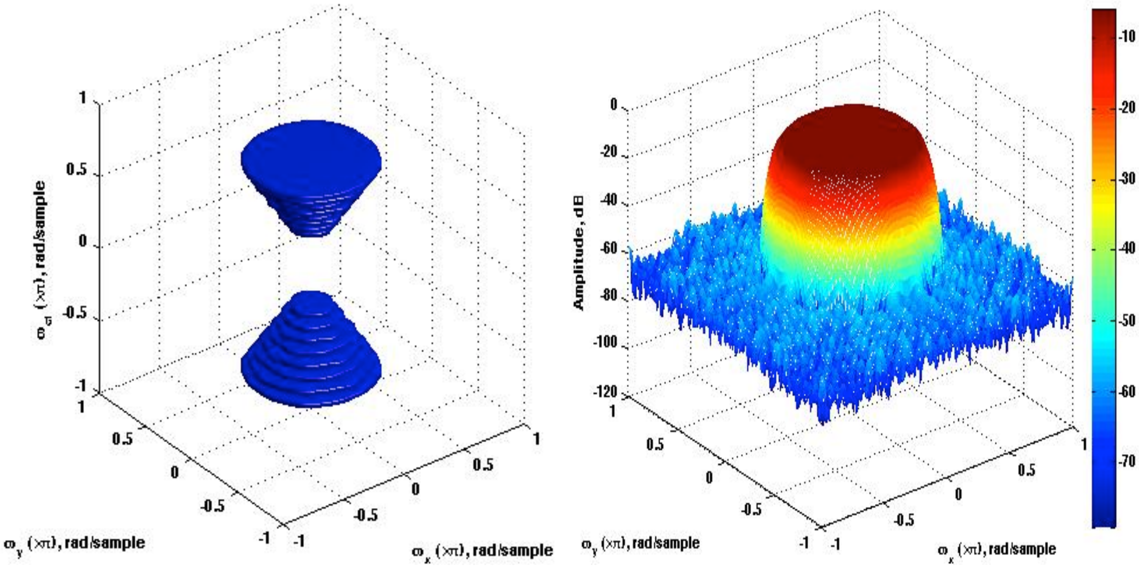

Figure 4.17: The normalized magnitude response of 16-band DDFBs frustum filter and the maximum aliasing distortion for each spatial frequency for 16-band DDFBs frustum filter

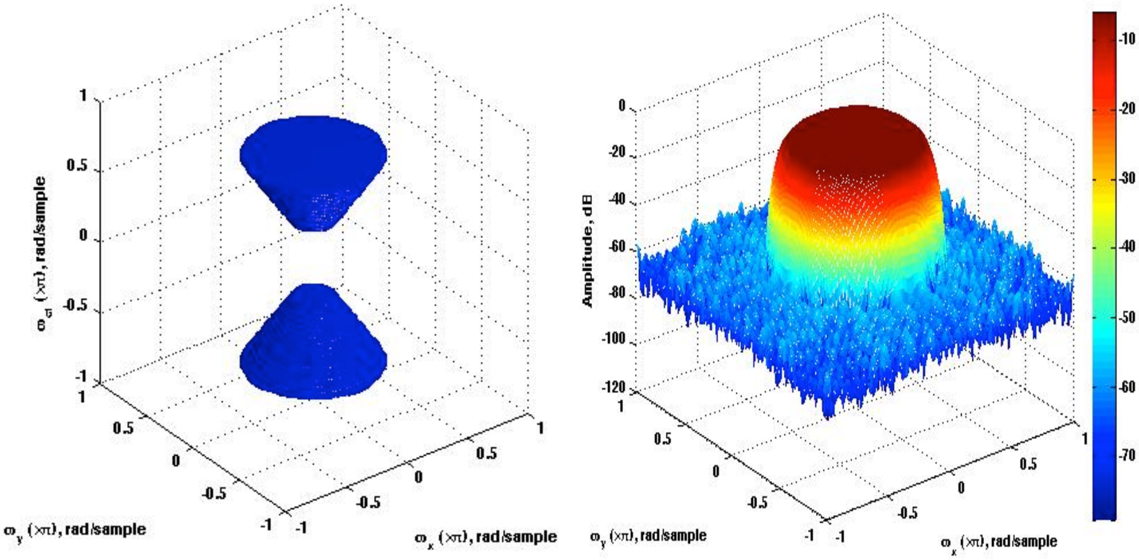

Figure 4.18: The normalized magnitude response of 32-band QM-CM frustum filter and the maximum aliasing distortion for each spatial frequency for 32-band QM-CM frustum filter

and DDFBs cone and frustum filters presented in Section 4.5. In the first subsection, the evaluation of SINR values is obtained with 3D cone filters with DAAs. In the second subsection, the evolution of SINR with FPAs is presented for 3D frustum

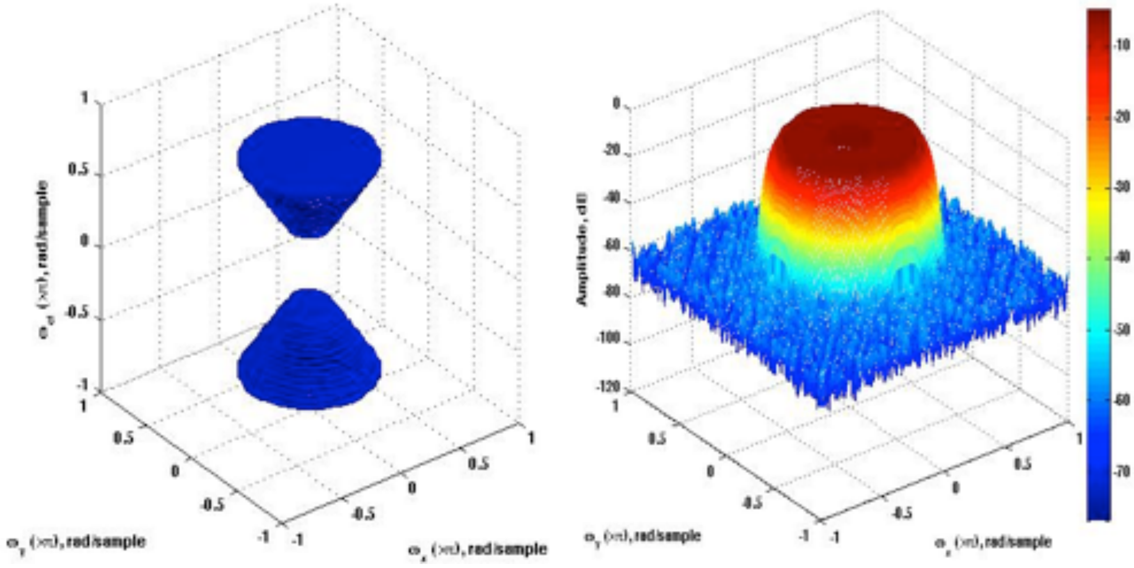

Figure 4.19: The normalized magnitude response of 32-band DDFBs frustum filter and the maximum aliasing distortion for each spatial frequency for 32-band DDFBs frustum filter

filters.

4.6.1 Analysis of SINR values obtained with 3D cone filters with DAAs

In first 3D filtering application, the analysis concerning BB signals received by DAAs that consists of 41 × 41 elemental antennas arranged in a rectangle. The distance between the inner antennas is equal $T_x = T_y = 7.5\,cm$ and f_{ts}, the temporal sampling frequency is equal to 4 GHz. The BB input signal $x_{DAA}(n_x, n_y, n_{ct})$ as in Eq. (4.29) to the cone filters consists $SOI_{DAA}(n_x, n_y, n_{ct})$ signal of interest, $RFI1_{DAA}(n_x, n_y, n_{ct})$ first radio frequency interference signal, $RFI2_{DAA}(n_x, n_y, n_{ct})$ second radio frequency interference signal, and $N_{DAA}(n_x, n_y, n_{ct})$ is Gaussian noise.

$$\begin{aligned} x_{DAA}(n_x, n_y, n_{ct}) &= SOI_{DAA}(n_x, n_y, n_{ct}) + RFI1_{DAA}(n_x, n_y, n_{ct}) \\ &\quad + RFI2_{DAA}(n_x, n_y, n_{ct}) + N_{DAA}(n_x, n_y, n_{ct}) \end{aligned} \tag{4.29}$$

The $SOI_{DAA}(n_x, n_y, n_{ct})$, $RFI1_{DAA}(n_x, n_y, n_{ct})$, and $RFI2_{DAA}(n_x, n_y, n_{ct})$ depicted in Figure 4.20 are numerical synthesized signals that are composed by monochromatic ST PWs Eq. (A.3) [32] with specifications in Table (4.1), see Appendix A for detail. Note that the energy of $RFI1_{DAA}(n_x, n_y, n_{ct})$, and $RFI2_{DAA}(n_x, n_y, n_{ct})$ and $Noise_{DAA}(n_x, n_y, n_{ct})$ are around 20-30 dB higher than the energy of $SOI_{DAA}(n_x, n_y, n_{ct})$; therefore, the $SOI_{DAA}(n_x, n_y, n_{ct})$ is considered to be a weak signal. For a review of the BB signal received with DAAs and its modulation, refer to A.1 and [32].

Signal	(θ, ϕ)	(α, β)	Bandwidth
SOI	$(0°, 0°)$	$(0°, 0°)$	0.0-2.0 GHz
RFI1	$(85°, 40°)$	$(44.89°, 40°)$	0.5-1.2 GHz
RFI2	$(87°, -110°)$	$(44.96°, -110°)$	0.5-1.2 GHz

Table 4.1: Specification of the BB SOI and two terrestrial RFI that received by DAA and using in simulation of 3D cone filters

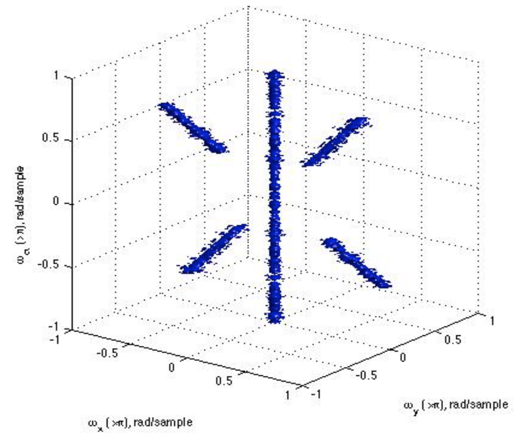

Figure 4.20: ISO-Surface of the normalized magnitude of SOI signal and 2 RFI signals that is received by DAA

During the simulation, a set of 32-band 3D MDFT cone filter, a set of 16-band, and a set of 32-band 3D QM-CM cone filters and a set of 16-band and a set of 32-band DDFBs cone filters with varying half-cone angles as $5°, 7.5°, \cdots, 45°$ are used to evaluate the SINR values. The double-cone shape for all designed filters occupy the whole normalized temporal frequency as plotted in Figures 4.10-4.14 so they have bandwidth of 0-2.0 GHz.

The SINR values for the sets of cone filters with varying angles are plotted in Figure 4.21. The input SINR to each cone filter is constant with values of -31 dB. In general, the output SINR values for all cone filters are decreasing as the half-cone angle increased. The SINR values decrease because as the passband of cone filters gets wider, more energy from noise and RFI signals intrudes into the passband of cone filters. On the other hand, the plot of SINR Figure 4.21 shows that the 16-band QM-CM and the DDFBs cone filters have identical SINR values for all angles. It is clear that the SINR values of the 16-band QM-CM and the DDFBs cone filters outperform the SINR outputs of 32 3D MDFT cone filters. The improvement in the SINR outputs of the 16-band QM-CM and the DDFBs cone filters over the 32-band MDFT cone is effective from angle $5°, 7.5°, \cdots, 45°$ with a value of 1.5-2.0 dB for each angle. Further, the 32-band 3D QM-CM and DDFBs cone filters have almost identical SINR output values that outperform the other SINR values. This improvement can be achieved with additional computational cost. The improvement of the SINR of the 3D 32-band QM-CM and DDFBs is approximately 1 dB better than the SINR of the 3D 16-band QM-CM and DDFBs from angle 7.5° to 30°. Moreover, the SINR outputs of the 3D 32-band QM-CM and DDFBs do not fall down shapely as the other SINR outputs because the 32-band QM-CM and DDFBs approximation of the double cone band pass shape have double accuracy than the other cone filters.

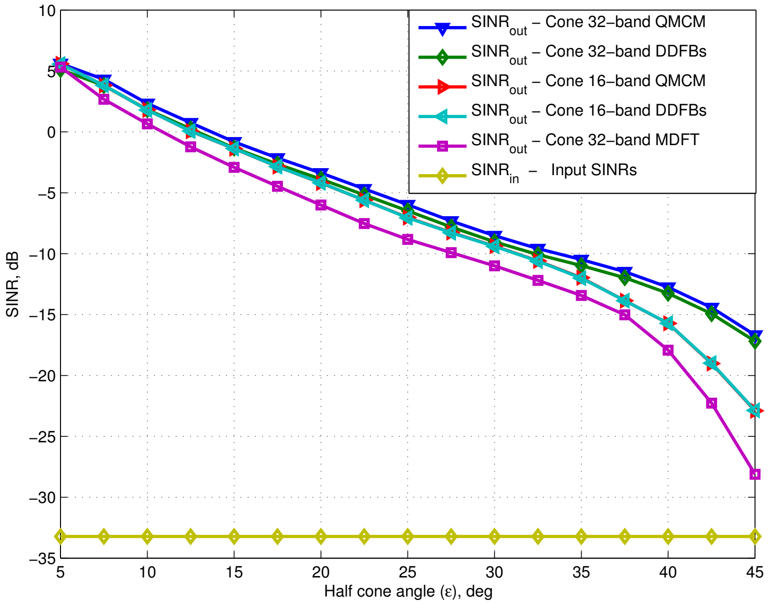

Figure 4.21: Input SINR and output SINR values of 3D 16-band and 32-band QM-CM and DDFB and 32-band MDFT cone filter for DAA signal

4.6.2 Analysis of SINR values obtained with 3D Frustum filters with FPAs

Similar to the DAAs receiver, 15 × 15 elemental antennas arranged in a rectangle with inner spacing of $T_x = T_y = 7.5\,cm$ FPAs (mounded on a paraboloidal reflector) is used as a receiver. The paraboloidal reflector has a diameter of D = 15 m and a focal length F = 6.75 m; therefore, the ratio of the focal length to the diameter F/D is 0.45. The temporal sampling frequency is set to 4.00 GHz. The BB received signal or the input frustum signal $x_{FPA}(n_x, n_y, n_{ct})$ as in Eq. (4.30) consists $SOI_{FPA}(n_x, n_y, n_{ct})$ signal of interest, $RFI1_{FPA}(n_x, n_y, n_{ct})$ first radio frequency interference signal, $RFI2_{FPA}(n_x, n_y, n_{ct})$ second radio frequency interference signal, and $N_{FPA}(n_x, n_y, n_{ct})$ white Gaussian noise and it has a size of (15,15,1024).

$$\begin{aligned} x_{FPA}(n_x, n_y, n_{ct}) = SOI_{FPA}(n_x, n_y, n_{ct}) + RFI1_{FPA}(n_x, n_y, n_{ct}) \\ + RFI2_{FPA}(n_x, n_y, n_{ct}) + N_{FPA}(n_x, n_y, n_{ct}) \end{aligned} \tag{4.30}$$

$RFI1_{FPA}(n_x, n_y, n_{ct})$ and $RFI2_{FPA}(n_x, n_y, n_{ct})$ are numerical synthesized signals that are composed by monochromatic ST PWs Eq. (A.3) [32][33]. On the other hand, the $SOI_{FPA}(n_x, n_y, n_{ct})$ is synthesized with special program that called the Focal Field Synthesizer [44] (Ch. 3). The specification of the $SOI_{FPA}(n_x, n_y, n_{ct})$, $RFI1_{FPA}(n_x, n_y, n_{ct})$ and $RFI2_{FPA}(n_x, n_y, n_{ct})$ are illustrated in Table (4.2) and Figure 4.22 depicted the $SOI_{FPA}(n_x, n_y, n_{ct})$, which has a double frustum shape. Note that the energy of $RFI1_{FPA}(n_x, n_y, n_{ct})$, and $RFI2_{FPA}(n_x, n_y, n_{ct})$ and $N_{FPA}(n_x, n_y, n_{ct})$ are around 20-30 dB higher than the energy of $SOI_{FPA}(n_x, n_y, n_{ct})$; therefore, the $SOI_{FPA}(n_x, n_y, n_{ct})$ is considered to be a weak signal compare to the noise and interference signals. For a review of the BB signal received with FPAs, refer to A.2 and [32].

Signal	(θ, ϕ)	(α, β)	Bandwidth
SOI	$(0°, 0°)$	$(0°, 0°)$	0.5-1.5 GHz
RFI1	$(85°, 40°)$	$(44.89°, 40°)$	0.5-1.2 GHz
RFI2	$(87°, -110°)$	$(44.96°, -110°)$	0.5-1.2 GHz

Table 4.2: Specification of the BB SOI and two terrestrial RFI that received by FPA and using in simulation of 3D cone filters

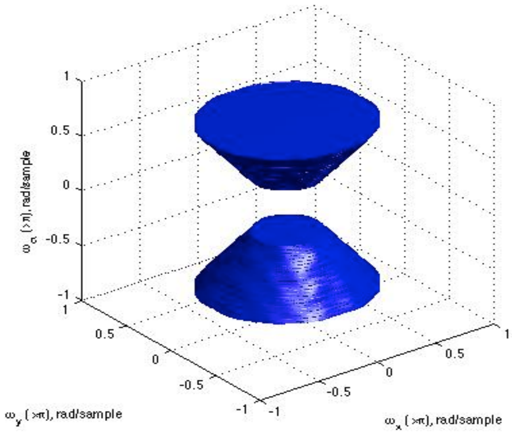

Figure 4.22: ISO-Surface of the normalized magnitude of SOI signal that is received by FPA

During the simulation and SINR evaluation of the input signal, a set of five ST 3D frustum filters with double-frustum shape with bandwidth of 0.5-1.5 GHz are used as in Figures 4.15-4.19. These ST 3D frustum filters are derived from corresponding 32-band 3D MDFT, 16-band and 32-band 3D QM-CM and 16-band and 32-band 3D DDFBs cone filters. The number of bands used to implement these 3D frustum filters are as follows: 18-band for 3D MDFT frustum out of 32-band, 8-band for QM-CM and DDFBs frustum filters out of 16-band, and 16-band for QM-CM and DDFBs frustum filters out of 32-band. The SINR values are evaluated with these five frustum filters at various half-cone angles, which are varying as $40.5°, 40.75°, ..., 44.5°$

The SINR values of the various 3D frustum filters are illustrated in Figure 4.23. The SINR outputs of the 8-band 3D QM-CM and DDFBs frustums filters have improvements with value of 1-2 dB over the 3D MDFT frustum filter. Moreover, with 16-band QM-CM and DDFBs frustum filters, the SINR values show a noticeable improvement with a value of over 2 dB for each angle over the 8-band QM-CM and DDFBs frustum filters.

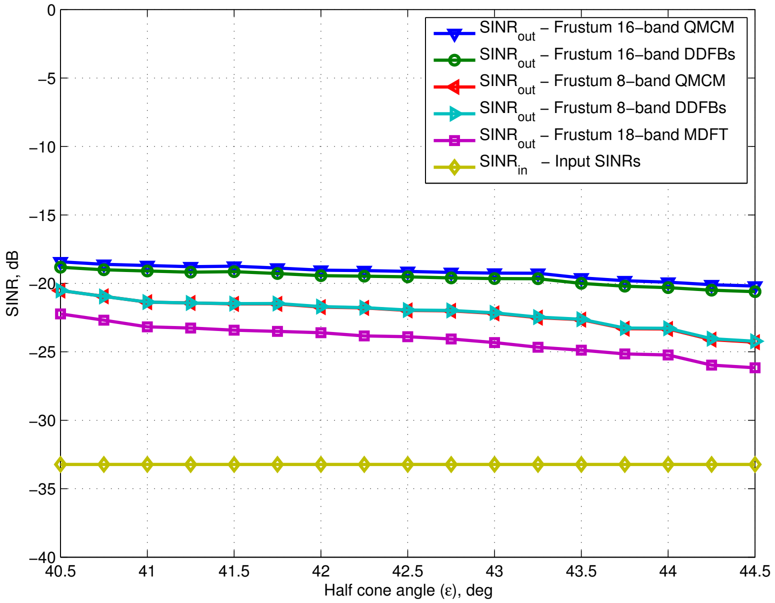

Figure 4.23: Input SINR and output SINR values of 3D 16-band and 32-band QM-CM and DDFB and 32-band MDFT cone filter for FPA signal

4.7 Analysis and Comparison of Computational Complexity of 3D MDFT, QM-CM and DDFBs Cone and Frustum Filters with DAAs and FPAs

The development of engineering applications seeks to achieve more improvements with efficiency. In this section we present the computational complexity and the arithmetical operations such as multiplication and addition required in processing samples, of the above-implemented 3D MDFT, QM-CM and DDFBs cone and frustum filters for SINR applications.

As mentioned in the above sections, all of MDFT [32][33], QM-CM and DDFBs cone filters can be efficiently implemented using poly-phase representation of filter banks. The poly-phase representation has been widely used for efficient implementation of filter banks in many engineering applications [38]. Note that the MDFT, QM-CM and DDFBs frustum filters can also be implemented in the same manner as the MDFT, QM-CM and DDFBs cone filters.

The computational complexity for QM-CM and DDFBs 3D cone filter can be numerically calculated using Eq. (4.31) and Eq.(4.32), respectively. Note that the number of the required multiplication is almost equivalent to number of required addition; therefore, the same equations are used to evaluated the required multiplication and addition.

$$NO._{mul\,QM-CM} = \{\frac{N_{ct}}{M} \times 2 \times 2 \times M + (N_x \times N_y \times M_{imp.\,band})\}\frac{1}{M} \tag{4.31}$$

$$NO._{mul\,DDFBs} = \{N_{ct} \times 2 \times M_{imp.\,band} + (N_x \times N_y \times M_{imp.\,band})\}\frac{1}{M} \tag{4.32}$$

The computational complexity for MDFT [32][33], QM-CM and DDFBs for the case of DAAs and FPAs selectivity filtering applications is numerically calculated and presented in Table (4.3). The computational complexity in this context is calculated to numerically evaluate the multiplication and addition operations required to process only one sample for 3D cone and frustum filters. The 3D QM-CM cone and frustum filters can be implemented with the less computational complexity; moreover, the efficient implementation of the 3D MDFT cone and frustum filters require additional operations over the 3D QM-CM cone and frustum filters. On the other hand, the 3D DDFBs cone filter required more numerical operations to process one sample than the other two 3D cone filters. The poly-phase implementation of the 3D cone and frustum filters decreases the computational complexity greatly.

Type of FB	Type of 3D Filter	Order of Filter	Req. Mul.	Req. Add.
QMCM	Cone	$(40 \times 40 \times 255)$	1745	≈ 1745
QMCM	Frustum	$(14 \times 14 \times 255)$	176.5	≈ 176.5
DDFBs	Cone	$(40 \times 40 \times 255)$	2193	≈ 2193
DDFBs	Frustum	$(14 \times 14 \times 255)$	368.5	≈ 368.5
MDFT [32][33]	Cone	$(40 \times 40 \times 254)$	1921.125	2016.375
MDFT [32][33]	Frustum	$(14 \times 14 \times 254)$	311.75	378.375

Table 4.3: The arithmetic multiplication and addition operations required to process one sample for the efficiently implemented 3D ST QM-CM, DDFBs and MDFT cone and frustum filters

4.8 Summary

In this chapter, two uniform 3D ST cone filters are proposed: the 3D ST QM-CM and DDFBs cone filters. In addition to this, we derive 3D QM-CM and DDFBs frustum filters from the proposed 3D cone filters. The design of these 3D ST cone filters is primarily based on 1D uniform maximally decimated QM-CM Subsection 2.2.2 [34] and DDFBs Subsection 2.2.3 [35]. Any M-band, where M can be even or odd, 3D cone and frustum filters can be designed by designing a M-band uniform QM-CM filter or DDFBs cascaded with M 2D low pass circularly symmetric spatial filters. The total requirements to design any QM-CM or DDFBs 3D cone filters are equivalent to designing the required 1D uniform M-band filter bank and the M 2D circularly symmetric low pass spatial filters.

The double cone shape is approximated with M symmetric discs around the temporal axis ω_{ct} where every disc has height of π/M and radius depends on the cutoff frequency $\omega_{sc,k}$ of the corresponding spatial filter. Any desirable 3D QM-CM and DDFBs frustum filters can be obtained by implementing a set of band $\mathbb{F} \in k$ and disregarding the rest of the bands.

The 3D QM-CM and DDFBs cone filters can be directly implemented as in Figure 4.5 and they can be efficiently implemented with the addition of poly-phase represented of filter bank Section B.1-B.2 as in Figures 4.7, 4.9. The 3D QM-CM and DDFBs frustum filters can be efficiently implemented similar to the 3D QM-CM cone filter by implementing the entire M-band filter bank using $2M$ poly-phase representation and T matrix and the required 2D spatial filters. The rest of the 2D spatial filters can be implemented with substituting their values with zeros. On the other hand, the 3D DDFBs frustum filter can be efficiently implemented by representing the required analysis and synthesis filters by poly-phase representations and implementing the corresponding 2D spatial filters.

In order to investigate the design requirements and performance of the proposed 3D cone and frustum filters, we present an overview of the existing 3D ST MDFT cone and frustum filters. The performance of amplitude response and aliasing distortion for 3D QM-CM, DDFBs and MDFT cone filters is illustrated in Section 4.5. We conclude that M-band 3D QM-CM and DDFBs cone filters have the same approximation of the double cone shape as $2M$-band MDFT cone filter. In term of total maximum aliasing distortion, the MDFT outperforms the QM-CM and DDFBs cone filter because the aliasing distortion of MDFT cone is less. Although the total aliasing distortion of QM-CM and DDFBs is higher than the MDFT cone filters, the effect of this aliasing is negligible during the filtering applications because the proposed QM-CM and DDFBs cone and frustum filters have shown improvements in filtering applications. The amplitude distortion of all implemented 3D cone and frustum filters are small and it is equivalent to [-50 or -60] dB. Moreover, a proof of minor aliasing effect of QM-CM and DDFBs 3D cone filters is discussed in C.1.

To further investigate the performance of the proposed 3D QM-CM and DDFBs can and frustum filters, we test the performance with 3D filtering applications of BB signals received with DAAs and FPAs and evaluate the SINR values for several 3D QM-CM, DDFBs and MDFT cone and frustum filters in Section 4.6. The analysis of SINR reveals that the proposed M-band 3D QM-CM and DDFBs cone and frustum filters have improvement with a value of 1-2 dB over $2M$-band MDFT cone and frustum filter.

To conclude this section, the performance of the proposed 3D QM-CM and DDFBs cone and frustum filters have shown improvement in SINR over the existing 3D MDFT cone and frustum filters; furthermore, the implementation of 3D QM-CM cone and frustum filters are the less than the 3D MDFT and DDFBs cone and frustum filters. 3D MDFT and DDFBs cone and frustum filters require nearly the same number of multiplications and additions.

Chapter 5

3D Spatio-Temporal (ST) Non-Uniform (NU) Cone and Frustum Filters

5.1 Introduction

In literature, various methods have been proposed to design 3D ST cone, frustum, and other filters [10][16][17][32][33][88]-[93], as discussed in Section 4.1. The class of 3D ST cone and frustum filters that is based on filter bank (FB) structure can be considered one of the most popular [10][32][33] and have shown success in video applications, and beamforming of broadband (BB) signals for radio astronomy applications and other applications [10]-[17][32][33]. In addition to their success in 3D filtering applications, 3D ST FB cone and frustum filters are attractive because they can be efficiently implemented.

All of the 3D ST FB cone and frustum filters have been designed with various well-known 1D uniform filter banks (UFBs), such as maximally-decimated and under-decimated DFT, MDFT, previously-proposed QM-CM, and previously-proposed DDFBs in the temporal dimension cascaded with 2D spatial filters. These methods have intensively investigated the 3D uniform bandwidth cone and frustum filters, unlike 3D non-uniform (NU) bandwidth cone and frustum filters. In literature, only one 3D NU bandwidth cone filter has been reported [94]. This 3D ST NU bandwidth cone filter [94] has been proposed for beamforming of BB ST plane waves (PWs). Its design is based on employing 1D NU DFT FB in the temporal dimension cascaded with 3D recursive beam filters [94]. The 1D NU DFT FB is achieved by cascading uniform DFT FBs in the tree structure method; the beam filters are designed by cascading two 3D planer filters as in [12]. In [94], the 3D transfer function can be expressed as in Eq. (5.1).

$$T_{NU-tree}(z_1, z_2, z_3) = \sum_{k=1}^{N} H_k(z_3) T_{BM,k}(z, d_D, \epsilon) \widetilde{H}_k(z_3) \tag{5.1}$$

k includes the number of filters from 1 to N

$$T_{BM,k}(z, d_D, \epsilon) is\, the\, beam\, filter$$

$$H_k(z_3)\, and\, \widetilde{H}_k(z_3)\, are\, analysis\, and\, synthesis\, filters$$

$$d_D\, specifies\, the\, direction\, of\, arrival$$

$$\epsilon\, specifies\, the\, half\, cone\, angle$$

Given the lack of literature on the subject, in this chapter we investigate the design of 3D ST NU cone and frustum filters: We propose two 3D NU cone filters; moreover, we derive two 3D ST NU frustum filters from them. In addition, we test the performance of the proposed 3D NU cone filters in selective filtering of radio astronomy BB signals in cases where the SOI and RFIs are nearly intervening at low temporal frequency.

The organization of this chapter is, as follows: in the Sections 5.2 and 5.3, we present the design details of the two proposed 3D ST UN cone filters; QM-CM and DDFBs, respectively. In Section 5.4, a comparison between the two proposed 3D ST NU cone filters in terms of their magnitude response and aliasing distortion is discussed. We further extend the comparison, in Section 5.5, to consider the SINR values of both 3D ST NU cone filters against uniform QM-CM, DDFBs, and MDFT cone filters. Finally, a summary is presented in Section 5.6.

5.2 Proposed 3D ST NU QM-CM Cone Filter

In this section, a detailed discussion of the proposed 3D ST NU QM-CM cone filter is presented. The proposed 3D ST NU QM-CM cone filter is based on well-known QM-CM NUFB structure, as described in Section 3.3 [36]. The structure of the proposed 3D ST NU QM-CM cone filter, depicted in Figure 5.1, consists of M-band QM-CM

NUFB in temporal direction, and M 2D spatial circularly symmetric low pass filters combined between the temporal analysis and synthesis banks. Thus, each band of the M-band 3D ST QM-CM NU cone filter consists of an analysis filter $H_k(z_{ct})$, a down-sampler, a 2D spatial filter $V_{n_k,k}(z_x, z_y)$, an up-sampler, and a synthesis filter $F_k(z_{ct})$. Note that the analysis filters and synthesis filters have non-uniformly-spaced frequency responses. Therefore, each decimation matrix, $\mathbf{n_k}$ Eq. (5.2), has a different temporal decimation factor, $\mathfrak{n}_k$. The decimation is only performed in the temporal direction; therefore, the decimation matrix $\mathbf{n_k}$ is given by:

$$\mathbf{n}_k = diag[1\,1\,\mathfrak{n}_k] \tag{5.2}$$

$$where\, k = 0, 1, ..., M-1.$$

Note that the temporal component $\mathfrak{n}_k$ varies from one band to another. Furthermore, the QM-CM NUFB is maximally-decimated as defined in Eq. (3.1).

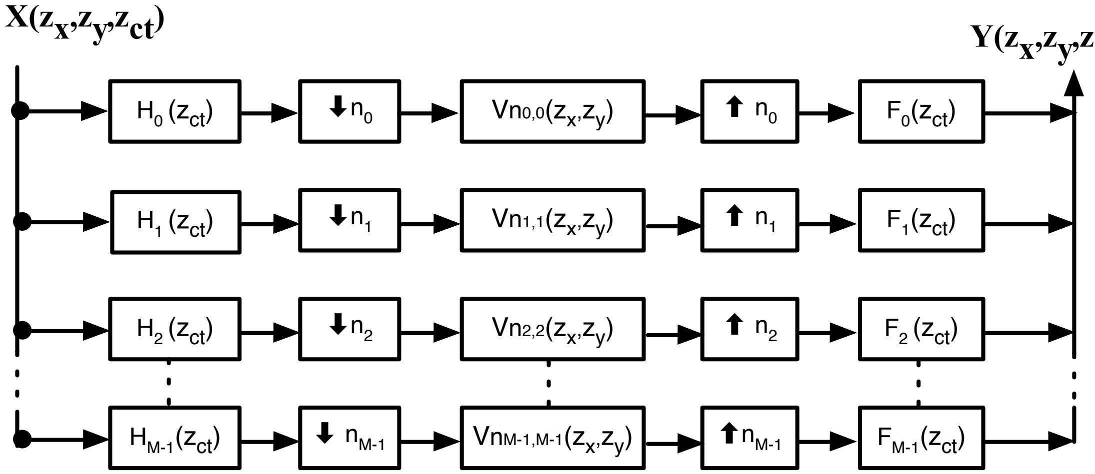

Figure 5.1: Proposed 3D ST QM-CM NU cone filter structure

The proposed 3D ST NU QM-CM cone filter has real NU analysis and synthesis filters; consequently, the frequency responses of analysis and synthesis filters are symmetric around the temporal direction ω_{ct}. This means that each band of the 3D ST NU QM-CM cone filter constructs a symmetric-disc around the temporal domain ω_{ct}, as shown in Figure 5.2. In contrast to a 3D uniform cone filter, each single disc of the 3D ST NU QM-CM cone filter has a height of $\pi/\mathfrak{n}_k$ that depends on the value of the temporal decimation factor $\mathfrak{n}_k$, and a proper radius that increases as the band number increases. Since the height of each disc is inversely proportional to the decimation factor $\mathfrak{n}_k$, a large value for $\mathfrak{n}_k$ results in a small disc height, and vice versa.

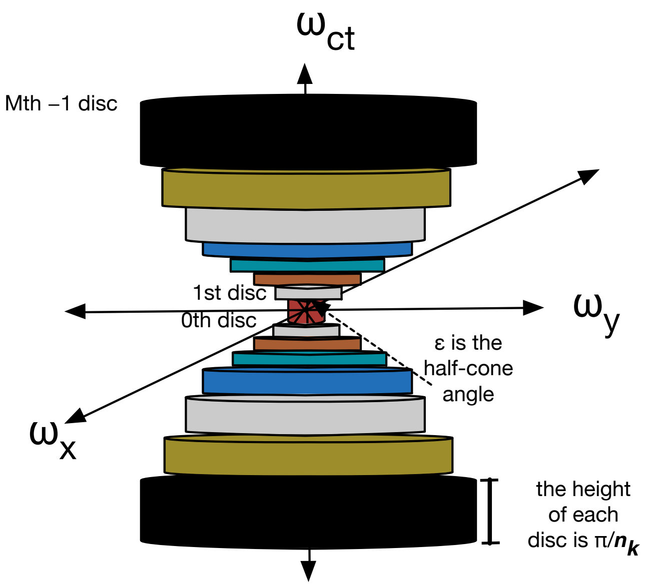

Figure 5.2: The ideal double-cone shape of the 3D ST QM-CM NU cone filter

The design of an M-band 3D ST NU QM-CM cone filter requires of designing a prototype filter, real cosine-modulation of the prototype filter, combining the uniform modulated filters to obtain a NUFB, and designing M 2D spatial circularly-symmetric low-pass filters. For a detailed discussion of the QM-CM NUFB, see Section 3.3 [36].

5.2.1 2D Spatial Circularly-Symmetric Low-Pass Filter Design

The ideal frequency response of the 2D spatial circularly-symmetric low-pass filters is given by Eq. (4.3) [5]. The 2D spatial filters required for designing a 3D ST NU QM-CM cone filter are designed similarly to the 2D spatial filter for uniform cone filters, as presented in Chapter 4. However, for the 3D ST NU QM-CM cone filter, the cutoff frequency, $\omega_{sc,k}$, for the 2D spatial filters is given by Eq. (5.3).

$$\omega_{sc,k} = \frac{(k+1)\pi}{\mathfrak{n}_k} \tan \varepsilon \qquad (5.3)$$
$$k = 0, 1, \cdots, M-1$$

Note that $\mathfrak{n}_k$ is the value of the temporal decimation factor, and it is varies from one band to another because the FB is NU. For the 3D ST NU QM-CM cone filter design,

M 2D spatial filters are required to approximate the required NU double-cone shape.

5.2.2 Efficient Poly-phase Implementation of 3D ST NU QM-CM Cone Filter

Figure 5.1 presents the structure of the proposed 3D ST NU QM-CM cone filter. Moreover, this structure presents a possible direct implementation of the 3D NU QM-CM cone filter; however, this implementation is not efficient, and it requires more computations. In order to efficiently implement the proposed 3D ST NU QM-CM cone filter, the poly-phase representation of the FBs can be utilized. The poly-phase representation of any uniform maximally-decimated FB with poly-phase matrices $\mathbf{E}(\mathbf{z}^{\mathbf{M}})$ and $\mathbf{R}(\mathbf{z}^{\mathbf{M}})$ for the analysis and synthesis filters, respectively, is demonstrated in Section B2. For the proposed 3D ST NU QM-CM cone filter, we can not construct poly-phase matrices because the filters and decimation factors $\mathfrak{n}_k$ are non-uniform. However, we can approach the efficient implementation by representing each analysis and synthesis filter with its $\mathfrak{n}_k$ poly-phase representations. The general efficient implementation of the proposed 3D ST NU QM-CM cone filter, with $\mathfrak{n}_k$ poly-phase representation of each individual filter, is depicted in Figure 5.3. Note that each filter is decomposed to its $\mathfrak{n}_k$ poly-phase components, where $\mathfrak{n}_k$ is the temporal sampling factor of that specific filter. The down-sampling is performed before the analysis filtering, and the up-sampling is performed after the synthesis filtering; consequently, the analysis, spatial and synthesis filtering operations are performed at the lowest rates.

As an example of efficient poly-phase representation, Figure 5.4 presents a 3D ST NU QM-CM cone filter, with decimation factors in the temporal direction of [2 4 4]. The first analysis filter, $H_0(z_{ct})$, is represented using 2 poly-phase filters, $H_{0,0}(z_{ct})$ and $H_{0,1}(z_{ct})$, which are placed after the down-sampler. The same scheme is used for the synthesis filter, $F_0(z_{ct})$. Note that the samplers are delayed with z_{ct}^{mk}, where $mk = 0, -1, ..., -(n_k - 1)$ for the analysis bank, and with z_{ct}^{lk}, where $lk = (n_k - 1), ..., 1, 0$ for the synthesis bank. Similarly to the first filter, the second filter, $H_1(z_{ct})$, and third filter, $H_2(z_{ct})$, are each represented using four poly-phase filters, as shown in Figure 5.4. Note that the analysis filters are decomposed with poly-phase type-1, as in Eq. (5.4); and the synthesis filters are decomposed using poly-phase type-3, as in Eq. (5.5). This implementation results in a great reduction in the computations.

$$H_k(z) = \sum_{l=0}^{n_k-1} z^{-l} H_{kl}(z^M)(\text{type 1 poly-phase}) \tag{5.4}$$

$$F_k(z) = \sum_{l=0}^{n_k-1} z^{M-1-l} F_{kl}(z^M)(\text{type 3 poly-phase}) \tag{5.5}$$

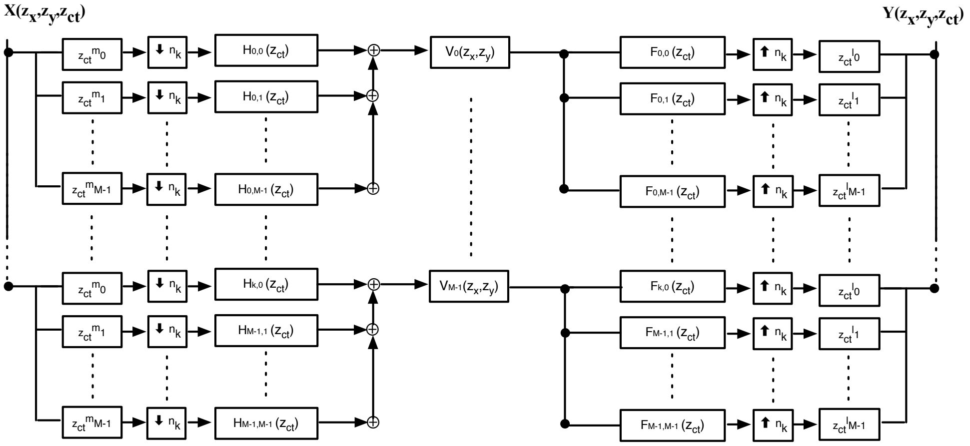

Figure 5.3: Efficient implementation of 3D ST NU QM-CM cone filter using poly-phase representation of each filter

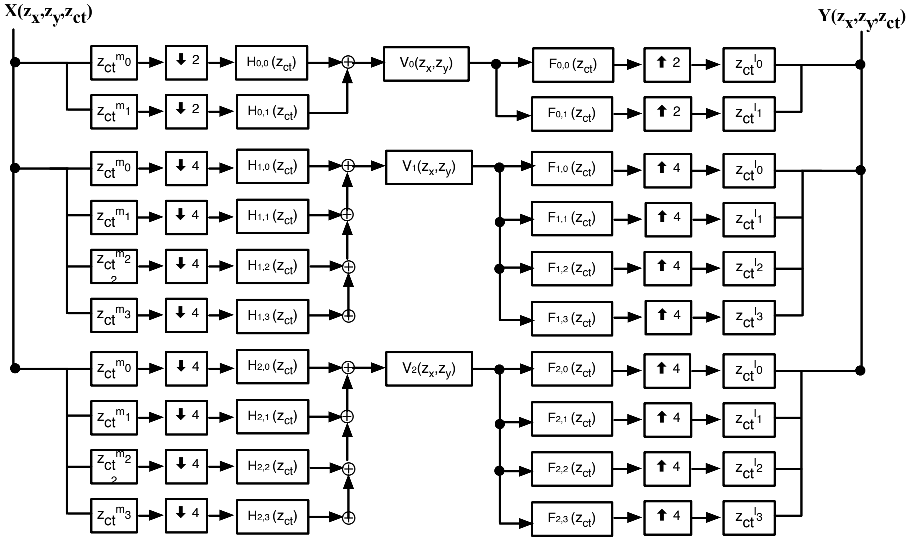

Figure 5.4: An example of efficient implementation of a 3D ST NU QM-CM cone filter, where the decimation for the temporal filter bank is [2 4 4]

5.2.3 Input and Output Relationship of the 3D ST NU QM-CM Cone Filter

The 3D output of the 3D ST NU QM-CM cone filter can be derived by analysing its structure see Figure 5.1 and the input-output relationship of the 1D QM-CM NUFBs see Eq. (3.6). The structure of the 3D ST NU QM-CM cone filter illustrates that 3D output could be obtained by combining the filter bank output equation with the 2D spatial filters. The total output, $Y_{QM-CM\,NU}(z_x, z_y, z_{ct})$, of the 3D ST NU QM-CM cone filter is presented in Eq. (5.6), and consists of the desired response, $D_{QM-CM\,NU}(z_x, z_y, z_{ct})$, shown in Eq. (5.7), and the aliasing distortion, $A_{QM-CM\,NU}(z_x, z_y, z_{ct})$, calculated by Eq. (5.8).

$$Y_{QM-CM\,NU}(z_x, z_y, z_{ct}) = \sum_{k=0}^{M-1} \sum_{l=0}^{\mathfrak{n}_k-1} \frac{1}{\mathfrak{n}_k} H_k(z_{ct}W_M^l) V_{n_k,k}(z_x, z_y) F_k(z_{ct}) X(z_x, z_y, z_{ct}W_M^l) \tag{5.6}$$

$$D_{QM-CM\,NU}(z_x, z_y, z_{ct}) = \sum_{k=0}^{M-1} \frac{1}{\mathfrak{n}_k} H_k(z_{ct}) V_{n_k,k}(z_x, z_y) F_k(z_{ct}) \tag{5.7}$$

$$A_{QM-CM\,NU}(z_x, z_y, z_{ct}) = \sum_{k=0}^{M-1} \sum_{l=0}^{\mathfrak{n}_k-1} \frac{1}{\mathfrak{n}_k} H_k(z_{ct}W_M^l) V_{n_k,k}(z_x, z_y) F_k(z_{ct}) \tag{5.8}$$

Note that the desired response, $D_{QM-CM\,NU}(z_x, z_y, z_{ct})$, corresponds to when the aliasing term contains $l = 0$, and the aliasing distortion, $A_{QM-CM\,NU}(z_x, z_y, z_{ct})$, consists of $\mathfrak{n}_k - 1$ aliasing terms for each band, where $\mathfrak{n}_k$ varies from one band to another.

5.2.4 The Derivation of a 3D ST NU QM-CM Frustum Filter

Similar to the uniform 3D frustum filter in Chapter (4), any desired 3D ST NU QM-CM frustum filter can be obtained by implementing a required set of bands, $\mathbb{F}$, to approximate the NU frustum double shape.

The 3D output signal, $Y_{QM-CMfrus\,NU}(z_x, z_y, z_{ct})$, of the derived 3D ST NU QM-CM frustum filter, as presented in Eq. (5.9), can be obtained from the original 3D output, $Y_{QM-CM\,NU}(z_x, z_y, z_{ct})$, of the 3D ST NU QM-CM cone filter, seen in Eq. (5.6). Furthermore, the 3D output $Y_{QM-CMfrus\,NU}(z_x, z_y, z_{ct})$, of the derived 3D ST NU QM-

CM frustum filter consists of the desired response, $D_{QM-CMfrus\,NU}(z_x, z_y, z_{ct})$, shown in Eq. (5.10), and the aliasing distortion, $A_{QM-CMfrus\,NU}(z_x, z_y, z_{ct})$, calculated by Eq. (5.11).

$$Y_{QM-CMfrus\,NU}(z_x, z_y, z_{ct}) = \sum_{k\in\mathbb{F}} \sum_{l=0}^{M-1} \frac{1}{\mathfrak{n}} H_k(z_{ct}W_M^l) V_{n_k,k}(z_x, z_y) F_k(z_{ct}) X(z_x, z_y, z_{ct}W_M^l) \tag{5.9}$$

$$D_{QM-CMfrus\,NU}(z_x, z_y, z_{ct}) = \sum_{k\in\mathbb{F}} \frac{1}{\mathfrak{n}} H_k(z_{ct}) V_{n_k,k}(z_x, z_y) F_k(z_{ct}) \tag{5.10}$$

$$A_{QM-CMfrus\,NU}(z_x, z_y, z_{ct}) = \sum_{k\in\mathbb{F}} \sum_{l=0}^{M-1} \frac{1}{\mathfrak{n}} H_k(z_{ct}W_M^l) V_{n_k,k}(z_x, z_y) F_k(z_{ct}) \tag{5.11}$$

5.3 Proposed 3D ST NU DDFBs Cone Filter

In the same manner as the previous 3D ST NU QM-CM cone filter, another 3D NU cone filter is proposed; in this case, it is called the 3D ST NU DDFBs cone filter because its structure is composed of an M-band 1D NU DDFBs see Section 3.4 [35] in the temporal direction, combined with 2D circularly-symmetric low-pass spatial filters [5]. The structures of the 3D ST NU QM-CM cone filter and the 3D ST NU DDFBs cone filter are exactly identical, as depicted in Figure 5.1. Hence, the new 3D ST NU DDFBs cone filter also consists of analysis filters, down-samplers, 2D spatial filters, up-samplers and synthesis filters. Note that the down-sampling and up-sampling are performed in the temporal direction only; therefore, the $\mathbf{n_k}$ is a diagonal matrix and is given by Eq. (5.2).

The NU analysis and synthesis filters of the 3D ST NU DDFBs cone filter are real filters, so they have symmetric frequency response around the temporal domain ω_{ct}. The required double-cone shape is approximated with NU symmetric discs that have varying height of $\pi/\mathfrak{n}_k$, which depends on the temporal decimation factors and proper radius, as illustrated in Figure 5.2.

The cost of designing a 3D ST NU DDFBs cone filter is equivalent to designing an M-band NU DDFBs and M 2D spatial filters. The advantage of DDFBs [35] is flexibility, because we can design any NU DDFBs with various compatible or non-compatible sampling sets, with any filter length N [35].

5.3.1 2D Spatial Circularly-Symmetric Low Pass Filters Design

The 2D spatial filters for the new 3D ST NU DDFBs cone filter are exactly designed as the 2D spatial filters for the uniform cone filter in Chapter (4). However, the cutoff frequency for each 2D spatial filter is given by Eq. (5.3) see Subsection 5.2.1.

5.3.2 Efficient Poly-phase Implementation of 3D ST NU DDFBs Cone Filter

The efficient implementation of the proposed 3D ST NU DDFBs cone filter can be achieved by representing the analysis and synthesis filters as their $\mathfrak{n}_k$ poly-phase components. The same representation for the 3D ST NU QM-CM cone filter, seen in Figure 5.3, is applicable for the proposed 3D ST NU DDFBs see Subsection 5.2.2.

5.3.3 Input and Output Relationship of the 3D ST NU DDFBs Cone Filter

The DDFBs discussed in Subsection 2.2.3 and Section 3.4 [35] is a general FB that can be used to design uniform and NU analysis and synthesis filters with compatible or non-compatible sampling sets. Therefore, the input and output equation of the filter bank, labelled as Eq. (2.14) [35], can be used to describe the input and output of uniform and NU DDFBs. Consequently, the 3D output of the 3D ST NU DDFBs cone filter can be evaluated using Eq. (4.23); moreover, the desired function and aliasing distortion can be derived as in Eq. (4.24) and Eq. (4.25), respectively.

5.3.4 The Derivation of a 3D ST NU DDFBs Frustum Filter

The 3D ST NU DDFBs frustum filter can be derived from the proposed 3D ST NU DDFBs cone filter by implementing the required set of bands, $\mathbb{F}$, to approximate the desired frustum filter shape, and disregarding the rest of the bands. The same argument for the input and output of the 3D ST DDFBs UN cone filter can be applied for the 3D ST NU DDFBs frustum filter. Therefore, Eq. (4.26) to Eq. (4.28) can be used to evaluate the total 3D output, desired function, and aliasing distortion of the 3D ST NU DDFBs frustum filter, respectively.

5.4 Performance Analysis of ST 3D QM-CM and DDFBs NU Cone Filters

In this section, we present a comparison between the proposed 3D ST NU QM-CM and DDFBs cone filters, to determine the efficiency and accuracy of each method. In this presentation, two 3D ST NU QM-CM cone filters and two 3D ST NU DDFBs cone filters are designed and compared. The first 3D ST NU QM-CM and DDFBs cone filters have specifications as listed in the column labelled 'First Cone' in Table (5.1), and the second 3D ST NU QM-CM and DDFBs cone filter have specifications as listed under 'Second Cone'. Note that in order to make the comparison equitable, the first 3D ST NU QM-CM and DDFBs cone filters have exact specifications; furthermore, the second 3D ST NU QM-CM and DDFBs cone filters have identical specifications.

In this comparison, the performance of NU QM-CM and DDFBs cone filters is analysed by investigating their magnitude response, aliasing distortion, and amplitude distortion. The magnitude response is analysed to reveal the smoothness and accuracy of the approximated NU double-cone shape, and aliasing and amplitude distortions are tested to investigate the level of distortion of the two methods.

The magnitude response, aliasing distortion, and frequency response of the NU analysis bank of the First Cone 3D ST NU QM-CM and DDFBs cone filters are plotted in Figures 5.5 and 5.6, respectively. The frequency response is presented to illustrate how the NU discs approximate the 3D NU cone filters. Subjectively, the magnitude responses of both NU QM-CM and DDFBs cone filters have approximated the specified NU double-cone shape with NU discs. The NU double-cone filters have thin discs at low frequency and wider discs at higher frequencies. Furthermore, the magnitude response of the QM-CM see Figure 5.5 has smoother and more accurate NU cone approximation than the magnitude response of DDFBs see Figure 5.6. Unfortunately, the aliasing distortion, which is calculated as the maximum of the total aliasing distortion, is generally quite high for both methods; however, performance of the QM-CM cone filter is better than the DDFBs cone filter. In terms of amplitude distortion, -45 dB is the maximum, which is considered very small.

For the Second Cone filters, the magnitude response, aliasing distortion, and frequency response of the NU analysis bank for 3D ST NU QM-CM and DDFBs cone filters are depicted in Figures 5.7 and 5.8, respectively. Frequency response demonstrates that both QM-CM and DDFBs have achieved excellent smooth NU double cone shape approximation. Additionally, the NU QM-CM cone filter has more noticeable accuracy and smoothness than the DDFBs NU cone filter. The aliasing distortion is high for both cases; however, the DDFBs NU cone has more aliasing distortion than the QM-CM NU cone filter. The amplitude distortion for the 3D ST NU QM-CM and DDFBs cone filters is small, and it is equivalent to -45 dB.

To summarize this comparison, both 3D ST NU QM-CM and DDFBs cone filters have achieved the required specifications, because the approximation of the required 3D ST NU cone filters is achieved. The QM-CM method tends to have more accurate and smooth discs for the approximated NU cone filters as shown by the magnitude response in Figures 5.5 and 5.7. The aliasing distortion is quite high for both methods; however, the aliasing distortion for designed QM-CM cone filters is less than the DDFBs. Regardless this aliasing distortion has minor effect, the analysis of 3D filtering applications in the next section will prove the negligible aliasing effect of the new proposed 3D ST NU QM-CM and DDFBs cone filters.

Specifications	First Cone	Second Cone
Total number of band	16	16
Total number of 2D filter	16	16
Decimation set	[32 32 32 32 16 16 16 16 16 16 16 16 16 16 8 8]	[32 32 32 32 32 32 32 32 16 16 16 16 8 8 8 8]

Table 5.1: Specifications of two NU cone filters designed using the proposed QM-CM and DDFBs NU methods

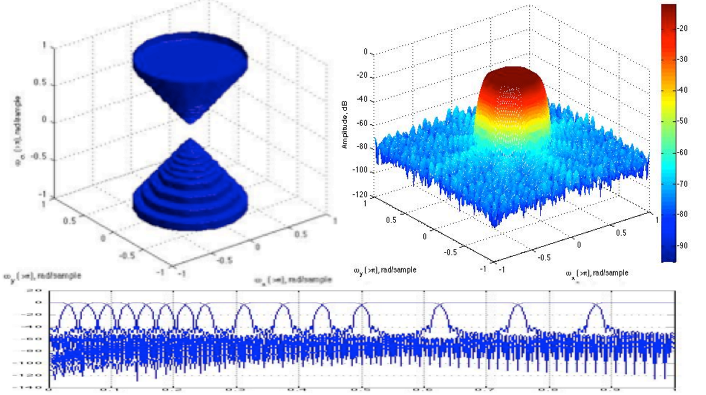

Figure 5.5: Normalized magnitude response and the maximum aliasing distortion for each spatial frequency of First Cone QM-CM NU cone filter, and frequency response of the NU analysis filters

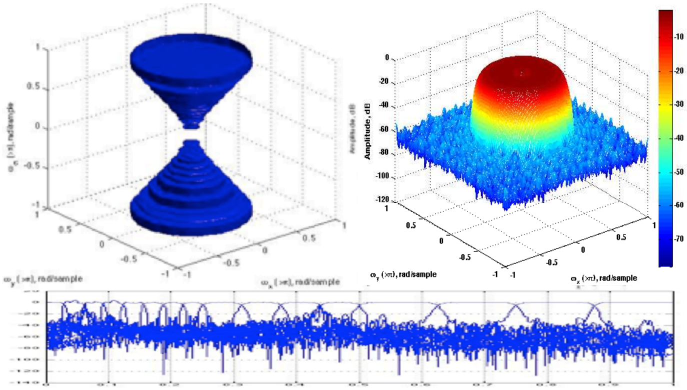

Figure 5.6: Normalized magnitude response and the maximum aliasing distortion for each spatial frequency of First Cone DDFBs NU cone filter, and frequency response of the NU analysis filters

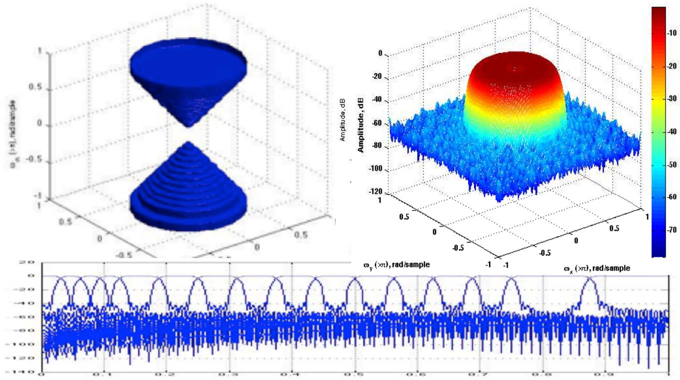

Figure 5.7: Normalized magnitude response and the maximum aliasing distortion for each spatial frequency of Second Cone QM-CM NU cone filter, and frequency response of the NU analysis filters

5.5 Analysis and Comparison of SINR Obtained with 3D MDFT, Uniform and NU QM-CM and DDFBs Cone Filters with DAAs

In Section 5.3, a comparison between the new proposed 3D ST NU QM-CM and DDFBs cone filters was presented. During the comparison, some observations and analysis for the magnitude response, aliasing distortion, and amplitude distortion for two NU QM-CM and two NU DDFBs cone filters were highlighted. The comparison aimed at revealing the efficiency and accuracy of the proposed QM-CM and DDFBs NU methods in approximating the specified 3D ST NU cone filters. Furthermore,

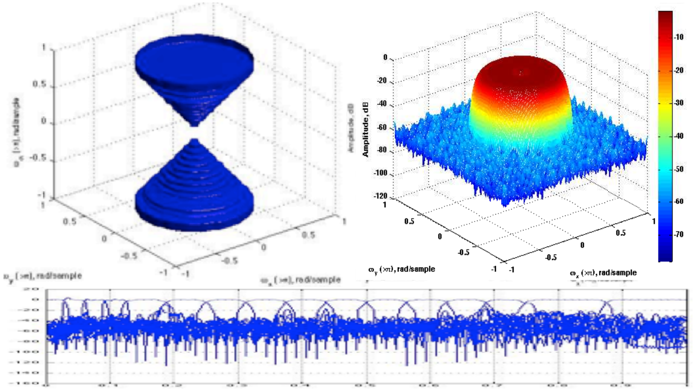

Figure 5.8: Normalized magnitude response and the maximum aliasing distortion for each spatial frequency of Second Cone DDFBs NU cone filter, and frequency response of the NU analysis filters

it was concluded that both methods achieved good approximation and accuracy. Moreover, the QM-CM method shows excellent NU cone approximation with smooth discs, seen as flat and ripple-free pass band response through the QM-CM filter bank. In addition, the amplitude distortion was equivalent to -45 dB. However, the aliasing distortion for both methods was quite high but it has negligible effect during filtering applications.

In this section, we further extend our comparison to test and measure the performances of the new proposed 3D ST NU QM-CM and DDFBs cone filters in 3D filtering application, and compare them with other 3D ST cone filters. In the following application, we test and evaluate the performance of the two designed 3D ST NU QM-CM cone filters, from Section 5.2, and the two designed 3D NU ST DDFBs cone filters, from Section 5.3, in improving the SINR of BB signals. Moreover, the performances of the existing MDFT cone filters [32], and previously-proposed uniform QM-CM and DDFBs from Chapter (4) are tested, and their SINR outputs are evaluated for comparison. Note, in order to make the evaluation and comparison reasonable, we used equivalent number of discs or bands for all 3D ST cone filters, as listed in the following:

1. NU QM-CM filter, with specifications of First Cone in Table 5.1;
2. NU QM-CM filter, with specifications of Second Cone in Table 5.1;
3. NU DDFBs filter, with specifications of First Cone in Table 5.1;
4. NU DDFBs filter, with specifications of Second Cone in Table 5.1;

5. 32-band MDFT uniform filter, as developed in [32];
6. 16-band uniform QM-CM filter, as designed in Section 4.3; and,
7. 16-band uniform DDFBs filter, as designed in Section 4.4.

The BB signal used in this simulation consists of the BB SOI, two BB radio-frequency interference signals, and Gaussian noise; moreover, these signals are received by DAAs. The BB SOI and two RFI signals are plotted in Figure 5.9, and their specifications are given in Table 5.2. The DAAs receiver is briefly discussed in Section A.1 of the Appendix; for more detail refers to [32].

Signal	(θ, ϕ)	(α, β)	Bandwidth
SOI	$(0°, 0°)$	$(0°, 0°)$	0.1-2 GHz
RFI1	$(85°, 40°)$	$(44.89°, 40°)$	0.1-1.2 GHz
RFI2	$(87°, -110°)$	$(44.96°, -110°)$	0.1-1.3 GHz

Table 5.2: Specification of the test signal components used in 3D filtering application

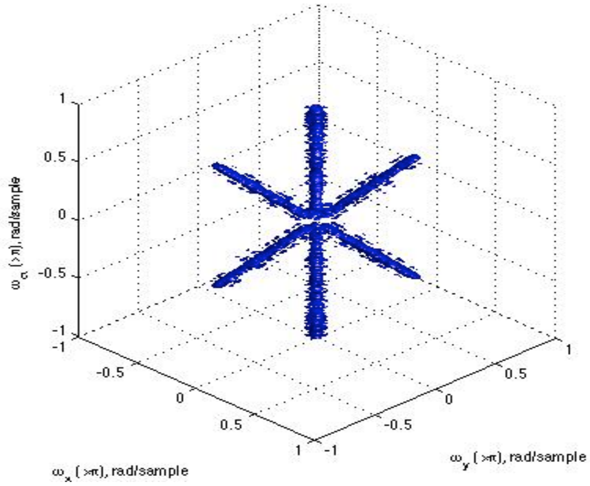

Figure 5.9: ISO-Surface of the normalized magnitude of the test signal used in 3D filtering application

During the simulation, a set of the seven above-listed 3D ST cone filters, with varying half-cone angles, as $5°, 7.5°, ..., 45°$ are used to evaluate the SINR values. Note that we refer to the cone filters by their name and number as in the list above.

The SINR values of the seven 3D ST cone filters, over a range of half-cone angles from 5° to 45° in 2.5° increments, are plotted in Figure 5.10. The input SINR is equal to -31 dB. In general, the SINR values are effective starting from an angle of 5°, and decrease as the half-cone angle increases. This is because more energy in the form of noise and interference signals is intruded to the band pass of the 3D ST NU cone filters. From the angles of 5° to 25°, all of the 3D ST NU cone filters have a slight improvement in SINR values over the 3D ST uniform QM-CM, DDFBs, and MDFT cone filters; moreover, the SINR values of 3D ST NU cone filters with an angle higher than 25° have some improvement over the 3D ST uniform QM-CM, DDFBs, and MDFT cone filters.

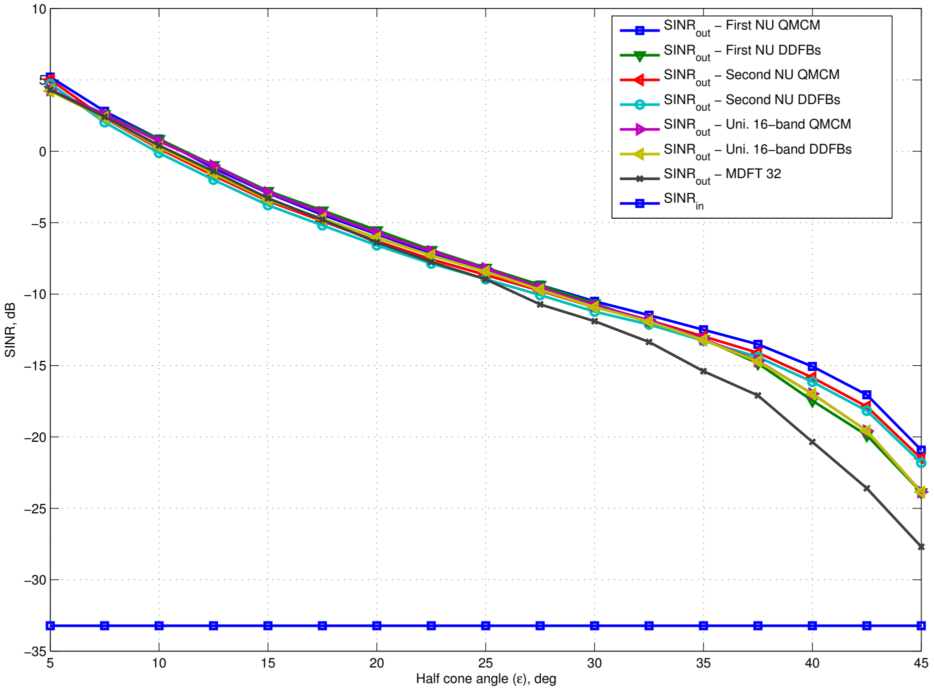

Figure 5.10: Input SINR and output SINR values of seven 3D cone filters for DAA signal

5.6 Summary

In this chapter, two 3D ST NU cone filters are proposed; specifically, a 3D ST NU QM-CM cone filters and a 3D ST DDFBs NU cone filter. Moreover, two 3D ST NU frustum filters are derived from the proposed 3D ST NU QM-CM and DDFBs cone filters. Essentially, the design of the two proposed NU cone filters is based on NUFBs and 2D spatial filters. The NU QM-CM and DDFBs filter banks are implemented in the temporal domain, and the 2D spatial filters are implemented in the spatial domain. Each band of the 3D ST NU cone and frustum filters, diagrammed in Figure 5.1, creates a disc with varying height dependant on the temporal decimation factor, and appropriate radius dependant on the specified cone angle. The 3D ST NU frustum filters can be obtained from the 3D ST NU cone filters by implementing a required set of bands to achieve the desired double frustum shape.

In order to illustrate the accuracy and quality of NU 3D cone approximation of the proposed QM-CM and DDFBs, two ST NU QM-CM and two 3D ST NU DDFBs cone filters were designed; and their magnitude response and aliasing distortion were presented in Section 5.4. The comparison reveals that DDFBs method achieves good approximation of specified NU cone filters; furthermore, although their aliasing distortion is apparently quite high, it has negligible effect during 3D filtering applications. On the other hand, the QM-CM NU method achieves very accurate NU cone approximation with less aliasing distortion than the DDFBs NU method.

The performance of the proposed 3D ST NU QM-CM and DDFBs filters and uniform QM-CM, DDFBs, and MDFT cone filters were tested, and SINR values were evaluated in the 3D selective filtering of BB signals received with DAAs. The simulation results showed that the SINR values for the 3D ST NU QM-CM and DDFBs cone filters have a slight improvement over uniform 3D ST cone filters, if the half-cone angle is less than 25°. Moreover, there is some improvement in SINR values for 3D ST NU QM-CM and DDFBs cone filters over the 3D uniform filters at higher angles.

Finally, the proposed 3D ST NU QM-CM and DDFBs cone and frustum filters can be efficiently implemented and utilized in selective filtering of BB signals to improve SINR values. The 3D ST NU QM-CM and DDFBs cone filters can be utilized in selective filtering in cases where the radio interference signals are almost intervened with SOI at low temporal frequency. However, in such cases, the cone approximation must be very smooth and fine to pass the SOI and reject the RFI signals. Three-dimensional ST NU cone filters can be used in these applications because we can design a 3D ST NU cone with smooth discs at low temporal frequency, and appropriate discs at high frequency, to achieve better improvement of SINRs with low computational cost.

Chapter 6

A Summary and Conclusions

6.1 Conclusions

The major objectives of the thesis are to design two uniform and two non-uniform 3D ST FIR cone and frustum filters, using well-known filter banks - namely uniform and non-uniform QM-CM and DDFBs -, to evaluate their performance in selective filtering in radio astronomy applications, and to compare their performance with the existing 3D ST MDFT cone and frustum filters. In addition, the objectives of proposing NUFB for implementations of 3D ST cone filters are to study and investigate the 3D ST NU cone and frustum filters that have not been intensively studied, and to evaluate their performance in radio astronomy BB signals in the presence of RFI disturbances, and then compare their performance with other 3D ST uniform cone filters.

In order to achieve these objectives, we intensively analysed and studied uniform FBs in Chapter 2 especially MDFT, QM-CM, and DDFBs. Furthermore, in Chapter 3, NUFB design methods were reviewed and a thorough study and analysis of NU QM-CM and DDFBs is presented. In Chapter 4, two uniform 3D ST FIR cone filters were proposed namely QM-CM and DDFBs 3D ST cone filters that can be utilized in various 3D filtering applications, especially selective filtering of astronomical BB signals. Moreover, uniform 3D ST QM-CM and DDFBs frustum filters were derived from the original 3D ST QM-CM and DDFBs cone filters. The design of 3D ST QM-CM and DDFBs cone filters is achieved by cascading 1D uniform M-band QM-CM or DDFBs filter banks with M 2D spatial low-pass circularly-symmetric filters. The performance of the proposed 3D ST QM-CM and DDFBs cone and frustum filters were tested in selective filtering of BB signals to enhance SOI and attenuate strong RFI signal and noise in DAAs and FPAs applications. The simulation results showed that the proposed uniform 3D ST QM-CM and DDFBs cone and frustum filters have improved SINR values over the 3D ST FIR MDFT cone filter that proposed in [32]. Besides the excellent performance of both the 3D ST QM-CM and DDFBs filters, the 3D ST QM-CM filters can be efficiently implemented with the lowest computational requirement using $2M$ poly-phase representation, compared to 3D MDFT and DDFBs cone and frustum filters, as illustrated in Section 4.7. On the other hand, the 3D ST DDFBs cone and frustum filters can be efficiently implemented using M poly-phase representation, as demonstrated in Section 4.7, but require extra more computations compared to 3D ST QM-CM and MDFT cone and frustum filters.

In Chapter 5, another 3D ST QM-CM and DDFBs cone filters that have NUFB structures are proposed. Moreover, non-uniform 3D ST QM-CM and DDFBs frustum filters are derived from the two proposed non-uniform 3D ST QM-CM and DDFBs cone filters. The objectives of this chapter were to study and investigate the designed non-uniform 3D ST cone and frustum filters, and to enhance and improve the selective filtering of broadband SOI, in cases where the SOI and RFI signals have almost overlapping ROS at low temporal frequencies. In such cases, a non-uniform 3D ST QM-CM or DDFBs filter with very smooth cone approximation at low frequencies, and appropriate band width at high frequency, can be used to improve and enhance the SOI and attenuate the RFI with low cost. In Section 5.5, the simulation results confirmed that non-uniform 3D ST QM-CM and DDFBs filters with thin discs at low frequencies, and thicker discs at high frequencies, can slightly improve the SINR over the proposed uniform QM-CM and DDFBs cone filters, and the previously-proposed 3D ST MDFT cone filter. In addition to their improvement in filtering applications, the non-uniform QM-CM and DDFBs 3D ST cone filter can be efficiently implemented using poly-phase representation of filter banks, as illustrated in Section 5.2.

6.2 Future Work

There are several analysis the work presented in the thesis can be extended. Two are briefly mentioned here:

- Other applications:
  3D ST filtering techniques are not limited for broadband beamforming of as-

tronomical signals; they can also be utilized in many applications in several fields. For example, 3D ST wide-angle stop-band cone and frustum filters can be used in linear trajectory signals to enhance a moving object with a constant 2D spatial velocity over time [10]. Furthermore, 3D ST filtering techniques have potential applications in other applications such as: motion detection, video image compression, 3D object detection, and 3D image de-noising [93]. In addition, 3D ST techniques can be used in tracking applications to track and observe an object with nearly constant 2D spatial velocity over a limited area. These applications are of great importance in surveillance systems for security. Other applications in 3D image processing include: biomedicine, robotics, and geophysics [17]. These are some potential applications for 3D ST filters, not to mention their importance in beamforming of broadband signals in wireless communications.

- Improve the 2D spatial filter design:
  The efficiency of 3D cone and frustum filters can be greatly improved by utilizing 2D IIR spatial filters. A class of 2D IIR spatial filter can be designed by optimization using symmetry [95].

Bibliography

[1] C. U. Edussooriya, D. G. Dansereau, L. T. Bruton, and P. Agathoklis, "Five-dimensional depth-velocity filtering for enhancing moving objects in light field videos," *Signal Processing, IEEE Transactions on*, vol. 63, no. 8, pp. 2151–2163, 2015.

[2] D. Dansereau and L. T. Bruton, "A 4-d dual-fan filter bank for depth filtering in light fields," *Signal Processing, IEEE Transactions on*, vol. 55, no. 2, pp. 542–549, 2007.

[3] A. Madanayake, R. Wimalagunarathne, D. G. Dansereau, R. J. Cintra, and L. T. Bruton, "Vlsi architecture for 4-d depth filtering," *Signal, Image and Video Processing*, pp. 1–10, 2013.

[4] H. A. Madanayake and L. T. Bruton, "Digital filtering of toroidal sensor-array signals using 3d iir frequency-planar filters," in *Circuits and Systems, 2007. NEWCAS 2007. IEEE Northeast Workshop on*, pp. 598–601, IEEE, 2007.

[5] D. E. Dudgeon and R. M. Mersereau, *Multidimensional Digital Signal Processing Prentice-Hall Signal Processing Series.* Prentice-Hall, Englewood Cliffs, NJ, 1984.

[6] A. Madanayake, C. Wijenayake, D. G. Dansereau, T. K. Gunaratne, L. T. Bruton, and S. B. Williams, "Multidimensional (md) circuits and systems for emerging applications including cognitive radio, radio astronomy, robot vision and imaging," *Circuits and Systems Magazine, IEEE*, vol. 13, no. 1, pp. 10–43, 2013.

[7] T. Ajdler, L. Sbaiz, and M. Vetterli, "The plenacoustic function and its sampling," *Signal Processing, IEEE Transactions on*, vol. 54, no. 10, pp. 3790–3804, 2006.

[8] J. W. Woods, *Multidimensional signal, image, and video processing and coding.* Academic press, 2006.

[9] L. T. Bruton and N. Bartley, "The design of highly selective adaptive three-dimensional recursive cone filters," *Circuits and Systems, IEEE Transactions on*, vol. 34, no. 7, pp. 775–781, 1987.

[10] C. U. Edussooriya, L. T. Bruton, and P. Agathoklis, "A low-complexity 3d spatio-temporal fir filter for enhancing linear trajectory signals," in *Acoustics, Speech and Signal Processing (ICASSP), 2014 IEEE International Conference on*, pp. 1165–1169, IEEE, 2014.

[11] L. Bruton, "Selective filtering of spatio-temporal plane waves using 3d cone filter banks," in *Communications, Computers and signal Processing, 2001. PACRIM. 2001 IEEE Pacific Rim Conference on*, vol. 1, pp. 67–70, IEEE, 2001.

[12] L. Bruton, "Three-dimensional cone filter banks," *Circuits and Systems I: Fundamental Theory and Applications, IEEE Transactions on*, vol. 50, no. 2, pp. 208–216, 2003.

[13] L. T. Bruton, "A 3d polyphase-dft cone filter bank for broad band plane wave filtering," in *Circuits and Systems, 2004. ISCAS'04. Proceedings of the 2004 International Symposium on*, vol. 3, pp. III–181, IEEE, 2004.

[14] L. Bruton and S. Singh, "Plane wave filtering using a novel 3d cone-stop filter bank," in *Circuits and Systems, 2002. MWSCAS-2002. The 2002 45th Midwest Symposium on*, vol. 3, pp. III–676, IEEE, 2002.

[15] B. Kuenzle and L. T. Bruton, "3-d iir filtering using decimated dft-polyphase filter bank structures," *Circuits and Systems I: Regular Papers, IEEE Transactions on*, vol. 53, no. 2, pp. 394–408, 2006.

[16] N. Liyanage, *3D space-time digital filtering for radio astronomy.* PhD thesis, 2009.

[17] N. Liyanage, L. Bruton, and P. Agathoklis, "On the attenuation of interference and mutual coupling in antenna arrays using 3d space-time filters," in *Communications, Computers and Signal Processing, 2009. PacRim 2009. IEEE Pacific Rim Conference on*, pp. 146–151, IEEE, 2009.

[18] T. K. Gunaratne and L. T. Bruton, “Broadband beamforming of dense aperture array (daa) and focal plane array (fpa) signals using 3d spatio-temporal filters for applications in aperture synthesis radio astronomy,” *Multidimensional Systems and Signal Processing*, vol. 22, no. 1-3, pp. 213–236, 2011.

[19] N. Liyanage, L. Bruton, P. Agathoklis, and C. Edussooriya, “Space-time digital filtering of radio astronomical signals using 3-d cone filters,” in *Proceedings of RFI Mitigation Workshop*, pp. 1–7, 2010.

[20] P. E. Dewdney, P. J. Hall, R. T. Schilizzi, and T. J. L. Lazio, “The square kilometre array,” *Proceedings of the IEEE*, vol. 97, no. 8, pp. 1482–1496, 2009.

[21] P. Gibson, “The vivaldi aerial,” in *Microwave Conference, 1979. 9th European*, pp. 101–105, IEEE, 1979.

[22] R. T. Schilizzi, P. E. Dewdney, and T. J. W. Lazio, “The square kilometre array,” in *SPIE Astronomical Telescopes+ Instrumentation*, pp. 773318–773318, International Society for Optics and Photonics, 2010.

[23] P. Dewdney and T. Lazio, “The square kilometer array (ska) radio telescope: Progress and technical directions,” *Radio Science Bulletin*, no. 326, p. 5, 2008.

[24] P. Hall, “The square kilometre array: An international engineering perspective,” in *The Square Kilometre Array: An Engineering Perspective*, pp. 5–16, Springer, 2005.

[25] R. Schilizzi, P. Alex, J. Cordes, P. Dewdney, R. Ekers, B. Gaensler, P. Hall, J. Jonas, and K. Kellermann, “Preliminary specifications for the square kilometre array, ska memo 100,” in *Antennas and Propagation Society International Symposium 2006, IEEE*, Citeseer, 2007.

[26] C. Edussooriya, L. Bruton, and P. Agathoklis, “Under-decimated 3d fir space-time cone filters using dft polyphase filter banks for attenuation of radio frequency interference,” in *Circuits and Systems (MWSCAS), 2011 IEEE 54th International Midwest Symposium on*, pp. 1–4, IEEE, 2011.

[27] T. K. Gunaratne, L. Bruton, and P. Agathoklis, “Broadband beamforming of focal plane array (fpa) signals using real-time spatio-temporal 3d fir frustum digital filters,” *Antennas and Propagation, IEEE Transactions on*, vol. 59, no. 6, pp. 2029–2040, 2011.

[28] T. K. Gunaratne, *Beamforming of broadband bandpass signals using multidimensional FIR filters.* PhD thesis, University of Calgary, 2011.

[29] A. Leshem, A.-J. van der Veen, and A.-J. Boonstra, “Multichannel interference mitigation techniques in radio astronomy,” *The Astrophysical Journal Supplement Series*, vol. 131, no. 1, p. 355, 2000.

[30] F. Briggs, J. Bell, and M. Kesteven, “Removing radio interference from contaminated astronomical spectra using an independent reference signal and closure relations,” *The Astronomical Journal*, vol. 120, no. 6, p. 3351, 2000.

[31] S. W. Ellingson, J. D. Bunton, and J. F. Bell, “Removal of the glonass c/a signal from oh spectral line observations using a parametric modeling technique,” *The Astrophysical Journal Supplement Series*, vol. 135, no. 1, p. 87, 2001.

[32] C. U. S. Edussooriya, *Multidimensional signal processing techniques for disturbance mitigation in synthetic aperture systems.* PhD thesis, University of Victoria, 2012.

[33] C. U. Edussooriya, L. T. Bruton, P. Agathoklis, and T. K. Gunaratne, “Low-complexity maximally-decimated multirate 3-d spatio-temporal fir cone and frustum filters,” *Circuits and Systems I: Regular Papers, IEEE Transactions on*, vol. 60, no. 7, pp. 1845–1856, 2013.

[34] T. Q. Nguyen, “Near-perfect-reconstruction pseudo-qmf banks,” *Signal Processing, IEEE Transactions on*, vol. 42, no. 1, pp. 65–76, 1994.

[35] I. Moazzen, *Array Signal Processing for Beamforming and Blind Source Separation.* PhD thesis, 2013.

[36] J. Li, T. Q. Nguyen, and S. Tantaratana, “A simple design method for near-perfect-reconstruction nonuniform filter banks,” *IEEE Transactions on Signal Processing*, vol. 45, no. 8, pp. 2105–2109, 1997.

[37] T. Karp and N. J. Fliege, “Modified dft filter banks with perfect reconstruction,” *Circuits and Systems II: Analog and Digital Signal Processing, IEEE Transactions on*, vol. 46, no. 11, pp. 1404–1414, 1999.

[38] P. P. Vaidyanathan, *Multirate systems and filter banks.* Pearson Education India, 1993.

[39] P. P. Vaidyanathan, “Multirate digital filters, filter banks, polyphase networks, and applications: A tutorial,” *Proceedings of the IEEE*, vol. 78, no. 1, pp. 56–93, 1990.

[40] T. D. Tran, R. L. De Queiroz, and T. Q. Nguyen, “Linear-phase perfect reconstruction filter bank: Lattice structure, design, and application in image coding,” *Signal Processing, IEEE Transactions on*, vol. 48, no. 1, pp. 133–147, 2000.

[41] A. Biem, S. Katagiri, E. McDermott, and B.-H. Juang, “An application of discriminative feature extraction to filter-bank-based speech recognition,” *Speech and Audio Processing, IEEE Transactions on*, vol. 9, no. 2, pp. 96–110, 2001.

[42] S. K. Mitra and Y. Kuo, *Digital signal processing: a computer-based approach*, vol. 2. McGraw-Hill New York, 2006.

[43] M. I. Skolnik, “Introduction to radar,” *Radar Handbook*, vol. 2, 1962.

[44] P. Vaidyanathan, Y.-P. Lin, S. Akkarakaran, and S.-M. Phoong, “Discrete multitone modulation with principal component filter banks,” *Circuits and Systems I: Fundamental Theory and Applications, IEEE Transactions on*, vol. 49, no. 10, pp. 1397–1412, 2002.

[45] B. E. Usevitch and M. T. Orchard, “Adaptive filtering using filter banks,” *Circuits and Systems II: Analog and Digital Signal Processing, IEEE Transactions on*, vol. 43, no. 3, pp. 255–265, 1996.

[46] M. G. Bellanger and J. Daguet, “Tdm-fdm transmultiplexer: Digital polyphase and fft,” *Communications, IEEE Transactions on*, vol. 22, no. 9, pp. 1199–1205, 1974.

[47] T. D. Tran and T. Q. Nguyen, “On m-channel linear phase fir filter banks and application in image compression,” *Signal Processing, IEEE Transactions on*, vol. 45, no. 9, pp. 2175–2187, 1997.

[48] N. Fliege, “Computational efficiency of modified dft polyphase filter banks,” in *Signals, Systems and Computers, 1993. 1993 Conference Record of The Twenty-Seventh Asilomar Conference on*, pp. 1296–1300, IEEE, 1993.

[49] N. J. Fliege, "Modified dft polyphase sbc filter banks with almost perfect reconstruction," in *Acoustics, Speech, and Signal Processing, 1994. ICASSP-94., 1994 IEEE International Conference on*, vol. 3, pp. III–149, IEEE, 1994.

[50] T. Karp and N. J. Fliege, "Mdft filter banks with perfect reconstruction," in *Circuits and Systems, 1995. ISCAS'95., 1995 IEEE International Symposium on*, vol. 1, pp. 744–747, IEEE, 1995.

[51] K. Nayebi, T. P. Barnwell, and M. J. Smith, "Time-domain filter bank analysis: A new design theory," *Signal Processing, IEEE Transactions on*, vol. 40, no. 6, pp. 1412–1429, 1992.

[52] T. Nguyen, "A quadratic-constrained least-squares approach to the design of digital filter banks," in *Circuits and Systems, 1992. ISCAS'92. Proceedings., 1992 IEEE International Symposium on*, vol. 3, pp. 1344–1347, IEEE, 1992.

[53] T. Q. Nguyen, "Digital filter bank design quadratic-constrained formulation," *Signal Processing, IEEE Transactions on*, vol. 43, no. 9, pp. 2103–2108, 1995.

[54] H. S. Malvar, *Signal processing with lapped transforms.* Artech House, 1992.

[55] K. Schittkowski, "On the convergence of a sequential quadratic programming method with an augmented lagrangian line search function 2," *Optimization*, vol. 14, no. 2, pp. 197–216, 1983.

[56] K. Schittkowski, "Nlpql: A fortran subroutine solving constrained nonlinear programming problems," *Annals of operations research*, vol. 5, no. 2, pp. 485–500, 1986.

[57] I. Moazzen, "Matlab function to design uniform filter bank," 2011.

[58] I. Moazzen and P. Agathoklis, "Fast filter bank design (ffbd)," 2013.

[59] Y.-P. Lin and P. Vaidyanathan, "Application of dft filter banks and cosine modulated filter banks in filtering," in *Circuits and Systems, 1994. APCCAS'94., 1994 IEEE Asia-Pacific Conference on*, pp. 254–259, IEEE, 1994.

[60] C. U. Edussooriya, L. T. Bruton, M. A. Naeini, and P. Agathoklis, "Using 1-d variable fractional-delay filters to reduce the computational complexity of 3-d broadband multibeam beamformers," 2014.

[61] H. Fastl and E. Zwicker, *Psychoacoustics: Facts and models*, vol. 22. Springer Science & Business Media, 2007.

[62] Y. Lian and Y. Wei, "A computationally efficient nonuniform fir digital filter bank for hearing aids," *Circuits and Systems I: Regular Papers, IEEE Transactions on*, vol. 52, no. 12, pp. 2754–2762, 2005.

[63] J. M. de Haan, I. Claesson, and H. Gustafsson, "Least squares design of nonuniform filter banks with evaluation in speech enhancement," in *Acoustics, Speech, and Signal Processing, 2003. Proceedings.(ICASSP'03). 2003 IEEE International Conference on*, vol. 6, pp. VI–109, IEEE, 2003.

[64] T. Gülzow, A. Engelsberg, and U. Heute, "Comparison of a discrete wavelet transformation and a nonuniform polyphase filterbank applied to spectral-subtraction speech enhancement," *Signal processing*, vol. 64, no. 1, pp. 5–19, 1998.

[65] I. Balasingham and T. A. Ramstad, "Optimized perfect reconstruction tree-structured filter banks for image coding," in *Image Processing, 1996. Proceedings., International Conference on*, vol. 1, pp. 585–588, IEEE, 1996.

[66] R. K. Soni, A. Jain, and R. Saxena, "An optimized design of non-uniform filter-bank using blackman window family.," *International Journal of Signal & Image Processing*, vol. 1, no. 1, 2010.

[67] S. Anurag and A. Kumar, "Non-uniform filter bank design using modified window functions," in *Computational Intelligence and Signal Processing (CISP), 2012 2nd National Conference on*, pp. 165–170, IEEE, 2012.

[68] P.-Q. Hoang and P. Vaidyanathan, "Non-uniform multirate filter banks: Theory and design," in *Circuits and Systems, 1989., IEEE International Symposium on*, pp. 371–374, IEEE, 1989.

[69] S. Akkarakaran and P. Vaidyanathan, "New results and open problems on nonuniform filter-banks," in *Acoustics, Speech, and Signal Processing, 1999. Proceedings., 1999 IEEE International Conference on*, vol. 3, pp. 1501–1504, IEEE, 1999.

[70] M. J. Absar and S. George, "On the search for compatible numbers in the design of maximally decimated perfect reconstruction non-uniform filter bank," in *Signal Processing Systems, 2001 IEEE Workshop on*, pp. 141–148, IEEE, 2001.

[71] K. Nayebi, T. P. Barnwell III, and M. J. Smith, "Nonuniform filter banks: A reconstruction and design theory," *Signal Processing, IEEE Transactions on*, vol. 41, no. 3, pp. 1114–1127, 1993.

[72] K. Nayebi, T. P. Barnwell III, and M. J. Smith, "Block decimated analysis-synthesis filter banks," in *Circuits and Systems, 1992. ISCAS'92. Proceedings., 1992 IEEE International Symposium on*, vol. 2, pp. 947–950, IEEE, 1992.

[73] K. Nayebi, T. P. Barnwell III, and M. Smith, "The design of perfect reconstruction nonuniform band filter banks," in *Acoustics, Speech, and Signal Processing, 1991. ICASSP-91., 1991 International Conference on*, pp. 1781–1784, IEEE, 1991.

[74] T. Chen, L. Qiu, and E.-W. Bai, "General multirate building structures with application to nonuniform filter banks," *Circuits and Systems II: Analog and Digital Signal Processing, IEEE Transactions on*, vol. 45, no. 8, pp. 948–958, 1998.

[75] B. Liu and L. T. Bruton, "The design of nonuniform-band maximally decimated filter banks," in *Circuits and Systems, 1993., ISCAS'93, 1993 IEEE International Symposium on*, pp. 375–378, IEEE, 1993.

[76] B. Liu and L. Bruton, "The design of n-band nonuniform-band maximally decimated filter banks," in *Signals, Systems and Computers, 1993. 1993 Conference Record of The Twenty-Seventh Asilomar Conference on*, pp. 1281–1285, IEEE, 1993.

[77] T. Nagai, T. Futie, and M. Ikehara, "Direct design of nonuniform filter banks," in *Acoustics, Speech, and Signal Processing, 1997. ICASSP-97., 1997 IEEE International Conference on*, vol. 3, pp. 2429–2432, IEEE, 1997.

[78] J.-J. Lee and B. G. Lee, "A design of nonuniform cosine modulated filter banks," *Circuits and Systems II: Analog and Digital Signal Processing, IEEE Transactions on*, vol. 42, no. 11, pp. 732–737, 1995.

[79] A. Kumar, G. Singh, and S. Anurag, "An optimized cosine-modulated nonuniform filter bank design for subband coding of ecg signal," *Journal of King Saud University-Engineering Sciences*, 2013.

[80] G. Shi, X. Xie, X. Chen, and W. Zhong, "Recent advances and new design method in nonuniform filter banks," in *Communications, Circuits and Systems Proceedings, 2006 International Conference on*, vol. 1, pp. 211–215, IEEE, 2006.

[81] W. Zhong, G. Shi, X. Xie, and X. Chen, "Design of linear-phase nonuniform filter banks with partial cosine modulation," *Signal Processing, IEEE Transactions on*, vol. 58, no. 6, pp. 3390–3395, 2010.

[82] B. Vo and S. Nordholm, "Non-uniform dft filter banks design with semi-definite programming," in *Signal Processing and Information Technology, 2003. ISSPIT 2003. Proceedings of the 3rd IEEE International Symposium on*, pp. 42–45, IEEE, 2003.

[83] J. M. de Haan, N. Grbic, I. Claesson, and S. Nordholm, "Design and evaluation of nonuniform dft filter banks in subband microphone arrays," in *Acoustics, Speech, and Signal Processing (ICASSP), 2002 IEEE International Conference on*, vol. 2, pp. II–1173, IEEE, 2002.

[84] J. M. de Haan, N. Grbic, I. Claesson, and S. Nordholm, "Design of oversampled uniform dft filter banks with delay specification using quadratic optimization," in *Acoustics, Speech, and Signal Processing, 2001. Proceedings.(ICASSP'01). 2001 IEEE International Conference on*, vol. 6, pp. 3633–3636, IEEE, 2001.

[85] X. Xie, X. Chen, and G. Shi, "A simple design method of linear-phase nonuniform filter banks with integer decimation factors," in *Circuits and Systems, 2005. 48th Midwest Symposium on*, pp. 724–727, IEEE, 2005.

[86] X. Chen, X. Xie, and G. Shi, "Direct design of near perfect reconstruction linear phase nonuniform filter banks with rational sampling factors," in *Acoustics, Speech and Signal Processing, 2006. ICASSP 2006 Proceedings. 2006 IEEE International Conference on*, vol. 3, pp. III–III, IEEE, 2006.

[87] X. Xie, L. Liang, G. Shi, and A. Fernandez, "Direct design of linear-phase nonuniform filter banks with arbitrary integer decimation factors,"

[88] L. T. Bruton and N. Bartley, “The design of highly selective adaptive three-dimensional recursive cone filters,” *Circuits and Systems, IEEE Transactions on*, vol. 34, no. 7, pp. 775–781, 1987.

[89] A. Tan and H. Sun, “Structural passive synthesis of three-dimensional recursive cone filters,” in *Circuits and Systems, 1989., Proceedings of the 32nd Midwest Symposium on*, pp. 1119–1122, IEEE, 1989.

[90] J. Pitas and A. N. Venetsanopoulos, “The use of symmetrics in the design of multidimensional digital filters,” *Circuits and Systems, IEEE Transactions on*, vol. 33, no. 9, pp. 863–873, 1986.

[91] V. Rajaravivarma, P. Rajan, and H. Reddy, “Application of symmetry results in 3-d digital filter design,” in *System Theory, 1989. Proceedings., Twenty-First Southeastern Symposium on*, pp. 277–281, IEEE, 1989.

[92] G. Runze and P. Steffen, “A contribution to the design of digital three-dimensional fir and iir cone filters,” in *Proceedings of 3D Image Analysis und-synthesis’ 96*, Citeseer, 1996.

[93] B. Kuenzle and L. T. Bruton, “3-d iir filtering using decimated dft-polyphase filter bank structures,” *Circuits and Systems I: Regular Papers, IEEE Transactions on*, vol. 53, no. 2, pp. 394–408, 2006.

[94] S. Singh and D. Piriyakumar, “Non-uniform bandwidth 3d cone filter bank,” in *Circuits and Systems, 2007. MWSCAS 2007. 50th Midwest Symposium on*, pp. 586–589, IEEE, 2007.

[95] H. Reddy, I.-H. Khoo, and P. Rajan, “2-d symmetry: theory and filter design applications,” *Circuits and Systems Magazine, IEEE*, vol. 3, no. 3, pp. 4–33, 2003.

[96] J. W. Baars, *The paraboloidal reflector antenna in radio astronomy and communication.* Springer, 2007.

Appendix A

Review and ST Modeling of Dense Aperture Arrays Signals and Focal Plane Arrays Signals

A.1 Introduction

In this section, a brief overview of broadband (BB) signals that are received by dense aperture arrays (DAAs) and focal plane arrays (FPAs) is presented. In this presentation, the spatio-temporal (ST) modeling of signals of interest (SOI) that are emanating from a far-field source, and radio-frequency interference (RFI) signals, are addressed. In the case of radio astronomy signals, a natural process like the synchrotron mechanism [32][33] generates SOI. Additionally, the RFI signals can involve natural or artificial electromagnetic radiations from surrounding electronic and broadcasting stations.

A.2 DAAs BB Signals: Introduction and Modeling

Figure A.1 shows a wavefront of electromagnetic waves coming from a far-field as planes. Note that the direction of arrival of the plane wave is specified with the unit vector $\widehat{d}(d_x, d_y, d_z)$ in the 3D space. These electromagnetic waves can be approximated over a small area as four-dimensional (4D) continuous-domain (CD) spatial-temporal (ST) plane waves. Both SOI and RFI signals received by DAAs can be modeled as

4D CD ST plane waves, as in Eq. (A.1). The plane wave in Eq. (A.1) is considered to be uni-polarized; therefore, Eq. (A.1) is treated as a scalar quantity.

$$pw(x, y, z, ct) = w(d_x x, d_y y, d_z z, ct) \tag{A.1}$$

c= speed of light

t=time

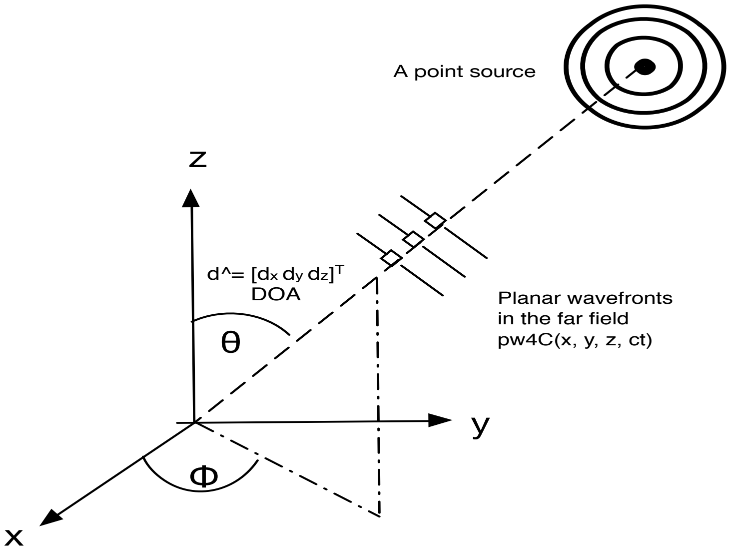

Figure A.1: Electromagnetic waves coming from a far point source as planes, with direction of arrival given by $\widehat{d}(d_x, d_y, d_z)$

In the polar coordination, the direction of arrival can be expressed, as in Eq. (A.2), where θ is the inclination angle, and ϕ is the azimuth angle. These two angles are also illustrated in Figure A.1.

$$\widehat{d}(d_x, d_y, d_z) = [\sin(\theta)\cos(\phi)\sin(\theta)\sin(\phi)\cos(\theta)]^T \tag{A.2}$$

$$where\,\phi \in [0°, 360°]\,and\,\theta \in [0°, 180°]$$

At the ground level, where $z = 0$, the 4D plane wave signal in Figure A.1 can be expressed as a 3D equation, as in Eq. (A.3):

$$pw(x, y, 0, ct) = w(d_x x, d_y y, 0, ct)$$

$$pw(x, y, ct) = w(d_x x, d_y y, ct) \tag{A.3}$$

Further, the 3D plane wave in Eq. (A.3) can be expressed as a 3D CD Fourier Transform (CDFT), as in Eq. (A.4) [16], to expose its spectrum and region of support.

$$PW(\Omega_x, \Omega_y, \Omega_{ct}) = W(\Omega_{ct})\delta(\Omega_x - \sin(\theta)\cos(\phi)\Omega_{ct})\delta(\Omega_y - \sin(\theta)\sin(\phi)\Omega_{ct}) \quad \text{(A.4)}$$

$$where \quad \delta(.)\, is\, 1D\, DC\, impulse\, response$$

Note that the terms $(\Omega_x - \sin(\theta)\cos(\phi)\Omega_{ct}) = 0$ and $(\Omega_y - \sin(\theta)\sin(\phi)\Omega_{ct}) = 0$ are two planes, and their line of intersection represents the region of support of $PW(\Omega_x, \Omega_y, \Omega_{ct})$. See Figure A.2 for a pictorial representation. Note that ϕ is the angle between the Ω_{ct} axis and the region of support, and is expressed in Eq. (A.5); and β is the angle of the project of region of support on $\Omega_{ct} = 0$ and Ω_x, and is expressed in Eq. (A.6).

$$\alpha = \tan^{-1}\sin(\theta) \quad \text{(A.5)}$$

$$\beta = \phi \quad \text{(A.6)}$$

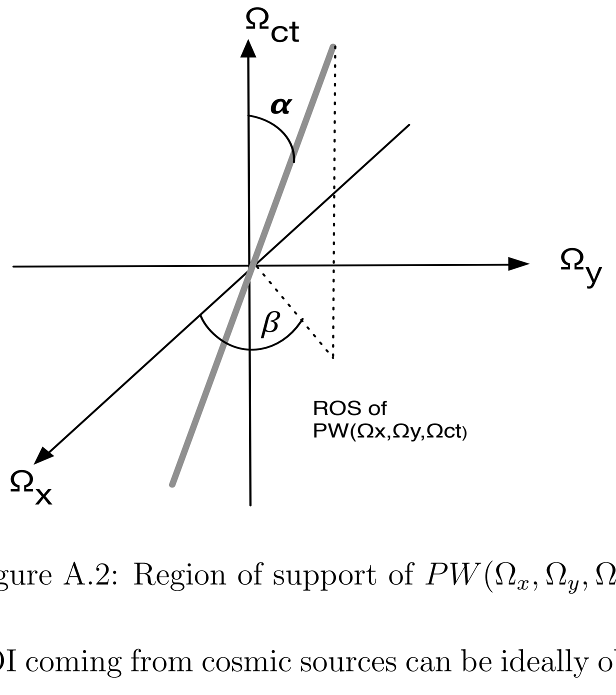

Figure A.2: Region of support of $PW(\Omega_x, \Omega_y, \Omega_{ct})$

Although the SOI coming from cosmic sources can be ideally observed with a large field of view (FoV), such as $\theta \in [0°, 90°]$ and $\phi \in [0°, 360°]$; the FoV is practically limited to $\theta \in [0, D^{\circ}_{max}]$, where D°_{max} is equal to the maximum inclination scan angle of a DAAs sky beam [32][33][40]. The practical limitations on the FoV is because of ground noise and RFI signals that arrive with high angles, such as $\theta > 80°$ [16][32][33]. The DAAs as in the Square Kilometre Array (SKA), for instance, has D°_{max} of 45° and 60° for its phase 1 and phase 2, respectively [25]. In this example, the spectrum of the SOI does not overlap with the spectra of RFI signals because they have different directions of arrival, as shown in Figure A.3. Three-dimensional ST cone filters can be utilized to enhance the SOI and attenuate the RFI signals, based on the direction of arrival properties illustrated in Figure A.3.

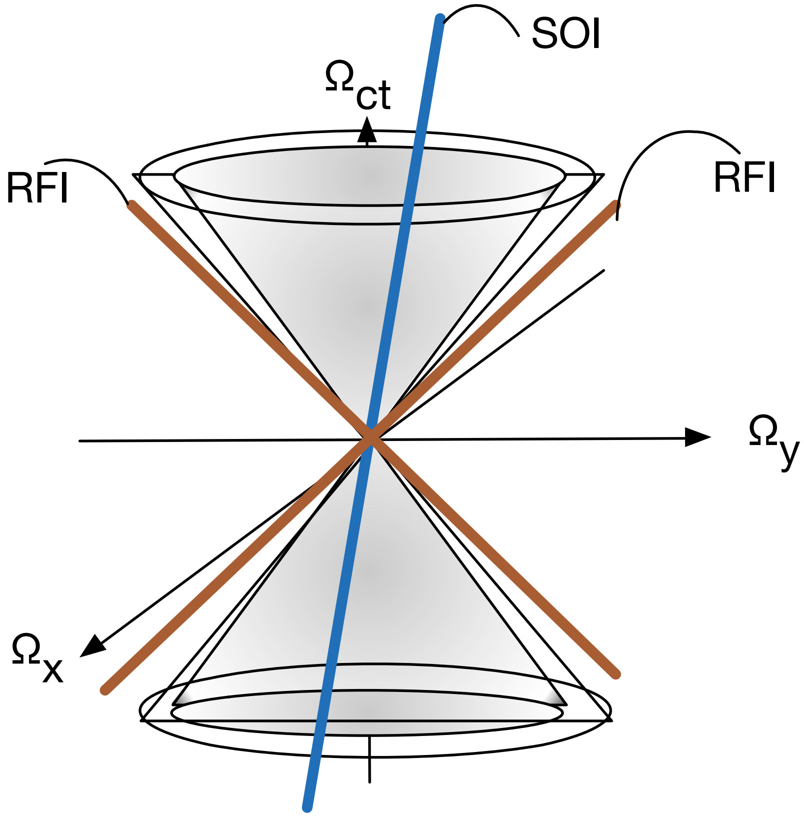

Figure A.3: The region of support of the SOI and RFI signals of DAAs from Eq. (A.4)

A.3 FPAs BB Signals: Introduction and Modeling

In the case of FPAs, the BB ST PW SOI coming from a cosmic source are received with FPAs that are mounted on a paraboloidal reflector, as illustrated in Figure A.4. The SOI hit the paraboloidal reflector, inducing a surface current, which then becomes a point source. According to ”Hugyens Principle” [96], this point source emanates a spherical wavefront to the focal region; moreover, these waves can be approximated as infinitesimal 3D waveforms. The electromagnetic field, $fp(x, y, ct)$, is created, with superposition from the infinitesimal 3D ST PWs that are emanating from the new point source on the paraboloidal reflector; the equation representing the electromagnetic field is presented in Eq. (A.7) [28][32][33]:

$$fp(x, y, ct) = \sum_{\theta} \sum_{\phi} pw^{\theta\phi}(x, y, ct) \tag{A.7}$$

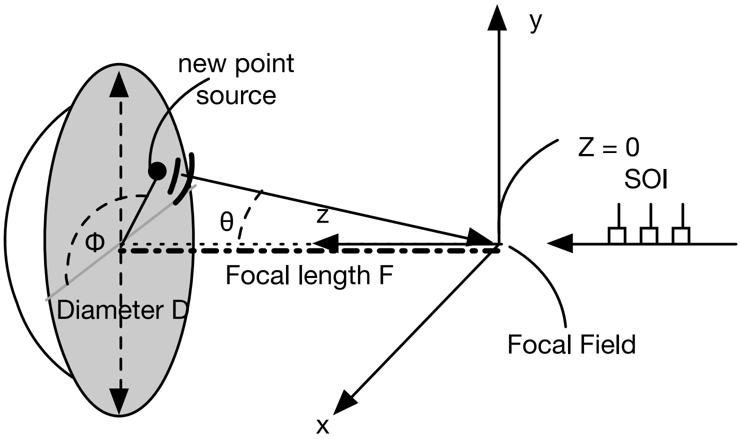

Figure A.4: The SOI received with paraboloidal reflector. Note that a new point source on the paraboloidal reflector reflects SOI from surface current to the focal field

Note that $PW(x, y, ct)$ is given by Eq. (A.3). The point source on the paraboloidal reflector surface has an inclination angle, θ, that varies as $\theta \in [0, \theta_{f_{max}}]$, where $\theta_{f_{max}}$ is the subtended angle, and is given by Eq. (A.8) [32][33]:

$$\theta_{f_{max}} = \tan^{-1}\left(\frac{\frac{F}{2D}}{(\frac{F}{D})^2 - \frac{1}{16}}\right) \tag{A.8}$$

F = focal length, and D = diameter

The emanated signal is concentrated on the focal region, and the region of the spectrum can be determined as a CDFT equation, as in Eq. (A.9) [28][32]:

$$FP(\Omega_x, \Omega_y, \Omega_{ct}) = \sum_{\theta} \sum_{\phi} PW^{\theta\phi}(\Omega_x, \Omega_y, \Omega_{ct}) \tag{A.9}$$

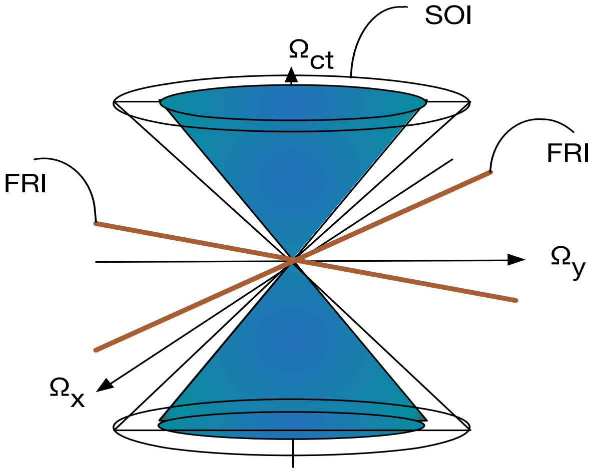

Figure A.5: The region of support of the SOI and RFI signals of FPA from Eq. (A.9)

The region of support of $FP(\Omega_x, \Omega_y, \Omega_{ct})$ is given by superposition of $PW(\Omega_x, \Omega_y, \Omega_{ct})$, and it has a solid double-cone shape with a half-angle equal to $\alpha_{f_{max}} = \tan^{-1}\sin(\theta_{f_{max}})$. The conic region of support of the SOI does not overlap with the RFI signals, just as in the case for DAAs (see Figure A.3). A 3D cone filter can be used to pass the SOI and reject the RFI signal based on the region of support, as illustrated in Figure A.5.

Appendix B

Poly-phase Implementation of Filter Banks

B.1 Efficient Implementation Using Poly-phase Representation of any Maximally-Decimated Filter Bank

Poly-phase representations of filter banks (FBs) have been used to represent various classes of FBs [38]. In these representations, the analysis filters and synthesis filters can be represented as M poly-phase components, in Eq. (B.1) to Eq. (B.4). Therefore, any maximally-decimated FB can be presented with two poly-phase matrices: $\mathbf{E}(\mathbf{z}^{\mathbf{M}})$ and $\mathbf{R}(\mathbf{z}^{\mathbf{M}})$ [38]. Figure B.1 illustrates the poly-phase representation of a maximally-decimated FB using these matrices, where $E(z)$ is the type-1 poly-phase for the analysis filters, and $R(z)$ is the type-3 poly-phase for synthesis filters; they are written in Eq. (B.5) and Eq. (B.6) respectively [38].

$$H_k(z) = \sum_{l=0}^{n_k-1} z^{-l} H_{kl}(z^M) (\text{type 1 poly-phase}) \tag{B.1}$$

$$F_k(z) = \sum_{l=0}^{n_k-1} z^{M-1-l} F_{kl}(z^M) (\text{type 3 poly-phase}) \tag{B.2}$$

$$\begin{bmatrix} H_0(z) \\ H_1(z) \\ \vdots \\ H_{M-1}(z) \end{bmatrix} = \begin{bmatrix} E_{0,0}(z^M) & E_{0,1}(z^M) & \cdots & E_{0,M-1}(z^M) \\ E_{1,0}(z^M) & E_{1,1}(z^M) & \cdots & E_{0,M-1}(z^M) \\ \vdots & \vdots & \ddots & \vdots \\ E_{M-1,0}(z^M) & E_{M-1,1}(z^M) & \cdots & E_{M-1,M-1}(z^M) \end{bmatrix} \times \begin{bmatrix} 1 \\ z^{-1} \\ \vdots \\ z^{M-1} \end{bmatrix} \tag{B.3}$$

$$\begin{bmatrix} F_0(z) \\ F_1(z) \\ \vdots \\ F_{M-1}(z) \end{bmatrix} = \begin{bmatrix} z^{M-1} \\ \vdots \\ z^{-1} \\ 1 \end{bmatrix}^{\mathsf{T}} \times \begin{bmatrix} R_{0,0}(z^M) & R_{0,1}(z^M) & \cdots & R_{0,M-1}(z^M) \\ R_{1,0}(z^M) & R_{1,1}(z^M) & \cdots & R_{0,M-1}(z^M) \\ \vdots & \vdots & \ddots & \vdots \\ R_{M-1,0}(z^M) & R_{M-1,1}(z^M) & \cdots & R_{M-1,M-1}(z^M) \end{bmatrix} \tag{B.4}$$

$$\mathbf{E}(z) = \begin{bmatrix} E_{0,0}(z^M) & E_{0,1}(z^M) & \cdots & E_{0,M-1}(z^M) \\ E_{1,0}(z^M) & E_{1,1}(z^M) & \cdots & E_{0,M-1}(z^M) \\ \vdots & \vdots & \ddots & \vdots \\ E_{M-1,0}(z^M) & E_{M-1,1}(z^M) & \cdots & E_{M-1,M-1}(z^M) \end{bmatrix} \tag{B.5}$$

$$\mathbf{R}(z) = \begin{bmatrix} R_{0,0}(z^M) & R_{0,1}(z^M) & \cdots & R_{0,M-1}(z^M) \\ R_{1,0}(z^M) & R_{1,1}(z^M) & \cdots & R_{0,M-1}(z^M) \\ \vdots & \vdots & \ddots & \vdots \\ R_{M-1,0}(z^M) & R_{M-1,1}(z^M) & \cdots & R_{M-1,M-1}(z^M) \end{bmatrix} \tag{B.6}$$

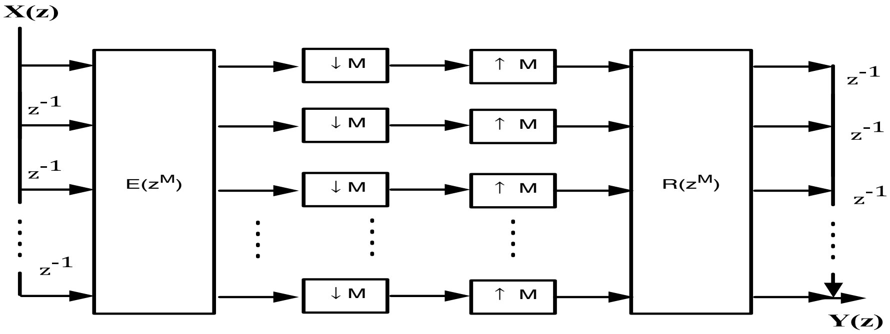

Figure B.1: The representation of a maximally-decimated FB using two poly-phase matrices $\mathbf{E}(\mathbf{z^M})$ and $\mathbf{R}(\mathbf{z^M})$ [38]

Any FB can be implemented with low computational complexity if the filtering is performed at lower rates. Therefore, using noble identities, the down-sampling can be performed prior to the $\mathbf{E}(\mathbf{z}^{\mathbf{M}})$ matrix of the analysis filters, and the up-sampling can be performed after the $\mathbf{R}(\mathbf{z}^{\mathbf{M}})$ matrix of the synthesis filters, as depicted in Figure B.2. This poly-phase representation, diagrammed in Figure B.2, can be used to implement any maximally-decimated FB including DDFBs and QM-CM filter banks. Furthermore, the matrices $\mathbf{E}(\mathbf{z})$ and $\mathbf{R}(\mathbf{z})$ can be simplified into one matrix, $\mathbf{S}(\mathbf{z})$, to achieve the schematic in Figure B.3,[38]. Note that poly-phase representation can be used to represent any filter or signal with any poly-phase components [38].

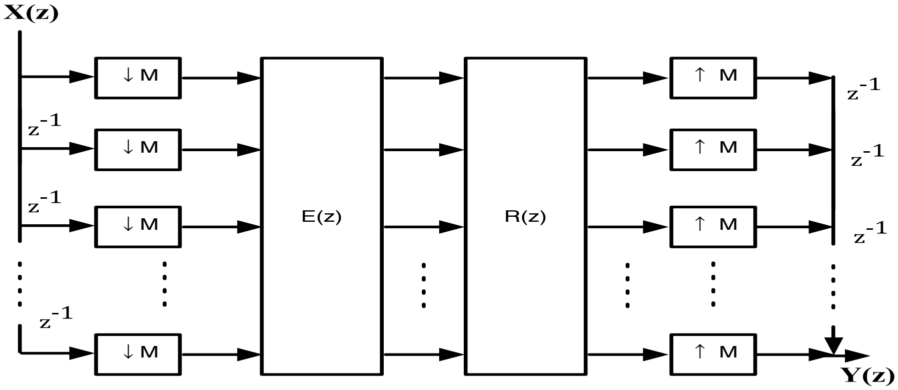

Figure B.2: Efficient implementation of a maximally-decimated FB with poly-phase matrices [38]

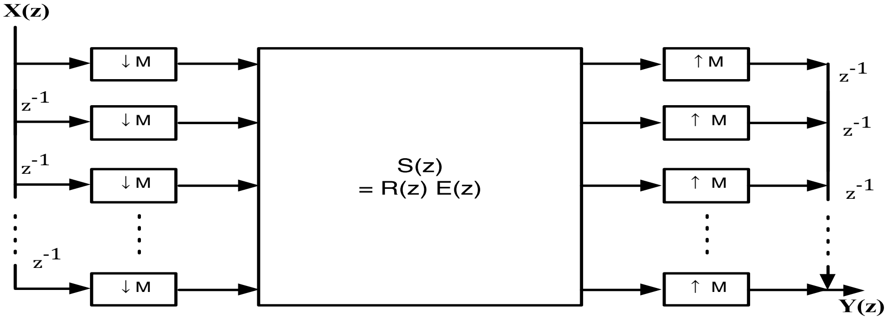

Figure B.3: Further simplifying efficient implementation of a maximally-decimated FB [38]

B.2 Efficient Implementation of QM-CM Filter Banks Using 2M Poly-phase Representation and a T matrix

The modulated analysis filters, h(z), and synthesis filters, f(z), of QM-CM FBs can be presented using $2M$ poly-phase components $G_k(z^{2M})$, where $k = 0, 1, \cdots, 2M-1$, of the prototype filter; and a real $(M \times 2M)$ T matrix that consists of the real cosine-modulation coefficients. Figures (B.4) and (B.5) illustrate the analysis filters and synthesis filters, respectively, that are represented by $G_k(z^{2M})$ and T matrix. The poly-phase component $G_k(z^{2M})$ is formulated in Eq. (B.7), and the T matrix expressed as t_{kn} is written in Eq. (B.8). The analysis filters, $h(z)$, can be expressed as in Eq. (B.9); and the synthesis filters, $f(z)$ (which are the image copies of the analysis filters), can be expressed as in Eq. (B.10).

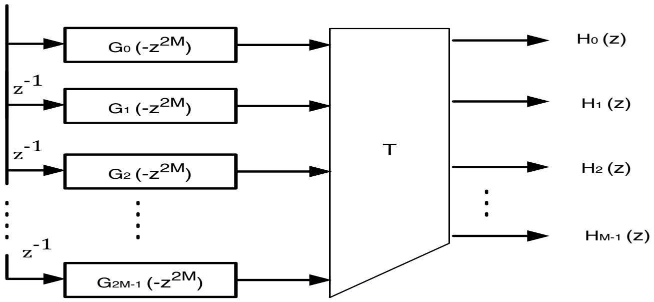

Figure B.4: Representation of analysis filters using $2M$ poly-phase and a T matrix [38]

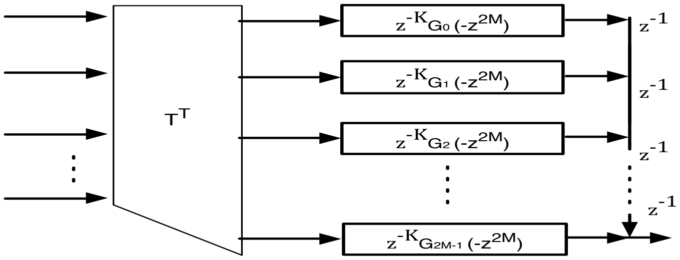

Figure B.5: Representation of synthesis filters using $2M$ poly-phase and a T matrix [38]

$$G_k(z) = \sum_{l=0}^{2M_k-1} z^{-l} P(z^{2M}) (\text{type 1 poly-phase}) \tag{B.7}$$

$$t_{kn} = 2\cos\left((2K+1)\frac{\pi}{2M}(n - (\frac{N-1}{2} + (-1)^k\frac{\pi}{4}))\right) \tag{B.8}$$

$$H_k(z) = Tg_k(z) \tag{B.9}$$

$$g(z) = \begin{bmatrix} G_0(-z^{2M}) \\ z^{-1}G_1(-z^{2M}) \vdots \\ z^{-(2M-1)}G_{2M-1}(-z^{2M}) \end{bmatrix} \tag{B.10}$$

$$f_k^T = z^{-N}H_k(z^{-1})^T = z^{-N}g^T(z^{-1})T^T \tag{B.11}$$

Figure B.6, diagrams how a computationally efficient implementation can be achieved for a QM-CM FB. Note that the down-sampling is performed before the analysis filters, and the up-sampling is performed after the synthesis filters. Computation complexity is reduced, by performing the filtering of analysis and synthesis filters efficiently at lower rates.

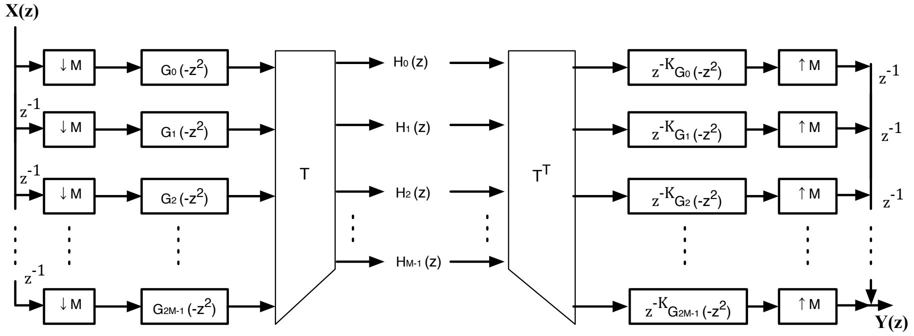

Figure B.6: Efficient implementation of QM-CM FB using $2M$ poly-phase and a T matrix [38]

Appendix C

Analysis of 3D Cone and Frustum Filters Distortions Effect

C.1 Amplitude and Aliasing Distortions for proposed QM-CM and DDFBs Cone Filters

In this section, the aliasing and amplitude distortions of the proposed 3D ST QM-CM and DDFBs cone and frustum filters in Chapters (4) and (5) is analysed to illustrate their effects during filtering. In this analysis, a 3D test signal with size (41,41,1024) is constructed from a 1D signal with size (1,1024). The frequency response of 1D is depicted in Figure C.1. The 3D test signal is processed with a 16-band 3D ST QM-CM cone filter. The output samples (21,21,1:1024) are analysed to investigate the distortions effects. Figures C.2 to C.7 illustrate the output for the discs of the cone filter: the first disc, the first two discs, the first four discs, and so on; until the output of the entire 16 discs of the cone filter is represented. Notice that the total output in Figure C.8, which shows a magnified version of the 16 discs illustrated in Figure C.7, is almost identical to the input signal, with errors between -0.01 to 0.008 ($= -40\ dB$) . The error is insignificant, and it includes the aliasing distortion and amplitude distortion as well. Also note that the aliasing effect for the discs can be seen in the figures; it has negligible effects, at the high frequency edges only.

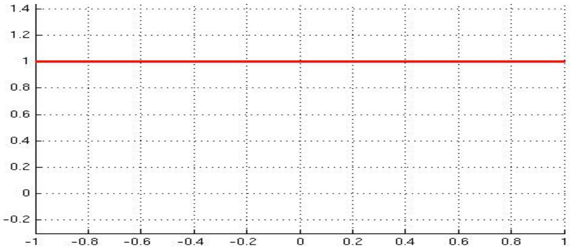

Figure C.1: The input 1D signal, with unity frequency response from -1 to 1

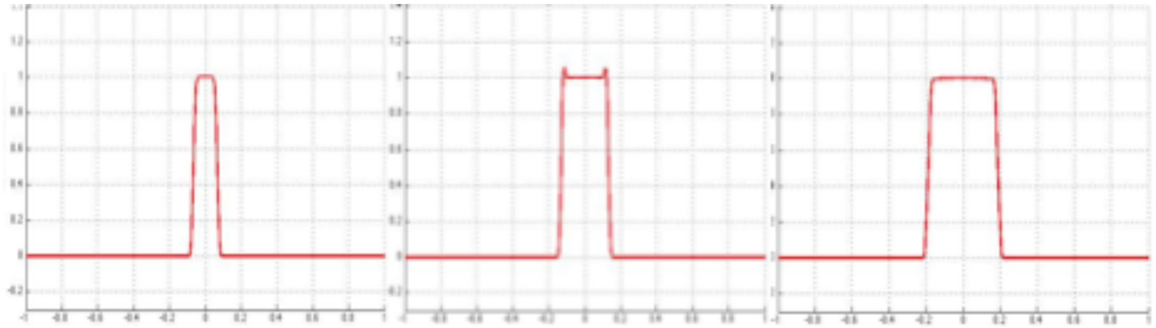

Figure C.2: The output of a 16-band 3D QM-CM cone filter for the first disc, the first two discs, and the first three discs

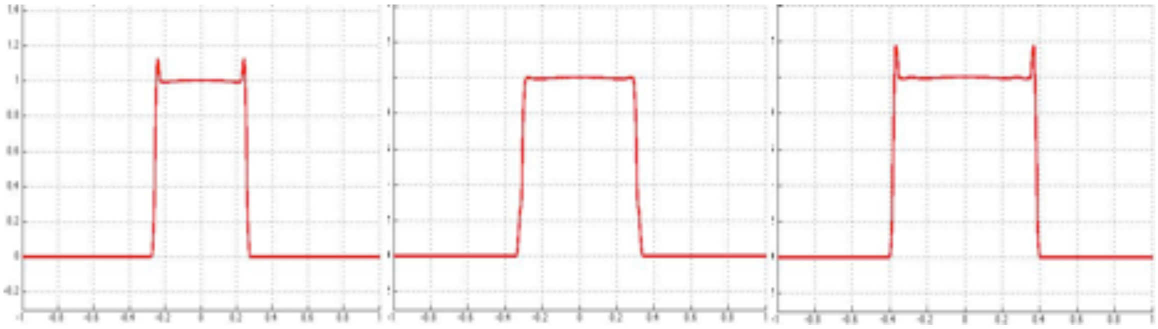

Figure C.3: The output of a 16-band 3D QM-CM cone filter for the first four discs, the first five discs, and the first six discs

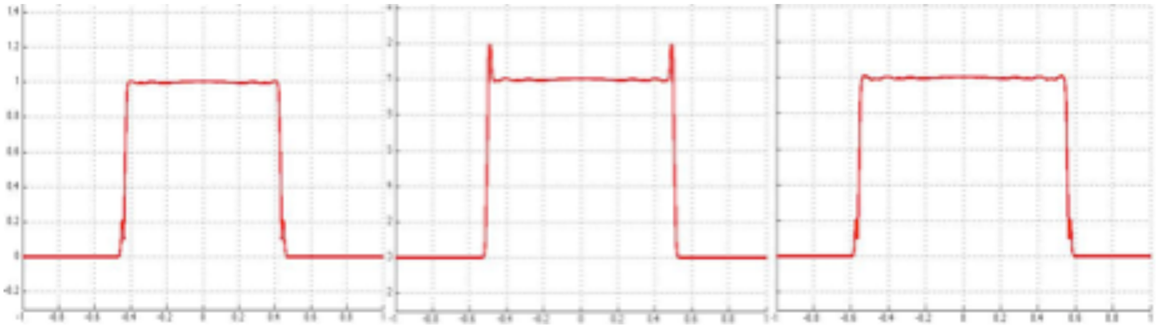

Figure C.4: The output of a 16-band 3D QM-CM cone filter for the first seven discs, the first eight discs, and the nine six discs

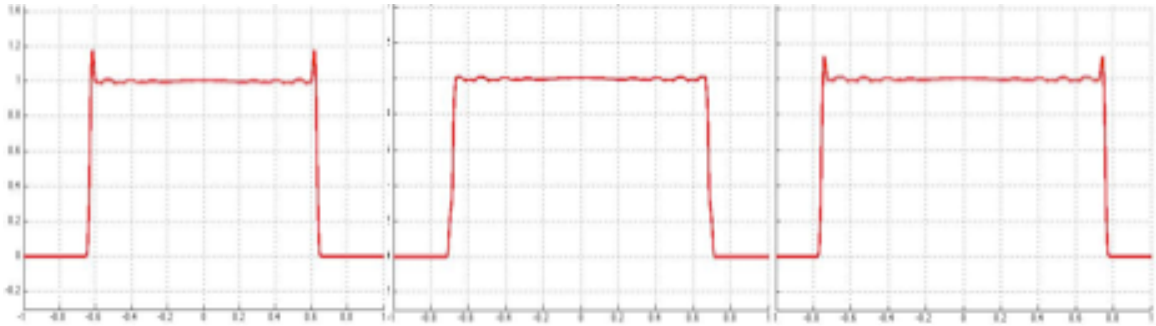

Figure C.5: The output of a 16-band 3D QM-CM cone filter for the first ten discs, the first eleven discs, and the first twelve discs

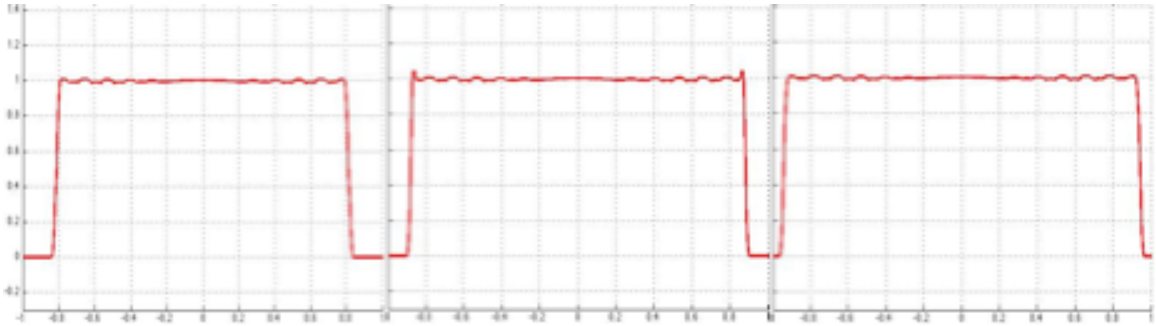

Figure C.6: The output of a 16-band 3D QM-CM cone filter for the first thirteen discs, the first fourteen discs, and the first fifteen discs

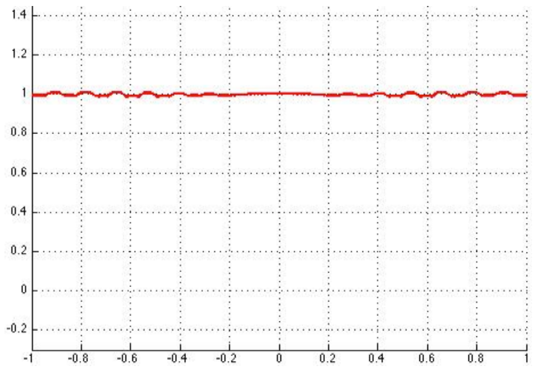

Figure C.7: The output of a 16-band 3D QM-CM cone filter for the entire sixteen discs

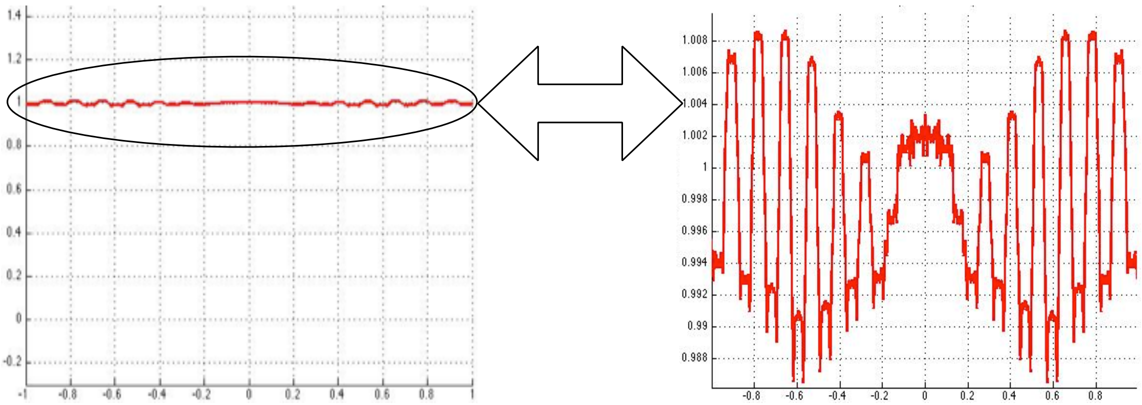

Figure C.8: The output of a 16-band 3D QM-CM cone filter for the entire sixteen discs, with a magnified version